Freie Universität Berlin

Fachbereich Physik

Im Fachbereich Physik der Freien Universität Berlin eingereichte Dissertation zur Erlangung des Doktorgrades der Naturwissenschaften (doctor rerum naturalium) mit dem Titel:

Time-Resolved Analysis of Protonation Dynamics in ChannelRhodopsin-2

Tom Resler

2016

Die Disputation erfolgte am 20.04.2017.

1. Gutachter Prof. Dr. Joachim Heberle
Fachbereich Physik
Freie Universität Berlin

2. Gutachterin Prof. Dr. Ulrike Alexiev
Fachbereich Physik
Freie Universität Berlin

Parts of this thesis have been already published:

V. A. Lórenz-Fonfría, C. Bamann, **T. Resler**, R. Schlesinger, E. Bamberg, and J. Heberle; Temporal evolution of helix hydration in a light-gated ion channel correlates with ion conductance; PNAS, 112:E5796-5804, (2015).

T. Resler, B.-J. Schultz, V. A. Lórenz-Fonfría, R. Schlesinger and J. Heberle; Kinetic and Vibrational Isotope Effects of Proton Transfer Reactions in Channelrhodopsin-2; Biophys Journal, 109:287-297, (2015).

V. A. Lórenz-Fonfría, B.-J. Schultz, **T. Resler**, R. Schlesinger, C. Bamann, E. Bamberg and J. Heberle; Pre-gating conformational changes in the ChETA variant of channelrhodopsin-2 monitored by nanosecond IR spectroscopy; JACS, 137:1850-1861, (2015).

V. A. Lórenz-Fonfría, **T. Resler**, N. Krause, M. Nack, M. Gossing, G. Fischer von Mollard, C. Bamann, E. Bamberg, R. Schlesinger, J. Heberle; Transient protonation changes in channelrhodopsin-2 and their relevance to channel gating; PNAS, 110:E1273–E1281, (2013).

M. Nack, I. Radu, B.-J. Schultz, **T. Resler**, R. Schlesinger, A.-N. Bondar, C. Del Val, S. Abbruzzetti, C. Viappiani, C. Bamann, E. Bamberg, J. Heberle; Kinetics of proton release and uptake by channelrhodopsin-2; FEBS Lett, 586:1344-1348, (2012).

Manuscripts in preparation:

T. Resler, N. Krause, V. Muders, M. Saita, V. A. Lórenz-Fonfría, C. Rosin, R. Schlesinger, R. Winter and J. Heberle; Pressure dependence of the photocycle kinetics of channelrhodopsins.

T. Resler, E. Bühl, C. Bamann, B.-J. Schultz, R. Lam, R. Schlesinger, E. Bamberg, J. Wachtveitl and J. Heberle; Assigning the role of R120 in the gating of ChR2 by time-resolved IR spectroscopy from femto- to milliseconds.

Abstract

As presented in my thesis, we made enormous progress in resolving the molecular details of the photoreaction of the light-gated ion channel channelrhodopsin-2 (ChR2), by applying time-resolved molecular spectroscopy. I have shown that D253 is the primary proton acceptor and D156 the internal proton donor of the retinal Schiff base of ChR2. The reprotonation of the latter residue constitutes the molecular determinant for channel closure. Upon H/D exchange of the solvent, the kinetic and vibrational isotope effects of these reactions and that of E90, a key residue in ion selectivity, were determined. My experiments with a pH indicating dye show that the de- and reprotonation of E90 takes place during the life time of the desensitized P_4^{480} state. Thus, other conclusions that E90 plays a key role in channel opening are clearly ruled out.
Light-adapted ChR2 contains a mixture of all-*trans* and 13-*cis* retinal. I contributed to time-resolved analysis of the E123T variant and we could show that the 13-*cis* photocycle does not lead to channel opening. Furthermore, the channel opening tallies with transient changes in the amide I vibration, identified as water influx to hydrate the peptide backbone. These findings from ChR2 were confirmed by experiments on variants of ChR2 that exhibit accelerated (E123T) or delayed (D156E) channel opening. The associated activation volumes are monitored and quantified by flash photolysis under hydrostatic pressures. Finally, the loss-of-function variant R120H was investigated, which exhibits wild-type photocycle kinetics but channel activity is blocked. Time-resolved IR spectroscopy covering almost 13 decades in time are presented (from 500 fs to s). An assignment of the arginine band was not feasible, but the possible role of His-Arg interactions were discussed and I demonstrated that R120 is not part of the proton release complex.

Although the mechanistic link between proton transfer reactions and channel function remain elusive, I could show that protonation dynamics are crucial in the ChR2 photocylce and are related to ion conductance. ChR2 is the mayor tool in optogenetics and a detailed understanding of this ion channel is supportive for medical application. Furthermore, it is a good model system for other ion channels, because in ChR2 ion permeation is triggered repeatable, non-invasive and reproducible by light, which allows the observation of channel on- and off-gating with high temporal and spacial resolution.

Zusammenfassung

In meiner Dissertation präsentiere ich unsere Fortschritte bei der molekularen Erforschung des lichtgesteuerten Ionenkanals Kanalrhodopsin-2 (ChR2) mittels zeitaufgelöster Spektroskopie. Ich konnte zeigen, dass D253 der primäre Protonenakzeptor und D156 der primäre Protonendonor der Schiffschen Base in ChR2 ist. Die Reprotonierung von D156 geht einher mit der Kanalschließung. Durch Messungen in H_2O und D_2O konnten der kinetische und spektrale Isotopeneffekt dieser Reaktionen und von E90 bestimmt werden. E90 is wichtig für die Ionenselektivität, aber eine De- und Resprotonierungsdynamik wurde nur im späten P_4^{480} Intermediat beobachtet. Damit konnten andere Schlussfolgerungen, dass E90 eine wichtige Rolle bei der Kanalöffnung hat, widerlegt werden.
Im lichtadaptierten Zustand von ChR2 liegt das Retinal in der all-*trans* und 13-*cis* Konfiguration vor. Wir konnten anhand der E123T Variante zeigen, dass der 13-*cis* Photozyklus nicht zu einer Kanalöffnung führen kann. Die Öffnung des Ionenkanals folgt Schwingungsänderungen in der Amid I region, welche als Einströmen von Wassermolekülen identifiziert wurde, welche die Helices hydratisieren. Diese Korrelation wurde mit Hilfe von Varianten bestätigt, welche eine beschleunigte (E123T) bzw. langsamere (D156E) Kanalaktivität zeigen. Die erwarteten Aktivierungsvolumen wurden durch Blitzlichtspektroskopie bei verschiedenen Drücken ermittelt. Die Variante R120H hat keine Kanalaktivität mehr, jedoch einen unveränderten Photozyklus. Zeitaufgelöste Absorptionsänderungen über fast 13 Dekaden (von 500 fs bis s) wurden dargestellt. Die Zuordnung der Argininbande war nicht eindeutig, jedoch wurden His-Arg Interaktionen im Detail erörtert und ich konnte zeigen, dass R120H nicht Teil der Protonenabgabegruppe ist.

Obwohl die genaue Verbindung zwischen Protonierungsänderungen und Kanalfunktion nicht vollständig geklärt wird, konnten wir zeigen, dass Protonierungsdynamiken eine entscheidende Rolle in ChR2 haben. Es ist das am häufigsten verwendete optogenetische Werkzeug und detaillierte Erkenntnisse über dieses Protein werden die medizinische Anwendungsmöglichkeiten verbessern. Außerdem ist ChR2 ein gutes Modellsystem für andere Ionenkanäle, da die Kanalöffnung nicht invasiv und reproduzierbar durch Licht aktiviert werden kann. Dies ermöglicht die Untersuchung der Kanalaktivität mit hoher zeitlicher und spektraler Auflösung.

Contents

Abbrevations

ATR attenuated total reflection

bR bacteriorhodopsin

BXB bromoxylenol blue

ChR channelrhodopsin

FTIR Fourier-transform infrared

HEK human embryonic kidney

IR infrared

KIE kinetic isotope effect

MD molecular dynamics

Nd:YAG neodymium-doped yttrium aluminium garnet

OPO optical parametric oscillator

PM purple membrane

PMT photomultiplier

QCL quantum cascade laser

SB Schiff base

SVD single value decomposition

TM transmembrane

UV/Vis ultraviolet-visible

VIE vibrational isotope effect

WT ChR2-wt

1 Introduction

> *A physicist is just an atom's way of looking at itself.*
>
> **— Niels Bohr**

Physics is a scientific field where scientists try to understand time and space, structures and materials, the interdependency of radiation, fundamental processes and general rules, as well as different other things. In experimental science, these concepts often lead to a strong focus on method development to overcome the borders and to proof theoretical models. In molecular biophysics the same fundamental question are addressed, although an interplay between biology, chemistry and physics is necessary [1].

In this interdisciplinary work, I will present my results about the membrane protein channelrhodopsin-2 (ChR2) obtained by time-resolved absorption difference spectroscopy. A macromolecule like ChR2 absorbs electromagnetic radiation in the visible (Vis) range by its bound retinal cofactor and in the infrared (IR) range by molecular vibrations. Time-resolved difference spectroscopy is used to track only those absorption changes that are relevant for the function of the protein. ChR2 is a light-gated ion channel and founded the new research field of optogenetics, where it is used to trigger neuronal cells by light. At the beginning of my research the underlying molecular mechanism was unknown, but I observed key proton transfer events and structural changes associated with ion gating. The focus on protonation dynamics and its coupling to the protein function leads to an improvement of the fundamental understanding of the membrane protein ChR2. These results also address the general role of protonation dynamics in proteins and help to understand other ion channels as well.

1.1 Channelrhodopsin

1.1.1 Ion transport across a biological membrane

Cell membranes are hydrophobic and largely impermeable for water and ions. Still, controlled ion transport across a biological membrane plays a key role in all biological systems, a task conducted by specialized membrane proteins. One differentiate these transmembrane proteins between active and passive ion transporters, i.e. pumps and channels. Ion pumps work against an ion gradient and transfer ions across the membrane, which often increase the membrane potential. In contrast, ion channels often depolarize the membrane potential by passive flow of ions across the membrane. Membrane proteins have specific architectures and some hydrophilic residues that form water-filled cavities or water wires. Such water networks play a key role for ion transport. Often, only specific ions are transported in either cases, selected by specific binding sites in ion pumps or by a selectivity filter in ion channels. The ion selectivity is given by a specific geometry and charge distribution of polar amino acids within the protein, as discussed in detail by Gouaux and MacKinnon [2] and Corry and Chung [3]. Ion channels can be classified into different categories depending on their gating mechanism. For instance, mechano-sensitive channels are activated by pressure on the membrane, voltage-gated channel respond to the membrane voltage, ligand-gated channels opens a pore after ligand binding [3].

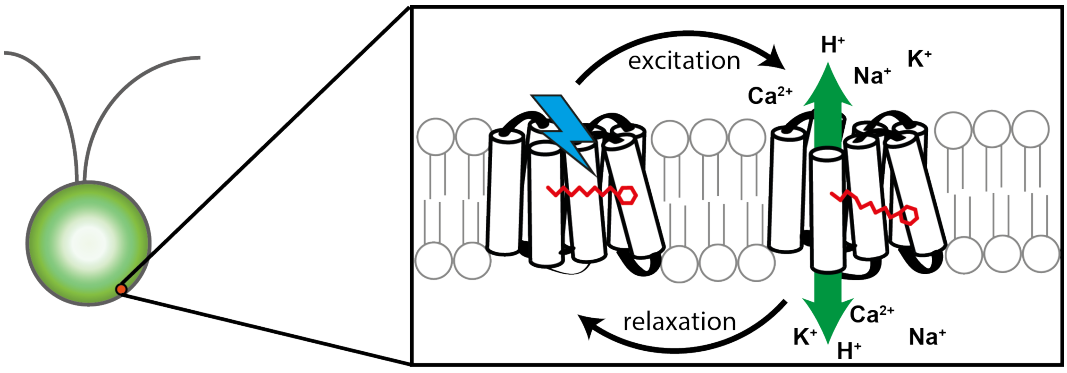

Fig. 1.1: Schematic representation of the light-gated cation-selective ion channel channelrhodopsin (right). It is naturally found in the eye-spot (red dot) of the green alga *Chlamydomonas reinhartii* (left). Light excitation leads to pore formation and relaxation drives the ground state recovery. The retinal chromophore is highlighted in magenta and the lipid membrane is shown in grey.

Here, the light-gated ion channel, named channelrhodopsin (ChR), is investigated (Fig. 1.1). Up to now, these light-gated ion channels are only found in the family of microbial rhodopsins (also known as type I rhodopsins) and lacking sequence

homology to other ion channels [4]. In microbial rhodopsins other ion transporters are observed and well characterized like bacteriorhodopsin (a light-gated proton pump) and halorhodopsin (a light-gated chloride pump).

Like other microbial rhodopsins, ChR2 consists of seven transmembrane helices and a retinal as chromophore. The light-absorbing co-factor (the retinal) is bound via a protonated lysine Schiff base (SB) to the apoprotein (Fig. 1.3). Blue-light excitation of the all-*trans* retinal leads to isomerization around the $C13 = C14$ bond, conformational changes, proton transfer reactions and eventually to cation permeation through the open channel. For that, some amino acids may have a crucial role in the photocycle by direct proton transfer or structural changes that lead to proton transport. This can be linked to the photocycle model, built on the description of transient absorption changes by intermediate states, named P_1^{500}, P_2^{390}, P_3^{520} and P_4^{480} (see Fig. 1.2) [5–7]. The superscript and subscript are representing the maximal absorbing wavelength and the order of the intermediate states in the photocycle, respectively. This plain photocycle model works as a starting point for the later discussion of the time-resolved data and conclusions.

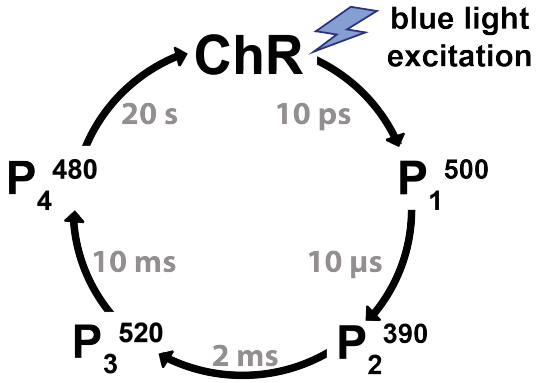

Fig. 1.2: The photocycle of ChR2 with its intermediate states (modified from [5]). The superscript represents the maximal absorbing wavelength and the subscript represents the order of the intermediate states in the photocycle after blue-light excitation. The time constants are colored in grey.

1.1.2 Optogenetics

Channelrhodpsin is a photoreceptor, naturally found in the eyespot of the unicellular green alga *Chlamydomonas reinhardtii* [8]. In its native host, ChR triggers the flagella machinery to swim towards or away from light (phototaxis). This is necessary to optimize photosynthetic growth [9]. Under physiological conditions, the cation current depolarizes the membrane potential, and if expressed heterologous in neuronal host cells, action potentials can be triggered upon illumination.

The ion channeling activity can be triggered fast (by laser excitation), non-invasive, and repeatable by light. In 2002 Nagel et al. [8] was the first who identified and characterized ChR, setting the grounds for the posterior new research field called optogenetics [10]. In principle, optogenetics can be also achieved with ion pumps, but the transport of only one ion per photocycle is less efficient to depolarize the cell membrane. Ion channels are able to transport many ions per photocycle. It was also important that the concentration of the retinal chromophore (vitamin A) in the host cells (including mammalian ones) are often sufficient to express the protein in functional form. Otherwise the co-factor had to be added externally, limiting the applications. The history of optogenetics is explained in detail by Hegemann and Nagel, 2013 [11]. As an important example for the function of optogenetics was the partial recovery of vision in blind mice [12]. The following list of publications provide detailed informations about optogenetics and how it is used in living other organisms: [13–25]. However, for medical application a detailed mechanistic understanding of ChRs supports the safety for the patients and allows the modification of this optogenetic tool. In addition, channelrhodopsin is a model system for other ion channels and the comparison with ion pumps may lead to a better understanding of ion translocations across membranes. Knowledge about the mechanistic details will lead to a variety of optogenetic tools.

1.2 Protonation dynamics of ChR2

The main hypothesis of my research is that protonation dynamics play a key role in coordinating and controlling the function of proteins. The term 'protonation dynamics' includes: short-distance relocation of protons between neighboring amino acids, long-distance proton transfer along water chains and protonatable groups, rearrangement of hydrogen-bonded networks, and remotely induced protonation changes by long-range electrostatic changes.

1.2.1 Proton translocation within the protein

To observe atomic interactions we need a high temporal and spacial resolution. Time-resolved absorption spectroscopy offers the unique opportunity to track protonation dynamics over decades in time and allows the identification of single protonation events. Ion channeling might correlate to or be caused by these dynamics [26]. The functional mechanism can be followed from femtoseconds to seconds, covering the whole photocylce kinetics (see Fig. 1.2). Here, time-resolved infrared (IR) and ultraviolet-visible (UV/Vis) difference absorption spectroscopy

are used. In ChR2 the residue D253 is identified as the primary proton acceptor (D212 in bacteriorhodopsin (bR)) and D156 is the primary proton donor (D115 in bR) of the retinal SB, see Fig. 1.3. Although the well-studied proton pump bR and channelrhodopsin (ChR) show some sequence homologies [27], the results are different. In bR, D85 (E123 in ChR2) is the primary proton acceptor and D96 (H134 in ChR2) is the primary proton donor [28]. Surprisingly, ChR2 also act as a leaky proton pump [29] and show proton uptake and release events, as observed by pH indicator experiments [30].

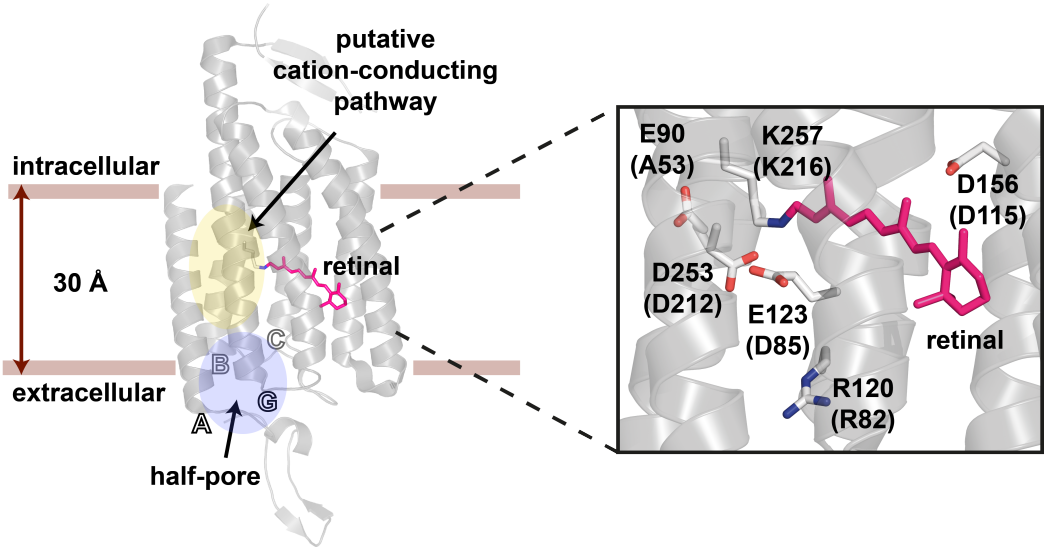

Fig. 1.3: (Left) Crystal structure of the truncated C1C2 chimera of *Cr*ChR1 and *Cr*ChR2 [31]. The water filled half-pore and the putative cation-conducting pathway are highlighted. (Right) Zoom-in of the retinal binding pocket of ChR2. The important amino acids are highlighted: E90, R120, E123, D156, D253 and K257. The letter refers to the amino acid and the numbering are related to the ChR2 sequence. In parenthesis, the structural aligned amino acid in bR are shown.

Although the assignment of the primary proton donor D156 in ChR2 was later challenged by the observations of an unusual spectral shift under hydrogen/deuterium (H/D) exchange measured under steady-state conditions at 80 K [32, 33], time-resolved experiments at room temperature solved the conflict [34], see section 1.2.2. The occurrence and role of other protonation changes are more controversial. Deprotonation of E90 was suggested to occur on an early time scale (sub-nanoseconds), according to molecular dynamics simulations [35]. However, early deprotonation of E90 is inconsistent time-resolved step-scan FTIR data and pH indicator experiments of the E90A variant [5]. Under H/D exchange, the observed kinetic isotope effect rather supports a deprotonation of E90 in the millisecond range [34].

1.2.2 Hydrogen/deuterium exchange

The exchange of H_2O versus D_2O as a solvent leads to delays in reaction steps, partially by solvent effects and primarily by deuteration of exchangeable hydrogens of the reactants. The increased mass of deuterium leads to a lower zero-point energy of the vibrational ground state, thereby increasing the energy barrier to break hydrogen bonds [36], which accounts for the pD value in D_2O being 0.4 higher than the equivalent pH value in H_2O [37]. Two major effects are observed when deuterium substitutes hydrogen in a protein: First, a frequency downshift of a vibrational mode is observed, if this band is originating from a $X-H$ group or coupled to such a group (vibrational isotope effect (VIE)). This case apply to the $C=O$ stretching vibration of carboxylic acids, which are coupled to the $O-H$ bending vibration. Second, reaction steps are slowed in a protein, if breaking and formation of hydrogen bonds are involved. It can be quantified as the ratio of the rate constants that are recorded for the sample immersed in H_2O and in D_2O, known as the kinetic isotope effect (KIE) [38]. This parameter has proven of enormous impact in mechanistic studies of membrane proteins such as bacteriorhodopsin [39, 40], photosystem II [41, 42], cytochrome-c oxidase [43], lactose permease [44], and others.

In this work, the KIEs of the photoreaction of ChR2 is determined by flash photolysis UV/Vis spectroscopy, namely, for the P_1^{500}/P_2^{390}, P_2^{390}/P_3^{520}, and P_3^{520}/P_4^{480} transitions. A novel flash-photolysis setup for nanosecond time-resolved IR spectroscopy is introduced, using tunable quantum cascade lasers (QCLs) as a light source, to determine the KIE for specific deprotonation and reprotonation events. These results shed light on the role of D156 as the internal proton donor to the retinal Schiff base and gauge the possibility that E90 deprotonates before the formation of the P_4^{480} intermediate, as proposed by others [35, 45].

1.3 Photoreactions of ChR2 under conditions with negligible channel activity

1.3.1 13-*cis* photocycle

The retinal of *Ca*ChR1 from *Chlamydomonas augustae* and ChR2 from *Chlamydomonas reinhardtii* in dark state was found to be in a mixture of all-*trans* and 13-*cis* configuration with a ratio of 70:30, respectively [46, 47]. Basically, both conformation could lead to a different photocycle. The all-*trans* state leads to conductive photocylce but functionality of the 13-*cis* photocycle is still inconclusive [4]. Analysis of the stationary photo currents suggests the presence of two conductive photocycles with different ion conductivity and selectivities as well as on- and off-kinetics [48–51].

The fast channeling ChR2 variant E123T (also known as ChETA) was used for time-resolved UV/Vis and IR spectroscopy with a time-resolution of several ns to answer the question: Does the 13-*cis* photocylce leads to a conductive state? It turns out, that this photocycle recovers within 1 ms, which is faster than most proton transfer reactions as well as the channel-off-gating. Thus, implying a minor functional relevance of the 13-*cis* photocycle in ChR2 [52].

1.3.2 Loss-of-function variant ChR2-R120H

The crystal structure of the C1C2 chimera [31] and the projection map obtained by cryo-electron microscopy [53] reveal structural similarity to different microbial rhodopsins, among others the proton pumping bacteriorhodopsin (bR), see Fig. 1.3. In bR, the extracellular proton pathway is characterized by an extended hydrogen-bonding network starting with the charge-stabilizing counter-ion of the protonated SB (D85, D212), several water molecules and an arginine residue (R82) that is highly conserved among the microbial rhodopsins. Close to the extracellular side, two glutamic acid residues (E194 and E204) are found, which are involved in a fast proton release in bR [54]. However, the sequence of events and the participating homologue residues are different compared to bR. As discussed in section 1.2.1, the residue D253 (D212 in bR) was identified as the primary proton acceptor of the Schiff base proton and D156 (D115 in bR) as the primary proton donor [5]. Kuhne et al. assigning the infrared bands in a different manner and they concluded that E123 acts as a proton acceptor similar to D85 in bR [35]. Furthermore, it is not clear how the protonation reactions at the SB and the residues involved in these reactions

are linked to the formation of the channel's open state. While absence of the charge and different side-chains at position 123 seem not to be detrimental to the channel functionality [10], other homologue residues of bR's hydrogen bonding network show a strong phenotype in electrophysiological recordings. Light-induced currents are abolished especially in mutants of residues D253 and R120 (R82 in bR) in ChR2 [5, 31, 55]. In contrast, mutation of residues located in the channel's pore often show only a minor effect in their channel functionality. There is strong evidence that the ion permeation pathway is formed with participation of transmembrane helices (TMHs) A, B, C and G [31, 53, 56]. Hence, the different effects on the functionality can be understood that the former residues are important for relaying the light reaction of the chromophore to the so far unknown channel gates while the later ones influence the ion selectivity. Noteworthy is residue E90 in the middle of the putative pore whose mutation to an arginine allows anion permeation [57]. Time-resolved IR and electrophysiology experiments reveal that helix hydration correlates with ion conductance summarized in a model of the gating steps in ChR2, see section 1.4.1 [58]. However, a clear picture showing the connection between the chromophore and the channel's gates did not emerge so far despite the wealth of data.

Channel deficient mutants of the hydrogen bonding network provide an opportunity to test their importance in the gating reaction and to assign further spectral markers for the channel functionality. In this thesis, a comprehensive comparison between the ChR2 wild-type and the ChR2-R120H variant is provided. The mutant's phenotype of channel deficiency has a molecular origin, and it is not related to different expression levels compared to the wild-type. As mentioned above, time-resolved Vis-pump and IR-probe and QCL spectroscopy was applied. The combination of both techniques offer the unique opportunity to observe and follow processes directly after protein activation with a very high time resolution. Monitoring the protein dynamics puts a technical challenge, as they cover the time range from femtoseconds to several seconds. Time-resolved pump-probe experiments in the visible [59] and IR [32] range observe the early events after photoexcitation up to 1.8 ns, missing the formation of the conducting pore ($\approx$ 200 us). In contrast, time-resolved step-scan FTIR experiments on ChR2 start data recording after 200 ns [35] or 6 μs [5], until the completion of the photocyle. The results of our home-build IR flash photolysis using a quantum cascade laser (QCL) were validated by time-resolved step-scan FTIR spectroscopy [34, 52] and offer a time resolution down to 20 ns. This makes it possible to combine Vis-pump and IR-probe spectroscopy with tunable QCL spectroscopy, covering the time scale from femtoseconds to seconds.

1.4 Structural changes of ChR2

Upon photoexcitation, the retinal chromophore isomerizes, but the protein does not form a conductive state until few hundreds of microseconds [52, 60], raising the questions of how retinal isomerization and the formation of a cation conductive transmembrane pore (gating) are molecularly connected. Protein backbone conformational changes occur from the early picoseconds [32] until the formation and decay of the conductive state [58, 61], as concluded from vibrational changes of the peptidic bond and of carboxylic groups detected by time-resolved infrared spectroscopy. In particular, vibrational changes in the peptidic bond indicate substantial alterations in helical transmembrane segments.

For ChR2 (from *Chlamydomonas reinhardtii*) more structural and mechanistic details are available than for any other ChRs. Distance measurements by EPR pELDOR experiments, freeze-trapping ChR2 wild type [62] and its C128T variant [56] after illumination, the latter with a long living conductive state, detected a movement of the intracellular end of helix B by a few angstroms. Comparable results were obtained by cryo-electron microscopy on 2D crystals of the C128T variant [53], which also detected smaller movements of other helices (B, F and G). In combination with the X-ray structure of a ChR1-ChR2 chimera [31], the above results indicate that the transient formation of a conductive transmembrane pore relays on the outward tilt of helix B to be tilted.

1.4.1 Helix hydration and pore formation

X-ray crystallography and EPR experiments are static methods and it is important to determine the timing of these structural rearrangements. It was concluded from molecular dynamics (MD) simulations that helix B is tilted by 3.9 Å within less than 100 ns after light excitation of the all-*trans* retinal. Leading to an early water filled pore between helix A,C and G [35], which would be three order of magnitudes earlier than the observed ion flow measured by time-resolved electrophysiology experiments (100 ns vs 200 μs). To investigate this conflict time-resolved step-scan Fourier-transform infrared (FTIR) experiments on ChR2-wt were performed to characterize molecular events with high temporal resolution. In collaboration with Christian Bamann, who performed time-resolved whole-cell patch clamp experiments, vibrational modes and ion conductance are correlated. Changes at 1665 cm^{-1} and 1648 cm^{-1} are identified, which originate from changes in the amide I vibration of the protein backbone, tallying with ion conductance. These two bands are presumably connected to the formation of a transmembrane pore caused by the

tilt of helix B, a movement detected by EPR spectroscopy [56, 62]. Measurements of ChR2 dissolved in $H_2^{16}O$ and $H_2^{18}O$ could identify these vibrational changes to be caused by the hydration of the protein backbone. As a control a slow (D156E) and a fast (E123T) channeling variant of ChR2 are measured, showing the same correlation. A model will be presented, how the water influx and efflux correlate with ion permeation.

1.4.2 Pressure dependent measurements

Although time-resolved infrared spectroscopy is very sensitive to both conformational changes in the peptide bond and their corresponding dynamics, the measured vibrational changes cannot be easily localized and are complexly related to the structural changes taking place due to the delocalized nature of the involved vibrations. Local information can be gained by using selectively attached Stark probes [63], and the vibrational interpretation in structural terms is getting less ambiguous thanks to progress in semi-empirical spectral calculations [64]. On the other hand, EPR pELDOR experiments provide precise distance changes between strategically placed cross-linked probes, but these are static and limited in number by the need of selective crosslink of specific protein sites with EPR probes.

Volume changes are a relevant and elegant approach to detect global conformational changes during the functional mechanism of proteins [65, 66]. Optoacoustic spectroscopy is able to monitor such changes from the sub nano- to the short microsecond time range [67, 68]. An extension to the millisecond range can be achieved by applying the photothermal beam deflection method [69, 70]. More conveniently, spectroscopic experiments under variable pressures offer the possibility to track volume changes from nanoseconds to seconds, which includes the pore opening and closure of ChR2 [6, 58]. The application of increasing (decreasing) pressure shifts states in equilibrium towards those states which occupy the smaller (larger) volume (Le Châtelier's principle). It also accelerates (decelerates) reactions that have a transition state with a smaller (larger) volume than the initial state [66, 71], allowing to determine volume changes of reaction intermediates or transition states under nonequilibrium conditions by the kinetic analysis of time-resolved experiments.

Here, I monitored with flash photolysis spectroscopy the pressure dependent kinetic behavior of ChR2 during the photocyclic reaction. This is the first time activation volume changes are resolved in ChR2 during its functional mechanism. The recorded kinetics were subjected to a global fit and lifetime distribution analysis to determine macroscopic rate constants at various pressure values. The dependency of the rate constants on the applied pressure (p) relates to the activation volume ($V^{\neq}$), which

describes the volume differences between the transition state and the initial state A in the conversion between states A to B, and is given by the expression [66, 71]:

$$\Delta V^{\neq} = V^{\neq} - V_A = -RT \cdot (\delta ln(k_{A \mapsto B})/(\delta p)) \tag{1.1}$$

Where k is the rate constant for the conversion of state A to B. We should note, however, that equation 1.1 strictly applies to microscopic rate constants. Several studies about pressure effects on the photocyclic reaction of the light driven proton pump bR, on their native purple membrane have been published [65, 72, 73]. Therefore, to elucidate to which extend the effect of pressure depends on the protein environment, ChR2 is studied in three different artificial biomembrane mimetic systems, namely: dissolved in detergent, embedded into nano discs, and reconstituted in unilamellar lipid vesicles. In contrast to bR, ChR2 shows both accelerated and slowed kinetics under pressure.

2 Materials and Methods

2.1 UV/Vis spectroscopy

2.1.1 Steady-state UV/Vis spectroscopy

As introduced, ChR contains a retinal as chromophore that absorbs visible light and triggers the photocylce. The absorption of the ground state as well as of the intermediate states can be measured by UV/Vis spectroscopy. In such a spectrometer a bright light source is attached to a monochromator, which selects specific wavelengths. The measuring light passes the sample and is detected by a photomultiplier. According to the Lambert-Beer law the measured intensity I is proportional to the initial intensity I_0, the concentration of the sample c, the differential path length dx and the proportionality constant ϵ'.

$$\frac{dI}{dx} = -\epsilon' I c \tag{2.1}$$

Integration leads to the Lambert-Beer law

$$I = I_0 exp(-\epsilon' dc) = I_0 \cdot 10^{-\epsilon_\lambda dc} = I_0 \cdot 10^{-A} \tag{2.2}$$

with the absorption A $(= cd\epsilon_\lambda)$, the molar extinction coefficient $\epsilon_\lambda (= \epsilon'/ln10)$ and the thickness d of the sample.

The absorption of the protein sample with the bound retinal shows two features. First, at around 470 nm (for ChR2-WT) caused the bound retinal (giving the protein its orange color) and at around 280 nm, which results from absorption of aromatic amino acids, i.e. tryptophan, phenylalanine and tyrosine [74]. Fig. 2.1 shows the absolute absorption spectra of ChR2 and its variants, scaled to maximum absorption peak of the retinal. The ratio Abs280nm/Abs470nm reflects the protein purity and quality of the sample. A higher ratio implies the presence of channelopsin (ChR2 without retinal, non-functional) or contaminant proteins. Here, samples with a ratio of around 2 and 4 are used for time-resolved FTIR and UV/Vis spectroscopy. For visible experiments in solution, the concentration of the protein sample (ChR2) was set to 10-20 μM, which results in an absorption of the retinal band at 470 nm (490 nm for E123T) between 0.5 to 1.0.

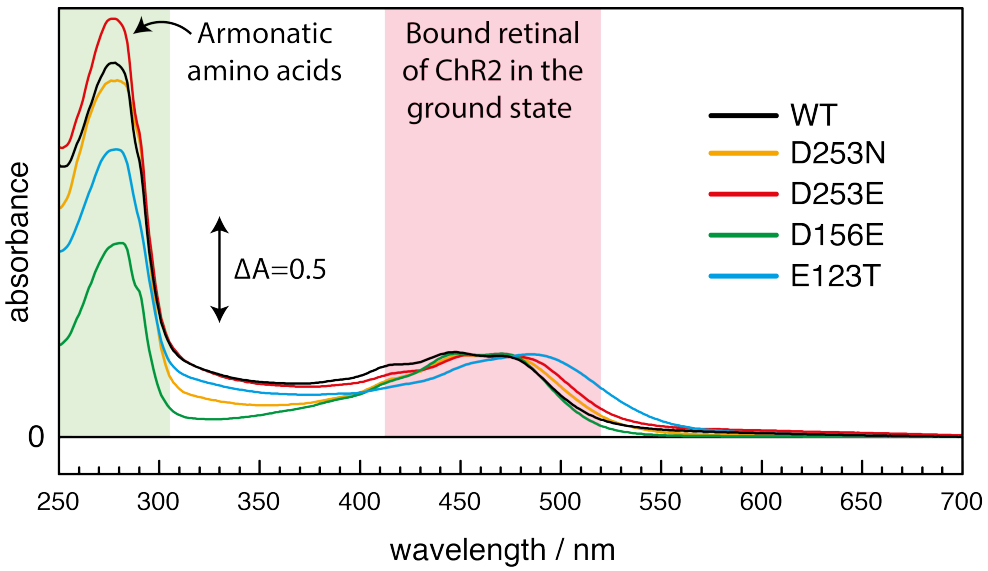

Fig. 2.1: UV/Vis absorption spectra of ChR2 wt (black) and the variants: D253N (yellow), D253E (red), D156E (green), and E123T (blue). The absorption of the bound retinal and the aromatic amino acids are highlighted by a red and green shading, respectively. All spectra are scaled to the retinal absorption peak of the WT.

2.1.2 Time-resolved UV/Vis difference spectroscopy

Absorption changes of the protein sample in the visible range are caused by alternation of the electrostatic properties of the retinal, caused by structural changes of the retinal binding pocket or charge transfer reactions from the Schiff base, resulting in a photocycle. The measured absorption changes are up to 100 times smaller than the ground state due to the partially achievable photoisomerization of the retinal (dependent on the intensity and wavelength of the exciting light) and to the strong spectral overlap between most of the intermediates formed in the photocycle with the initial dark-state. Difference spectroscopy is used to observe the small absorption changes by subtraction of the ground state absorption. Thus, negative absorption changes reflect ground state depletion and positive absorption changes reflect the intermediate states.

Here, a commercial flash photolysis unit was used (LKS80; Applied Photophysics, Leatherhead, Surrey, UK) as schematically shown in Fig. 2.2. The sample was excited with a 10-ns laser pulse at 450 nm and a repetition frequency of 0.1 Hz was used. Precisely, the third harmonic of neodymium-doped yttrium aluminium garnet (Nd:YAG) laser (355 nm) was converted via an optical parametric oscillator (OPO) to 450 nm. This conversion needs high energy light pulses, generated with the Q-switch mode, where an attenuator regulate the quality of the resonator to achieve a high population inversion.

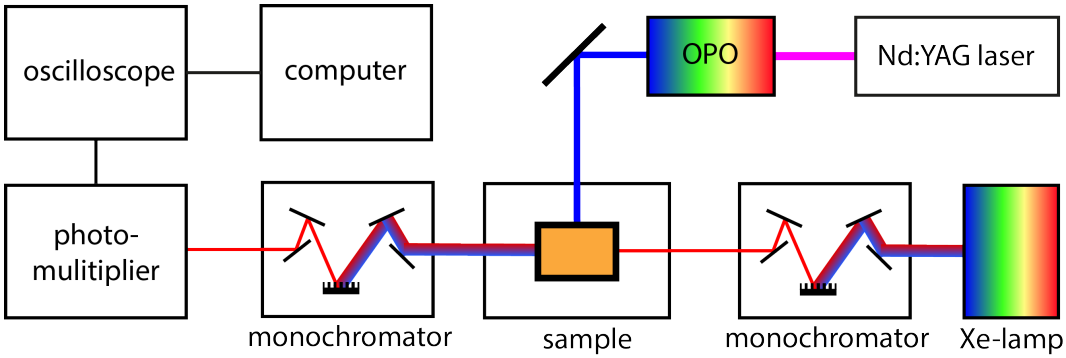

Fig. 2.2: Schematic illustration of a flash photolysis experiment. The probing light is emitted by a xenon arc lamp, attached to the right monochromator, which selects a specific wavelength. The 10-ns laser pulse from a Nd:YAG laser is color-tuned by an OPO to excite the protein sample. The left monochromator prevents the detection of scattering light from the laser pulse. The photomultiplier detects the incoming light and the signal is processed by an oscilloscope.

The energy density of the laser pulses was set to the ideal value of 3 mJ/cm^2, a value considered optimum as determined by a ground state depletion experiment (Fig. 2.3). The probing light was emitted by a xenon arc lamp, which operates in pulsed mode for the early time scale (50 ns to 300 μs) and in continuous mode for the later time scale (300 μs to 50 s). The recorded kinetics were merged together. For each time trace 20,000,000 data points were recorded and logarithmic averaged to compress them into 1,000 data points. Depending on the signal to noise ratio, each time trace is averaged 5 to 20 times. Kinetics are detected at different wavelengths between 300 to 700 nm. The transmitted light is measured by a photomultiplier tube and processed by an oscilloscope (Fig. 2.2).

The resulting absorption changes were analyzed by single value decomposition (SVD) and by global exponential fitting with a home-build *MATLAB* (The MathWorks GmbH, Ismaning, GER) routine. Basically, the SVD method factorize the measured dataset to increase the signal-to-noise ratio. For further information see Hendler et al. [75]. In global exponential fitting the data was fitted using nonlinear weighted least-squares to estimate time constants and amplitude spectra (also known as decay associated spectra). In some cases maximum entropy lifetime distribution analysis was performed. Basically, a distribution of exponential amplitudes vs quasi-continuous values of time constants is obtained by balancing the data description (measured by the least-squares criterion) and the multiplicity of the distribution (measured by an entropy-like expression) [44].

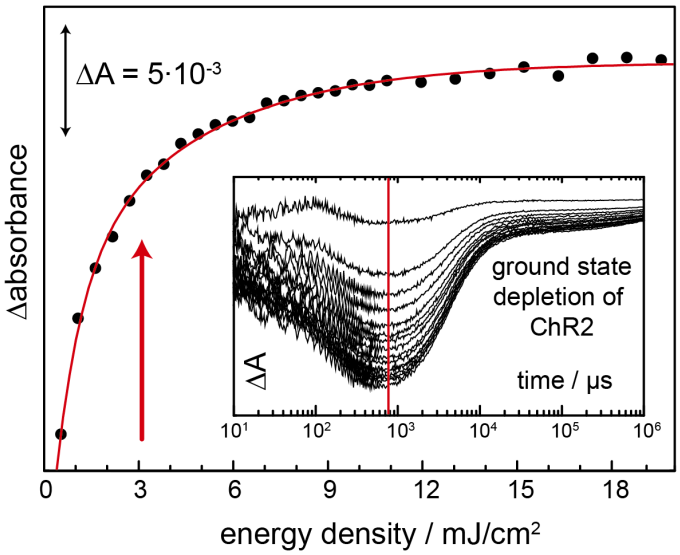

Fig. 2.3: Estimation of the laser energy density by ground state depletion of ChR2 (inset). Optimum between signal intensity and bleaching is found at 3 mJ/cm^2 (red arrow).

2.1.3 pH indicator experiments

Transient pH changes of ChR2 in solution are detected optically with time-resolved UV/Vis spectroscopy as described above. Here, the pH indicator bromoxylenol blue (15 μM BXB) is ideal, because absorption changes at 620 nm are not observed in ChR2 and therefore reflect only the color change of the pH indicator and a high sensitivity at pH 7.4 is observed. Prior to the time-resolved pH indicator experiments, great care was taken to completely remove the imidazole buffer by repetitive washing steps and centrifugation of the solution through polycarbonate filters (Amicon Ultra Centrifugal Filter, cut-off 50 kDa). For time-resolved experiments, 15 μM ChR2 dissolved in 0.2 % decyl maltoside, 100 mM NaCl, pH 7.4 were used, as described by Nack et al. [30].

2.1.4 Pressure dependent measurements

The pressure cell is built on a thermostable jacket that was flooded with water as pressurizing medium (Fig. 2.4). A hand operated hydraulic pump was used to change the pressure, which was measured by manometer from Heise, New England, Newton. To allow for time-resolved UV/Vis spectroscopic studies, three flat sapphire windows are build in the cell for passing probing light and laser excitation pulses. A detailed description can be found elsewhere (Woenckhaus et al. 2000 [76]). The temperature was kept at 25 $°C$. The pressure cell was provided by Roland Winter

(AG Winter, TU Dortmund) and implemented in the flash photolysis setup (section 2.1.2).

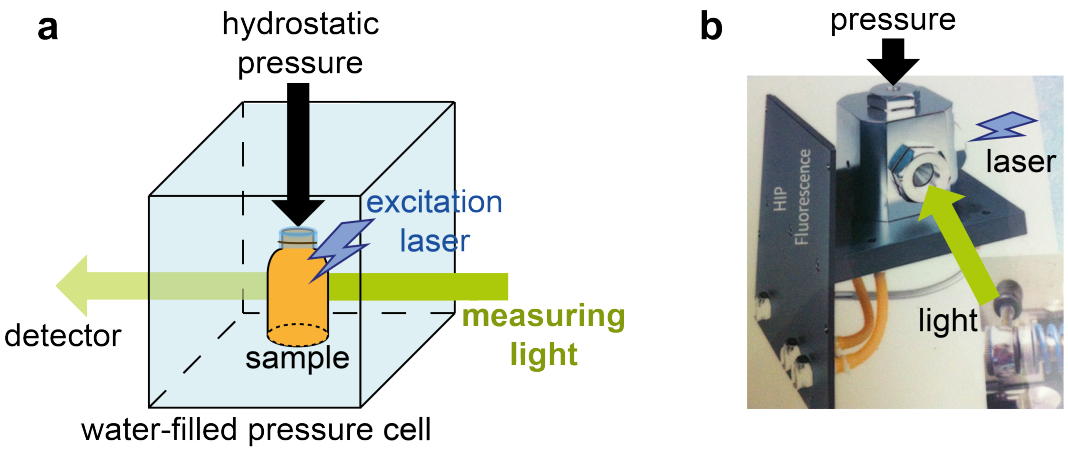

Fig. 2.4: Pressure dependent UV/Vis experiement. (a) Schematic illustration of the water-filled pressure cell. The sample is covered with a membrane, which transfers the pressure to the protein solution. The pressure from 1 bar to 800 bar is produced by water compression. (b) Photographic picture of the pressure cell.

Preparation of ChR2 reconstituted in nanodiscs

The reconstitution process of ChR2 into lipidic nanodiscs was performed by Nils Krause, as adopted from Ritchie et al. 2009 [77]. In brief, 100-200 μM ChR2 in dodecylmaltoside was mixed with the membrane scaffold protein 1D1 (MSP1D1) (typically 100-200 μM) and a DMPC/cholate solution (50 mM/100mM). The molar ratio of ChR2/MSP1D1/DMPC was 0.5/1/55. Incubation for 1 h at 25 $°C$. Subsequently biobeads were added to remove the detergent, inducing the insertion of the protein in the nanodiscs. Incubation for 2 h at 25 $°C$. This mixture was centrifuged at 21.000 g for 20 min to remove larger aggregates. The supernatant was put on a size exclusion column (Superdex 200 10/300, GE Healthcare; buffer: 20mM Hepes, 100 mM NaCl, pH 7.4) at 0.5 mL/min and the peak containing the self-assembled ChR2 nanodiscs was pooled.

Preparation of ChR2 reconstituted in liposomes

The reconstitution process of ChR2 into unilamellar lipid vesicles was performed by Mattia Saita. ChR2, solubilized in dodecyl maltoside, was added to a liposomes suspension consisting of a mixture of Egg PC and PS (Avanti Lipids Polar, Inc.) at

a molar ratio ChR2/PC/PS of 1/40/40. This particular lipid composition showed no aggregation and sedimentation. Therefore, it was preferred to DMPC lipids, which were used for nanodisc reconstitution. The detergent was then removed with Bio-Beads SM-2 (Bio-Rad).

2.2 IR spectroscopy

Molecular vibrations absorb electromagnetic light in the infrared region related to the change in dipole moment. The wavenumber of the absorption bands are characteristic for specific vibrational modes, either from the protein, the solvent or any other molecules present. By doing difference spectroscopy we can observe changes in a single vibrational mode of the entire protein, i.g. changes in hydrogen bonds or protonation events.

2.2.1 FTIR spectroscopy

Over the past 50 year, IR spectroscopy improved drastically and therefore the utility increases. In the beginning, it was only used to elucidate structural feature of new organic compounds and nowadays the scope of application is huge, e.g. kinetic information, proton transfer reactions, and others. In general, IR spectroscopy can be performed by dispersive elements, by IR lasers or by Fourier-Transform (FTIR). The last method allows the detection of the full spectral range at the same time (multiplex or Fellgett advantage) and it has an higher light throughput in comparison to dispersive instruments (Jacquinot advantage) [78]. The main element is a Michelson interferometer that physically Fourier-transforms the IR light intensity. As shown in Fig. 2.5a, the IR beam is divided by a beamsplitter and reflected by a moveable and stationary mirror. Depending on the frequency and the path difference (retardation) the interference pattern changes. FTIR spectrometer usually work in a continuous-scan mode by a permanent movement of the movable mirror. In this mode a whole interferogram is measured. This is ideal for absolute absorption spectra (or very slow reactions), as shown in section 2.2.2. In addition, trapped intermediate states can measured with difference FTIR spectroscopy as described in section 2.2.2.

Time-resolved FTIR measurements need a short reaction trigger, e.g. light pulse. To activate proteins that are not light-triggered, one can use light activatable caged compounds, like calcium chelators, neurotransmitters, phosphates and fluorophores [79]. As shown in Fig. 2.5c, time-resolved IR techniques cover different periods

of time. Pulsed laser based technologies like Vis-pump and IR-probe experiments observe IR absorption changes within femto- to nanoseconds. Our recent home-build QCL spectrometer has a temporal resolution of ≈10-15 ns and prolongs the time range to the hundreds of millisecond time-regime (described in detail in section 2.2.3). FTIR techniques like step-scan, stroboscopic scan, ultrarapid scan, and rapid scan are covering the full spectral range. For a detailed description of FTIR spectroscopy see Herres and Grönholz[80], Baurecht [81], and Griffiths and Haseth [78].

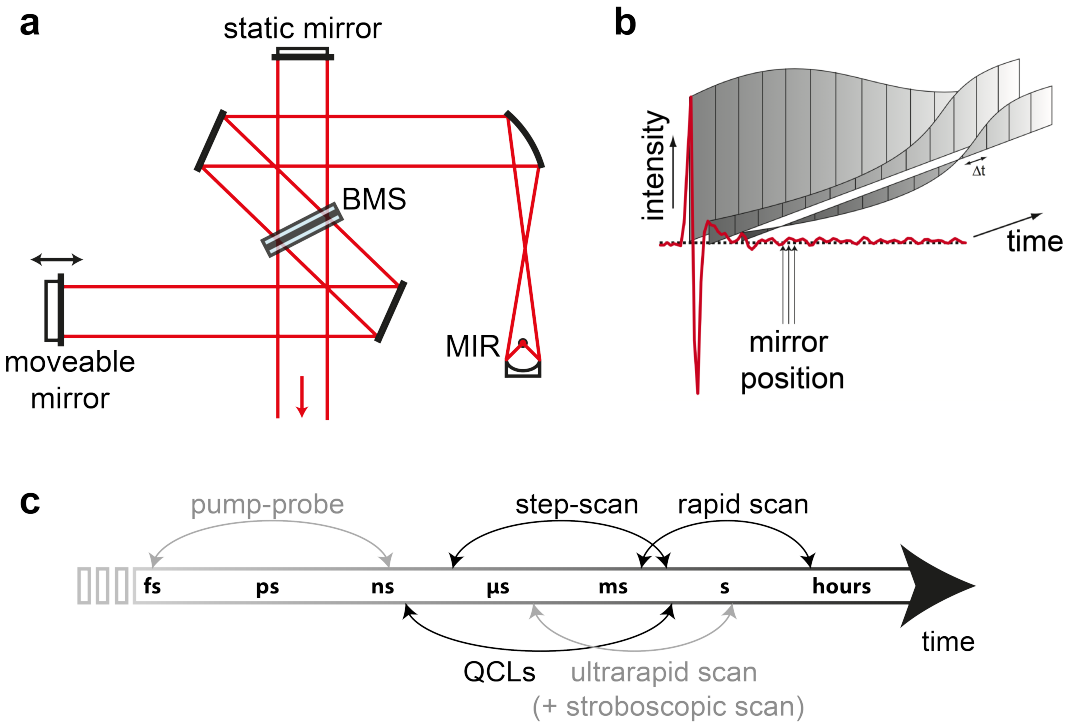

Fig. 2.5: Schematic representation of a FTIR spectrometer. (a) Michelson interferometer containing a mid-infrared source (MIR), a beam splitter (BMS) and a static and a movable mirror. This beam path is used in Vertex 80v spectrometer (Bruker Optics, Ettlingen, Germany), which was used for all FTIR measurements. (b) In the step-scan FTIR method the intensities of the interferogram at specific mirror positions are detected over time. Therefore, to obtain a whole interferogram all mirror positions must be sampled to perform a Fourier transformation to obtain a spectrum. Figure b) is taken from Pfeifer et al.[82]. (c) Time-resolved IR techniques cover different time periods. Pump-probe and QCL spectrometer are based on lasers and have a high temporal resolution. While FTIR methods cover only the later time region but measuring the entire spectral range.

2.2.2 FTIR absorption spectra of proteins

A typical IR absorption spectrum of ChR2 in detergent is shown in Fig. 2.6 showing some prominent absorption bands of the protein backbone. The $N-H$ stretching vibration is around 3300 cm^{-1} and 3170 cm^{-1} (amide A and B, respectively) and overlaps with the $O-H$ stretching vibration of water. The amide I vibration at around 1650 cm^{-1} arises mainly from $C=O$ stretching plus minor contribution from $N-H$ in-plane bend, CCN deformation and $C-N$ stretching vibrations. The amide II band is around 1550 cm^{-1}, which is a combination mode of the out-of-phase vibration of $N-H$ in-plane bend and the $C-N$ stretch with minor contributions of the $C-C$ stretching vibration. And finally, the amide III vibration from 1400 to 1200 cm^{-1} is the in-phase combination of the $N-H$ bend and $C-N$ stretch mode with minor contribution of $C-C$ stretching and $C=O$ in plane bending vibration. For further information of vibrational modes of amino acids and the protein backbone see Barth and Zscherp (2002) [83].

As indicated in the Fig. 2.6, the protein environment (detergent) gives also rise to prominent absorption bands, overlapping with the protein absorption at around 2900 cm^{-1} ($C-H$ stretch) and 1100 cm^{-1} ($C-O$ stretch). Vibrations of water molecules also overlap with the protein vibrations in the amide A and B region as well as in the amide I region (Fig. 2.6). For IR studies of proteins this is an important aspect, because the noise in these regions is increased. Thus, the concentration of water and detergent is reduced (see section 2.2.4).

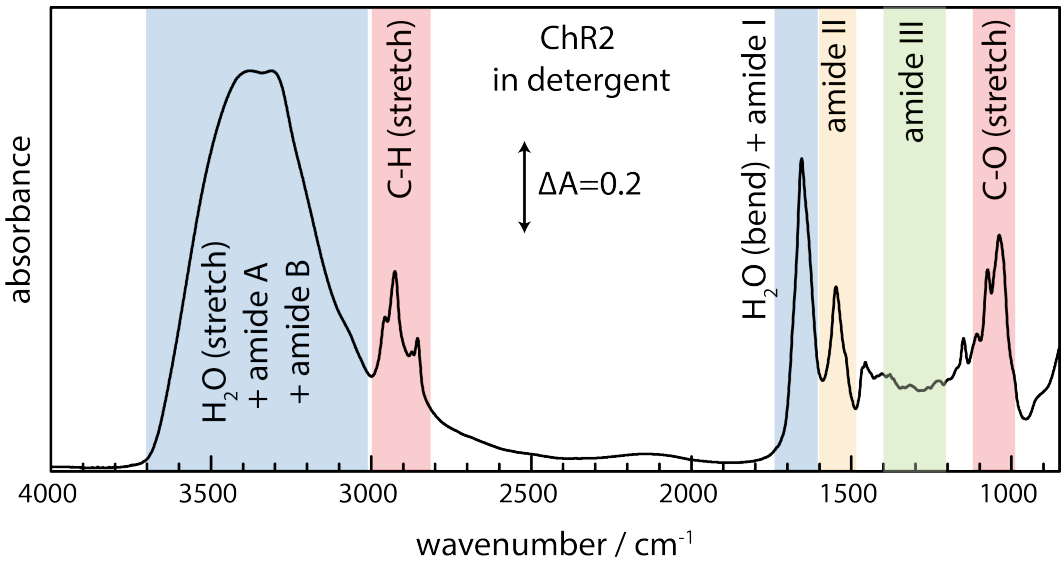

Fig. 2.6: Absorption spectrum of a rehydrated ChR2 protein film measured in transmission. This spectrum is characteristic for other membrane proteins, which were solubilized in detergent. The main contribution of specific vibrational modes of water/protein (blue), detergent/protein (red) and protein (blue, orange, green) are highlighted.

Steady-state FTIR difference spectroscopy

Difference spectroscopy is necessary to observe small vibrational differences between the ground state and intermediate states. The absorption is calculated according to equation 2.2. Here, I_0 is the single channel of the ground state and I is the single channel of the intermediate state. In a steady state experiment intermediate states are trapped (by freezing or accumulation). Time-resolved IR spectroscopy (e.g. QCL, step-scan and rapid scan FTIR) detects changes in vibrational modes are over time.

Rapid scan FTIR spectroscopy

In a rapid scan experiment, the moveable mirror moves very fast forward and backward, i.e. a whole interferogram is taken with a high repetition frequency. The time-resolution of rapid scan FTIR is limited by the movement speed of the mirror, which is here 10 ms (but could be longer, depending on the time for a break to change the direction). Time-resolved rapid-scan FTIR experiments for rehydrated samples dissolved in H_2O and D_2O, respectively, were performed using a Vertex 80v spectrometer (Bruker Optics, Ettlingen, Germany). The repetition rate of the pulsed laser was set to 0.01 Hz, and the interferograms are recorded every 10 ms and logarithmic averaged, thus spanning the time range from 5 ms to 90 s. The resolution was set to 8 cm^{-1}.

Step-scan FTIR spectroscopy

The step-scan method works different in comparison to rapid scan. The moveable mirror steps to a specific interferogram point and the kinetic is measured. The mirror moves subsequent to the next interferogram point and an additional triggering of the reaction cycle starts until the kinetics at every interferogram point are taken (see Fig. 2.5). This method has a time resolution up to the ns time scale, which is mainly limited by the responds time of the detector. The disadvantage is the sensitivity for external vibrations (noise) and the long measuring time. In addition, the mirror stability is a critical part of this method. Therefore, extra time is needed after each step to stabilize the mirror. This method is most useful for fast cyclic photo-induced rections, like in bR. Slow or non-cyclic reactions are more difficult to measure.

Here, the pulsed laser excitation was performed under the same conditions as for time-resolved UV/Vis experiments. Multiexponential fitting of transients at single

wavenumbers was performed by ORIGINPRO (OriginLab, Northampton, MA) and by a home-written Matlab routine. After data acquisition, the time-resolved IR spectra were quasilogarithmically averaged to 20 spectra per decade and offset to zero in the range of 1820 to 1780 cm^{-1}. The step-scan and rapid-scan data were merged and noise-filtered by singular value decomposition (SVD), retaining the first five major components. Fourier self-deconvoltion (FSD) and global fitting were applied [5].

2.2.3 Time-resolved QCL spectroscopy

Time-resolved IR spectroscopy with IR lasers was performed on a home-built spectrometer (by Bernd Schultz) using tunable QCLs (an external cavity QCL run in continuous mode; Daylight Solutions, San Diego, CA). The continuous monochromatic emission of the QCL was directed through the sample. The transmitted intensity was recorded by a photovoltaic MCT detector (KV104 Series, 50 MHz; Kolmar Technologies, Newburyport, MA). The detector output was amplified (KA-050 Series; Kolmar Technologies, Newburyport, MA) and divided into two separate channels. Both channels were digitized by picoscopes (4227 Series; PICO Technology, St. Neots, Cambridgeshire, UK) with the first running at a sampling frequency of 250 MHz and the second at 1 MHz. The time-resolution of the detection system, limited by the detector/preamplifier system response time, was determined to be 10-15 ns [52]. A quantity of 50,000 pretrigger points were recorded (corresponding to 200 μs and 50 ms, respectively) before the exciting laser flash and were stored as reference intensity. The photocycle of the sample was triggered by 10-ns laser pulse at 450 nm, see Fig. 2.7.

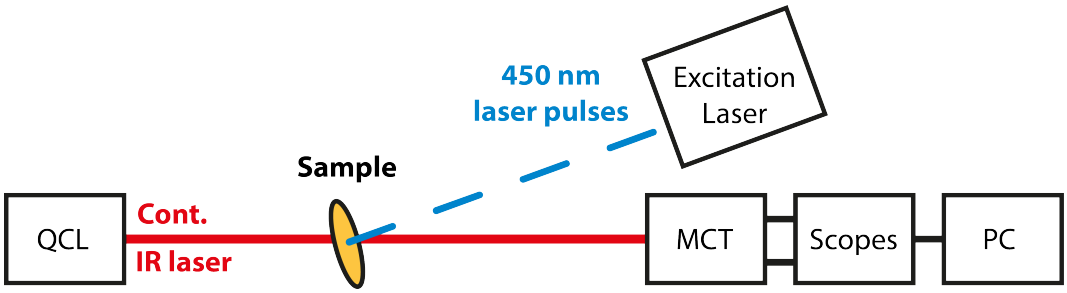

Fig. 2.7: Schematic representation of our home-build QCL spectrometer. The tunable QCL runs a continuous mode at a specific wavenumber. The sample is excited like in the other time-resolved experiments, as described above.

Transient absorbance changes after light excitation were calculated by the Labert-Beer law, by taking the negative logarithm of the ratio of the intensity after the exciting laser pulse and the mean average intensity in the pretrigger range. The linear equidistant data points were logarithmically averaged and reduced to 100 points per decade. Each kinetic was 35 times recorded and averaged to improve

the signal-to-noise ratio. The experiment was repeated to cover the frequency range from 1600 to 1700 cm^{-1} in 200 steps. A second QCL head was used for the range of 1690 to 1780 cm^{-1}. Due to the lower background absorption in this frequency range, the sample thickness was doubled (increasing the optical path length), which increased the absorption in these experiments. The emission frequency of the QCL was tuned by 0.5 or 1 cm^{-1} steps for D_2O and H_2O, respectively. The overlapping spectral region (1690-1700 cm^{-1}) was used to match signal amplitudes in both data sets, which resulted in a merged dataset covering the range of 1600 to1780 cm^{-1}. The data was multiplied by a Gaussian in Fourier space to generate spectra at 4 cm^{-1} nominal resolution, (see Resler et al. 2015 [34] for further information). In collaboration with Bernd Schultz I performed QCL experiments. The recorded IR data were subjected to singular-value-decomposition analysis (SVD). Here, the QCL data set was reconstructed with six singular-value-decomposition components. Transients from QCL and rapid-scan FTIR experiments were merged when monitoring changes later than 300 ms.

2.2.4 Sample preparation for IR spectroscopy

Purified protein of ChR2 and its variants are provided by the laboratory of Ramona Schlesinger (Freie Universität Berlin) and Ernst Bamberg (MPI of Biophysics, Frankfurt). The ChR2 samples for IR spectroscopy are solubilized in detergent. For ideal protein films I concentrated the sample to 4 mg/mL, dried on a BaF_2 window and rehydrated over the vapor phase generated by a glycerol/water mixture (3:7 weight/weight). Before drying, the detergent concentration was reduced to 2%. This was controlled by an attenuated total reflection (ATR) FTIR experiment of the liquid sample and compared to reference spectra of different detergent concentrations. H/D exchange was achieved using a 2:5 (weight/weight) mixture of a deuterated glycerol and deuterium oxide mixture. The samples were measured at 24 $^{\circ}C$ and at pH 7.4 and pD 7.8, respectively.

Here, I measured ChR2-wt and the following variants: E90A, R120H, E123T, D156E, D156N, D253E and D253N. The visible absorption spectra of the last five variants and WT are shown in Fig. 2.1. All variants and the ChR2-wt are truncated ChR2 (1-315) from *Chlamydomonas reinhardtii*.

Results

3

Two different aspects of ChR2 are characterized: The protonation dynamics and the structural changes. Both aspects can be observed by time-resolved IR difference spectroscopy and are complimented by time-resolved UV/Vis difference spectroscopy. As shown in Fig. 3.1a time-resolved FTIR data are measured from 6 μs to 100 s after photoexcitation by a 10 ns laser pulse at 450 nm, scanning the spectral range from 900 cm^{-1} to 1820 cm^{-1}. Negative absorption changes (blue) correspond to vibrational modes in the ground state and positive absorption changes (red) correspond to vibrational modes in the intermediate states. By time-resolved UV/Vis spectroscopy the corresponding photointermediates were determined (Fig. 3.1b, same color coding).

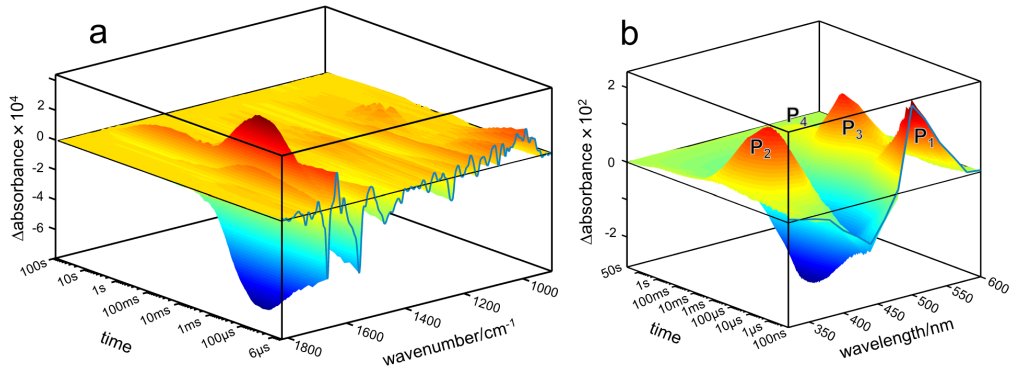

Fig. 3.1: Overview of the time-resolved absorbance changes after photoexcitation of ChR2. Time-resolved difference spectra in the IR (a) and UV/Vis (b) range. Negative and positive absorption changes are colored blue and red, respectively [5].

The specific time points of maximum accumulation of these intermediates are 6 μs, 300 μs, 6 ms and 300 ms for the P_1^{500}, P_2^{390}, P_3^{520} and P_4^{480} state. The extracted IR (a) and UV/Vis (b) spectra at these time points are shown in Fig. 3.2. The difference spectrum of the P_1^{500} intermediate shows a strong negative peak at 1663 cm^{-1} indicating early structural changes of the protein backbone. This vibrational band is described in more detail in section 3.6. The negative peak at 1554 cm^{-1} is due to the ethylenic stretching mode ($C = C$) of all-$trans$ ground state retinal; it correlates well with the absorption maximum in the visible range at 470 nm [84]. The corresponding $C - C$ stretching modes of the all-$trans$ retinal are observed as negative peaks at 1240, 1200 and 1154 cm^{-1}. Both observations support that the photocycle origins mainly from photoisomerization of the all-$trans$ retinal [85].

The positive and asymmetric band at 1173 cm^{-1} with a shoulder at 1188 cm^{-1} reflects the $C_{14} - C_{15}$ stretching mode of the 13-*cis* retinal. The positive band at 986 cm^{-1} corresponds to the hydrogen-out-of-plane (HOOP) vibration. It indicates a non-planar conformation of the retinal in the early red-shifted intermediate, like for other microbial rhodopsins [86–88].

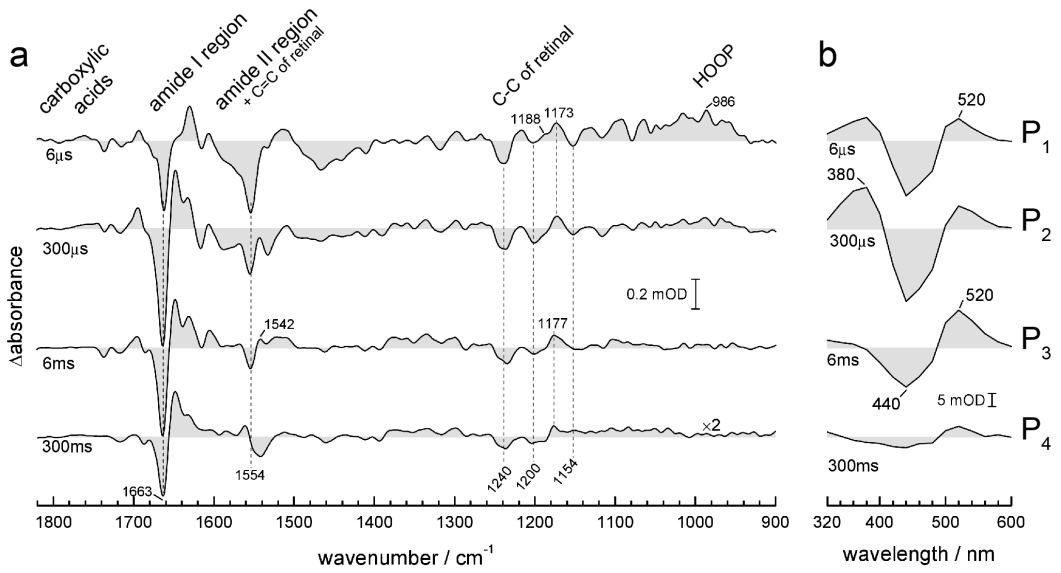

Fig. 3.2: Time-resolved absorbance difference spectra at selected times after photoexcitation in the IR (a) and UV/Vis (b) region. The times are chosen to reflect distinct intermediate states P_1^{500} (6 μs), P_2^{390} (300 μs), P_3^{520} (6 ms) and P_4^{480} (300 ms). Here, mOD refers to a change in absorbance of 10^{-3} [5].

Analysis of a 3D data set and the drawn conclusions are complex. Therefore, specific spectral ranges are discussed separately in more detail. Vibrational modes were identified by point mutation of single amino acids, isotopic exchange of the solvent, infrared spectra of model compounds, and literature studies.

3.1 Protonation dynamics

Within Channelrhodopsin-2 (ChR2), protonation dynamics including hydrogen bond changes as well as de- and reprotonation events, can be observed by absorption changes of specific amino acids. During the transition between P_1^{500} and P_2^{390} the Schiff base (SB) of ChR2 gets deprotonated and between P_2^{390} and P_3^{520} reprotonated [6]. Although proton transfer reactions from the protonated SB were observed by UV/Vis spectroscopy, the primary proton accepting groups were still missing. Only some amino acids may act as primary proton acceptor or donors, related to their specific chemical ability to accept or release a proton. Especially carboxylic acids

are prime candidates for such residues as found for other microbial rhodosins where proton transport was observed, for example bacteriorhodopsin (bR) [28, 89]. Only protonated carboxylic acids shows a characteristic frequency of the $C = O$ stretching vibration in the range of 1690 to 1780 cm^{-1} [90, 91]; a spectral region that shows hardly any contributions from other vibrational modes [83]. In addition, FTIR difference spectroscopy highlights only these carboxylates that undergoes hydrogen bond changes or de- and reprotonation events. In ChR2, four positive bands at 1760, 1745, 1728 and 1695 cm^{-1} and two negative bands at 1737 and 1717 cm^{-1} are identified after 6 μs, as shown in Fig. 3.3a. The band assignment and their relevance in the proton transfer mechanism are discussed next.

3.1.1 Primary proton donor to the Schiff base: D156

If the primary proton donor of the SB is a protonated carboxylic group, the rise and the decay kinetic of a $C = O$ stretching band has to be negative and must match with the P_3^{520} state formation. Although two negative peaks can be observed at 6 ms (Fig. 3.3a), only the kinetic of the band at 1737 cm^{-1} correlate with the P_3^{520} intermediate observed by time-resolved UV/Vis spectroscopy (Fig. 3.3b). By point mutation we can identify the amino acid, which relates to the observed changes in vibrational modes. The conservative variant D156E shows in the P_3^{520} state a spectral upshift of 26 cm^{-1} (from 1737 to 1763 cm^{-1}, see Fig. 3.3d). In the P_2^{390} state of the D156A variant, two positive bands at 1760 and 1745 cm^{-1} and the negative band at 1737 cm^{-1} (Fig. 3.3d, marked by asterisks) are missing. Therefore, the two positive bands and the negative band, observed in the P_1^{500} and P_2^{390} intermediates can be assigned to hydrogen bonding changes of D156. And the prominent negative band during the P_3^{520} state at 1737 cm^{-1} origins from deprotonation of D156. Thus, D156 is identified as the primary proton donor to the retinal SB. In both variants (D156E and D156A) the negative band at 1717 cm^{-1} and the positive band at 1728 cm^{-1} are not affected but missing in the E90A variant [5]. Thus, supporting the assignment as $C = O$ stretching vibration of E90, as assigned by Ritter et al. [7].

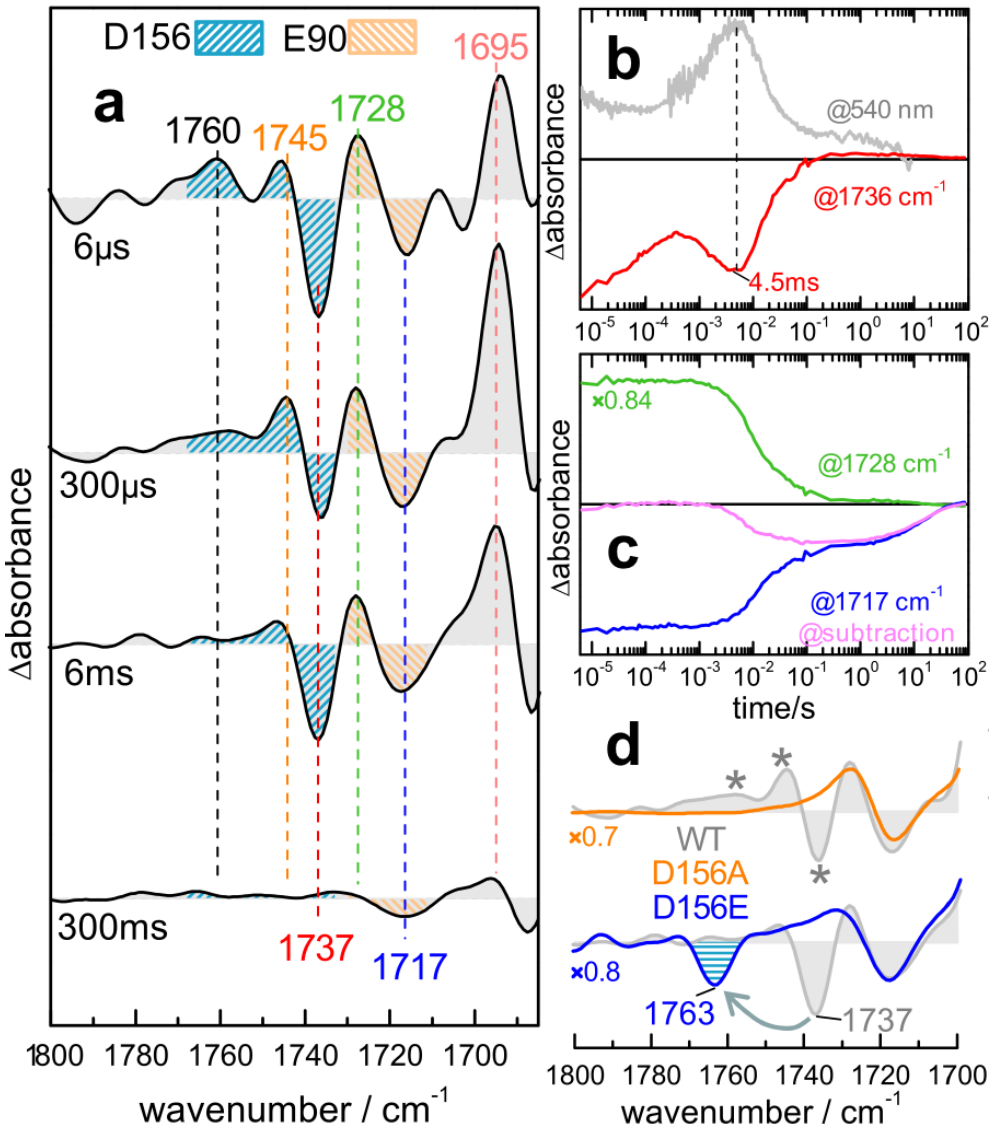

Fig. 3.3: Carboxylic region of ChR2. Assignement of $C = O$ stretching modes to D156 and E90 by point mutation. (a) Four extracted IR difference spectra of the carboxylic region reflecting different intermediate states at indicated times. The bands assigned to D156 and E90 are colored in blue and orange, respectively. (b) Comparison of the rise and decay kinetic of the P_3^{520} at 540 nm and the IR band at 1736 cm^{-1}. Both showing a maximum at 4.5 ms after laser excitation (dashed line). (c) Kinetics of the IR bands at 1728 and 1717 cm^{-1} as well as the subtraction colored in green, blue and pink, respectively. (d) Band assignment by point mutation D156A (upper) and D156E (lower) [5].

Conclusively, point mutations of the primary proton donor D156 should alter the photocycle and may effect the channel functionality. In the D156E variant, the P_2^{390} decay is accelerated and less intense as in WT, i.e. the reprotonation of the retinal SB was accelerated. The P_3^{520} decay is 10-fold delayed (Fig 3.4), i.e. the reprotonation of E156 is delayed. Both effect may origin from a lower proton affinity in this variant. Interestingly, this variant shows a delayed channel opening and closing kinetic, observed by time-resolved electrophysiology [5]. Furthermore, it was shown by Bamann et al. [92] that the photocycle kinectics of the D156A shows a long living P_2^{390} intermediate and a 10^{-4}-fold delayed reprotonation dynamic of the SB and the cation permeation was delayed in a similar order. Therefore, it can be concluded that the reprotonation of D156 is crucial for channel closing. A detailed analysis of pore formation and closure is discussed in section 3.6.

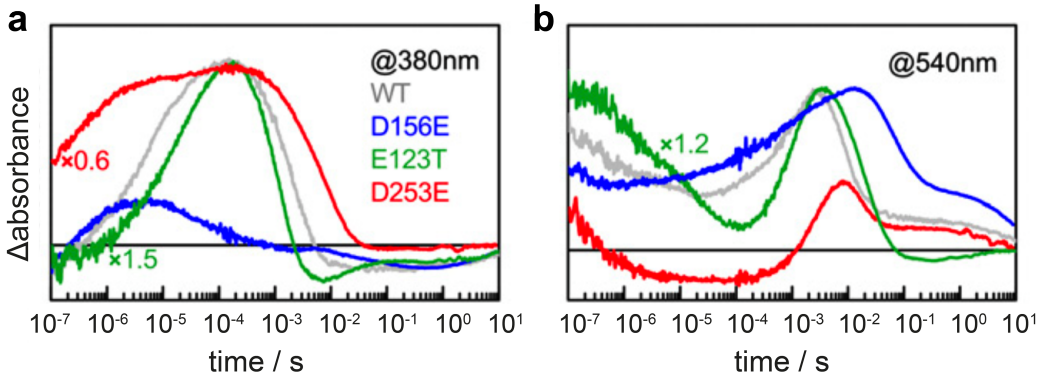

Fig. 3.4: Time-resolved absorbance changes after blue light excitation of WT ChR2 (grey) and its variants D156E (blue), E123T (red) and D253E (green). Kinetics are measured at 380 nm (a) and 540 nm (b), representing the P_2^{390} and P_3^{520} state [5].

3.1.2 Protonation changes of E90

The negative and positive bands at 1728 cm^{-1} and 1717 cm^{-1} were previously assigned to hydrogen bond changes of the protonated amino acid E90 in the P_4^{480} intermediate [7]. This is in agreement with our observed time-resolved step-scan FTIR data of E90A in the P_2^{390} and P_3^{520} intermediate ([5], SI Fig. S4). The kinetic analysis of the band at 1728 cm^{-1} shows a positive absorbance plateau starting before 6 μs and decaying mono exponentially (Fig. 3.3c, green). The early phase is mirrored by the kinetic of the band at 1717 cm^{-1} (Fig. 3.3 c, green). This suggests an early change in the $C = O$ stretching vibration of the protonated carboxylic group of E90. In contrast to 1728 cm^{-1} the band at 1717 cm^{-1} decays in biphasic manner that may origin from a late deprotonation event of E90. The late deprotonation event is more clearly observed by subtraction of these bands as shown in magenta (Fig. 3.3c). These kinetics follows the rise and decay of the closed (desensitized) P_4^{480} state. These findings are also supported by ns IR flash photolysis experiments upon H/D exchange in section 3.2 and by pH indicator experiments in section 3.3.

3.1.3 Primary proton acceptor of the Schiff base: D253

The primary proton acceptor must be in close distance of the Schiff base. The crystallographic structure of the C1C2 chimera reveals two deprotonated carboxylic acids named E123 and D253, which are located 3.4 and 3.0 Å away from the SB [31]. If one of these residues gets protonated the $C = O$ stretching vibration occurs, which results in a positive absorption change in the difference spectrum of the P_2^{390} state (see Fig. 3.3a at 300 μs). Four positive bands can be observed in this region at 1760, 1745, 1728, and 1695 cm^{-1}. The first three are identified as changes in hydrogen bonding of D156 and E90 as discussed above. The only remaining band is at 1695 cm^{-1}, which is unusually low in comparison to other rhodopsins [5]. But in wild type (WT) these band correlate with the rise of the P_2^{390} state (3.5b).

The position of the residue E123 is equivalent to D85 in bR, which acts as the primary proton acceptor in this homologue protein. The D85T variant shows strong kinetic and functional effects [93]. In contrast, the variant E123T in ChR2 (also known as ChETA) exhibits only minor spectral and kinetic changes at the P_2^{390} and P_3^{520} state. This is in agreement with the preserved channel functionality [10]. Only the appearance of the band at 1712 cm^{-1} differs in comparison to wild type (see Fig. 3.5a, top). The kinetics tallies with the P_2^{390} rise (Fig. 3.5c). The amplitude of the band at 1695 cm^{-1} is also decreased, indicating a downshift in frequency related to changes in hydrogen bonding.

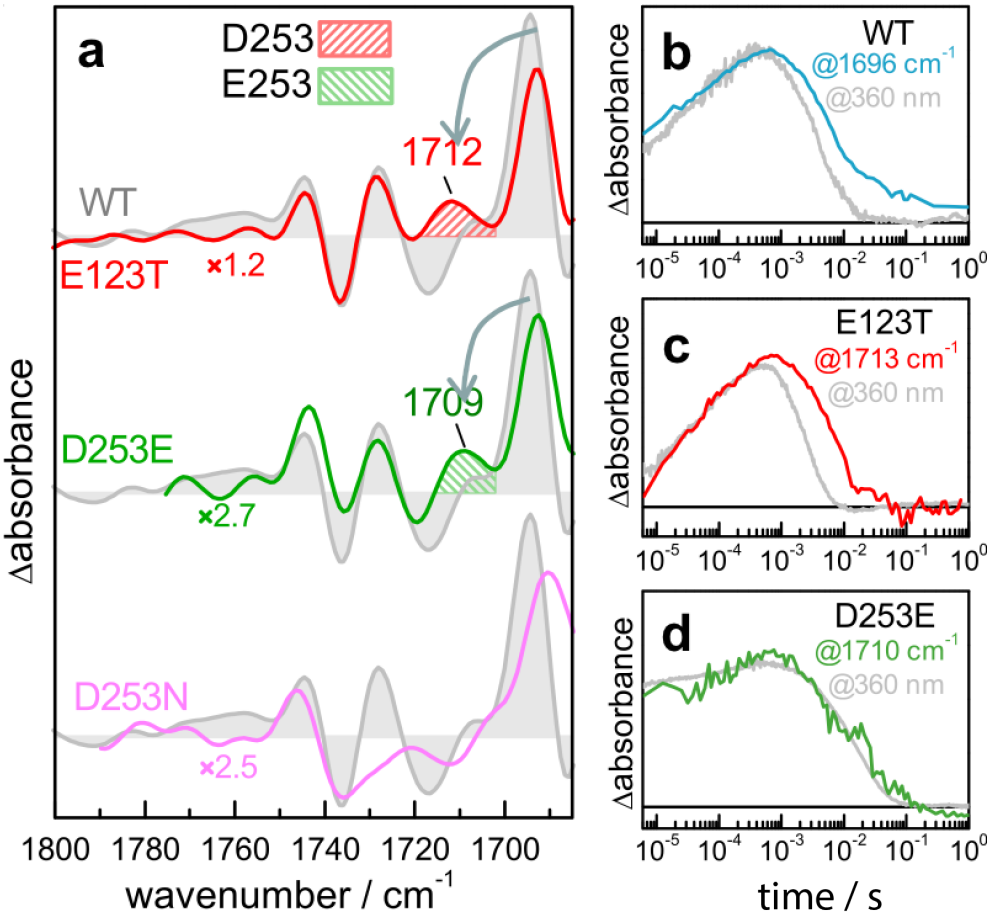

Fig. 3.5: Identification of primary proton acceptor of the retinal SB. (a) FTIR difference spectra of the carboxylic region representing the P_2^{390} state of E123T (red), D253 (green), and D253N (magenta). All spectra are scaled to the ChR2-wt data (grey). Band shifts are indicated by arrows. (b) Transient absorption changes at 1696 cm^{-1} (blue) of ChR2-wt and compared to 360 nm (grey), reflecting the P_2^{390} rise and decay kinetic. (c) Comparison of the transient absorption changes of E123T at 1713 cm^{-1} (red) and at 360 nm (grey). (d) Comparison of the transient absorption changes of D253E at 1710 cm^{-1} (red) and at 360 nm (grey). (b-d) the kinetics are scaled to match the intensity of the trace at 360 nm [5].

However, the variant D253E shows a notable 50-fold accelerated rise and a 3-fold delayed decay of the P_2^{390} intermediate leading to a delay and low accumulation of the P_3^{520} state (see Fig. 3.4). The difference spectrum in the infrared shows a new positive band appearing at 1709 cm^{-1} and a decrease in amplitude of the band at 1695 cm^{-1} (Fig. 3.5a, middle). Indicating an upshift of the $C = O$ stretching vibration upon conservative exchange of aspartic to glutamic acid. This frequency tallies also with the P_2^{390} rise and decay (Fig. 3.5d). The variant D253N shows drastic changes in the carboxylic region (Fig. 3.5a, bottom). The missing positive and negative bands at 1728 cm^{-1} and 1717 cm^{-1} suggesting a change in the pKa value of E90. In addition, the positive peak at 1695 cm^{-1} is also reduced and a

positive peak around 1710 cm^{-1} is not appearing. Therefore, the band at 1695 cm^{-1} is identified as the $C = O$ stretching vibration of D253, which acts as the primary proton acceptor. Consequently, the D253N variant is non-functional in contrast to E123T and D253E.

3.2 Spectroscopy of ChR2 upon H/D exchange

The excitation and therefore the structural and electronic changes of ChR2 are induced by a 10 ns laser pulse. The corresponding photoreaction was recorded in the UV/Vis and mid-IR ranges and the kinetics were analyzed from 50 ns on. Kinetic and vibrational isotope effects were determined by comparing experiments in D_2O conducted on samples hydrated either with H_2O or with D_2O. This chapter is based on Resler et al., 2015, *Biophysical Journal* [34].

3.2.1 Deuterium KIEs observed in the visible range

The reaction intermediates of ChR2, as for any other rhodopsins, are characterized by the energy of the absorption maximum of retinal and summarized in a photocylce. The corresponding wavelength varies among intermediate states due to changes in the protonation state of the retinal Schiff base and/or conformational changes of the retinal cofactor. It has been shown that the transitions between the intermediates of ChR2 involve proton transfer reactions (see section 3.1). Therefore, proton transfer may be a rate-limiting step in the photocycle kinetics of ChR2, expected to exhibit altered kinetics upon H/D exchange. Transient absorption changes are measured in the UV/Vis range of ChR2 immersed in H_2O (Fig. 3.6, black trace) and in D_2O (red trace). Specific kinetics are recorded at 380 nm, which are characteristic for the formation and decay of the blue shifted P_2^{390} state. At 520 nm the decay of the red-shifted P_1^{500} and the formation and decay of the red-shifted P_3^{520} states are monitored. Finally, at 480 nm the recovery of the bleached ground state is observed.

A global exponential fit analysis was performed to obtain time constants, including kinetics recorded at 360, 380, 440, 480, 520 and 540 nm in H_2O and in D_2O. In addition, maximum entropy lifetime distribution analysis was applied to the kinetics of ChR2 in H_2O, D_2O, and in an equimolar mixture of H_2O/D_2O at two selected wavelengths at 380 nm (Fig. 3.7), and at 520 nm (Fig. 3.7), giving a visual perception of the magnitude of the KIE for each exponential component. The results

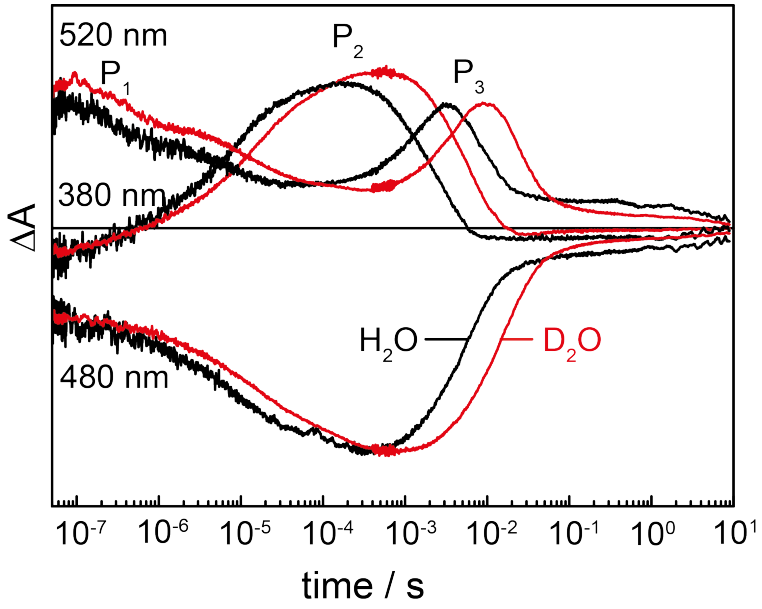

Fig. 3.6: Transient absorption changes in the UV/Vis range after pulsed excitation of ChR2 in H_2O (black traces) and D_2O (red traces). The sample was thermostated at 25° C and at a pH 7.4 or pD 7.8, respectively. ground state recovery was probed at 480 nm, the red-shifted intermediates (P_1^{500}, P_3^{520} and P_4^{480}) at 520 nm and the blue-shifted intermediate (P_2^{390}) at 380 nm [34].

of both fitting methods are summarized in Tab. 3.1 and compared to published data of the photocycle intermediates of the proton-pumping protein bR. The KIEs derived from lifetime distribution analysis are shown in parenthesis and will be used in the further discussion.

In H_2O, the rise of P_2^{390} is multi-exponential with a dominant phase of $\tau = 8\ \mu s$ (70% of the amplitude), while the decay is clearly mono-exponential with $\tau = 2\ ms$ (Fig. 3.7, black trace). P_3^{520} also rises mono-exponentially with $\tau = 1.5\ ms$, and decays mono-exponentially with $\tau = 6\ ms$ (Fig. 3.7, black trace). The absorption of the P_1^{500} state decays in several phases (Fig. 3.7, black trace). The fast decaying component with $\tau = 300\ ns$ is assigned to a transition between two P_1^{500} intermediates that is silent in the E123T variant of ChR2 [52]. P_1^{500} further decays with $\tau = 8\ \mu s$ matching the main rise of the P_2^{390} state. Finally, the P_4^{480} decays with $\tau = 19\ s$, which was determined by rapid-scan FTIR at 1242 cm^{-1} reflecting the ground state recovery [5]. Though weak in intensity, the continuous light used to detect absorbance changes in the visible, may lead to photoconversion of the P_4^{480} state back to the initial ground state, particularly when the lifetime is very long. At this stage, the much lower energy of IR radiation is certainly more appropriate when the time constant of the decay of the P_4^{480} state is determined (*vide infra*).

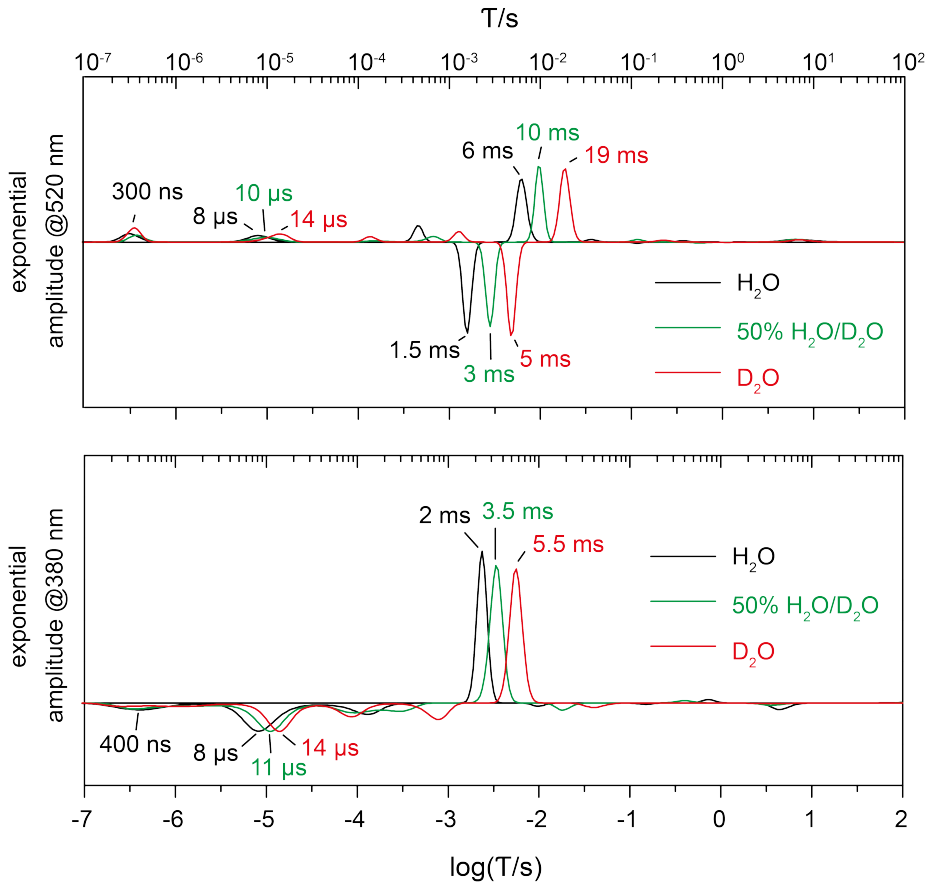

Fig. 3.7: Maximum entropy lifetime distribution of transient absorption changes of ChR2 in H_2O (black), 50 % H_2O/D_2O (green) and D_2O (red) measured at (top panel) 520 nm and (bottom panel) 380 nm. Components discussed in the text are labeled by their time constant [34].

KIEs were derived from the ratio of the time constants of ChR2 dissolved in H_2O and in D_2O. A KIE of 1.8 was determined for the P_1^{500} to P_2^{390} transition (Table 3.1). This is in contrast to bR in PM which exhibits a much larger KIE of 5.6 for the main step in the formation of the M state, despite the fact that the retinal Schiff base gets deprotonated in both intermediate states. The KIE for P_3^{520} formation and decay are 3.3 and 3.2, respectively. These may be compared to the M to N and N to O state transitions of bR showing weaker KIEs of 1.7 and 1.5, respectively. The ground state recovery kinetics of ChR2 exhibited with 2.6, which indicates a proton transfer reaction to be rate-limiting in the recovery of ChR2 (Table 3.1).

Tab. 3.1: Time constants for transitions of photocycle intermediates as derived from lifetime distribution (in parentheses) and multi-exponential global fitting of transient absorption changes of ChR2 at 360, 380, 440, 480, 520 and 540 nm after blue light (450 nm) excitation. The sample was measured in H_2O and D_2O and the KIE is given by the ratio of the time constants. The KIEs characterizing the transitions of the various intermediate states of the bacteriorhodopsin (bR) photocycle were taken from [40, 94–97]. Because the rise of the M intermediate in bR is multi-exponential, the KIE for the formation of M is given for the component with the largest amplitude. The KIE of the recovery of ground state ChR2 was determined by rapid-scan FTIR as described by Lórenz-Fonfría et al. [5]. The back reaction from the P_4^{480} state is derived from multi-exponential fitting of the rapid-scan FTIR spectroscopic data at 1242 cm^{-1} and marked with an asterics [34].

ChR2 transitions	τ (H_2O)	τ (D_2O)	KIE of ChR2	bR transitions	KIE of bR
$P_1^{500} \rightarrow P_2^{390}$	8 µs (9.6 µs)	14 µs (17 µs)	1.8 (1.8)	L → M	4.6-5.6
$P_2^{390} \rightarrow P_3^{520}$	1.5 ms (2.3 ms)	5 ms (7.0 ms)	3.3 (3.0)	M → N	1.7-1.8
$P_3^{520} \rightarrow P_4^{480}$	6 ms (6.4 ms)	19 ms (18 ms)	3.2 (2.8)	N → O	1.5-2.0
$P_4^4 \rightarrow$ ChR2*	19 s	49 s	2.6	O → bR	1.5-2.0

3.2.2 Time-resolved IR absorbance changes of ChR2

Visible spectroscopy is well-suited to identify intermediates of the ChR2 photocycle based on the electronic changes in the retinal cofactor but structural changes of the surrounding opsin moiety are spectrally silent. To address this, the photoreaction of ChR2 was recorded by transient absorption spectroscopy in the mid-IR range. A novel IR spectrometer employing tunable quantum cascade lasers (QCL) were developed in our group. Here, kinetic traces are recorded with a temporal resolution of 15 ns. The tunability of the QCL allows to measure across a broad frequency range. As an example of the fidelity of the recorded data, the left panel in Fig. 3.8 provides an overview of the photo-induced transient absorbance changes of ChR2 in the amide I region (predominantly $C = O$ stretching vibration of the peptide bond in the spectral range between 1600 cm^{-1} and 1690 cm^{-1}). The QCL data are validated by time-resolved FTIR spectroscopy using the step-scan technique (right panel of Fig. 3.8, data were taken from [5]). The latter data have been recorded at lower time resolution (6 μs). Overall, the data exhibit close agreement. Clearly, the QCL approach provides higher time resolution, but a broader spectral range is covered by step-scan FTIR spectroscopy [26, 98].

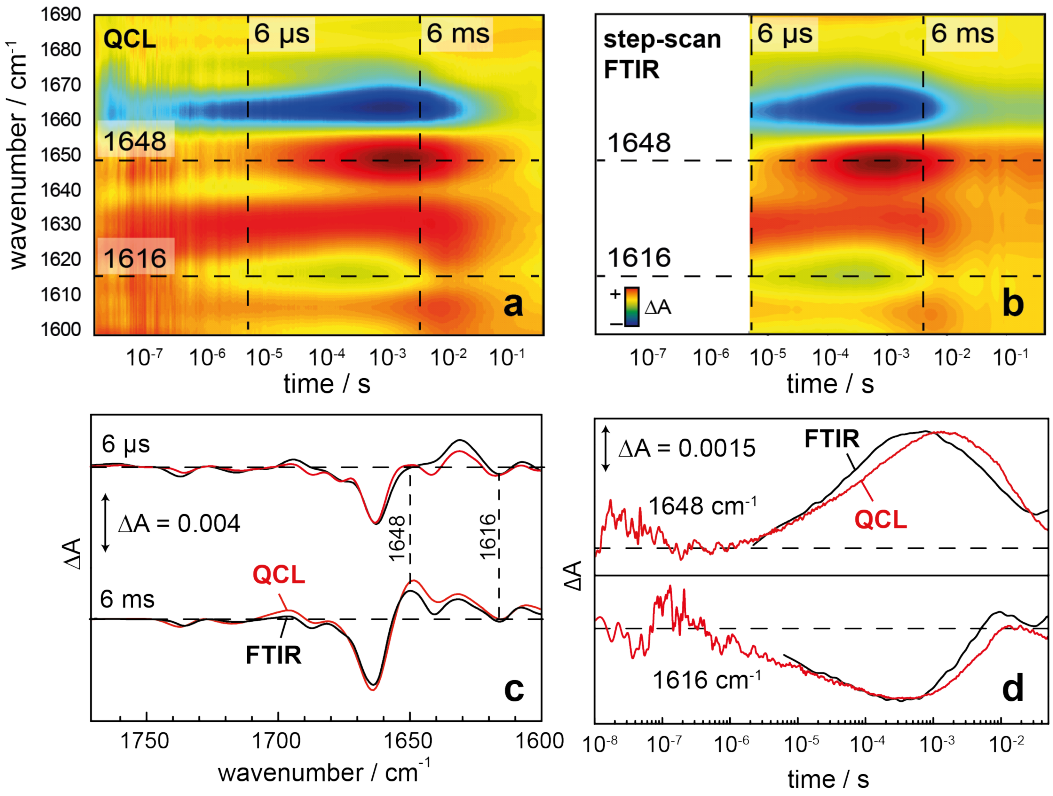

Fig. 3.8: Contour plot of transient absorbance changes of ChR2 in the amide I region (of 1600-1690 cm^{-1}) recorded with the novel QCL spectrometer (a) and by step-scan FTIR spectroscopy (b). The latter data have been taken from [5]. The logarithmic time axis covers the range from 20 ns to 300 ms. Negative and positive absorption changes are indicated in blue and red, respectively. Dashed horizontal lines indicate bands at specific wavenumbers (1648 cm^{-1} and 1616 cm^{-1}) and vertical lines indicate time specific points (6 μs and 6 ms) as discussed in the text. (c-d) Comparison of the time-resolved IR data recorded by QCL (red) and step-scan FTIR spectroscopy (black) [34].

For a detailed inspection, we extracted difference spectra at 6 μs and 6 ms after the exciting laser pulse (dashed vertical lines in Fig. 3.8) as recorded by QCL (Fig. 3.8c, red spectrum) and step-scan FTIR spectroscopy (black spectrum), respectively. The comparison reveals close agreement between both spectroscopic methods. Minor deviations in the region around 1630 cm^{-1}, 1640 cm^{-1} and 1700 cm^{-1} are the result of the higher spectral resolution of the QCL setup (4 cm^{-1} vs. 8 cm^{-1} of the FTIR data). Two time traces at 1648 cm^{-1} and 1616 cm^{-1} (dashed horizontal lines in Fig. 3.8a-b) were extracted to show the transient absorption changes recorded with the dispersive QCL setup and by step-scan FTIR spectroscopy (Fig. 3.8d). Overall, the kinetics agree well with minor deviations to be accounted for the different spectral resolutions used (*vide supra*).

3.2.3 Deuterium isotope effects in the carboxylic region

After validation of the QCL setup, time-resolved IR difference spectroscopy was used to study the absorption changes between 1690 cm^{-1} and 1775 cm^{-1} range (3.9). In this frequency range, transient protonation and hydrogen-bonding changes of acidic amino acids (aspartic and glutamic acids) have previously been reported for ChR2, albeit at lower time resolution [5, 7, 35, 45, 52]. Two isotope effects induced by the H/D exchange must be discriminated in the analysis of time-resolved data. Firstly, the vibrational frequency of $C = O$ stretching modes are downshifted by 5-20 cm^{-1} due to the increase in reduced mass induced by the heavy isotope [91]. The frequency downshift of the $C = O$ stretch comes about the coupling to the $O - H$ bending vibration, which is lost when the hydroxyl of the carboxylic group is deuterated [91]. Secondly, the increased mass of the isotope leads to a deceleration of the kinetics of the vibrational bands that are associated with proton transfer reactions [99]. Thus, the analysis of isotope effects in time-resolved IR experiments is complex. Fig. 3.9 shows the time-resolved IR differences of ChR2 in H_2O (left panel) and in D_2O (right panel). Dashed horizontal lines in the contour plot indicate specific bands at the wavenumber of their maximum absorbance change. The vertical line indicates the time at which the P_3^{520} state of the ChR2 photocycle has maximal accumulation. This photocycle intermediate state is of particular relevance as ion permeation takes place during its lifetime.

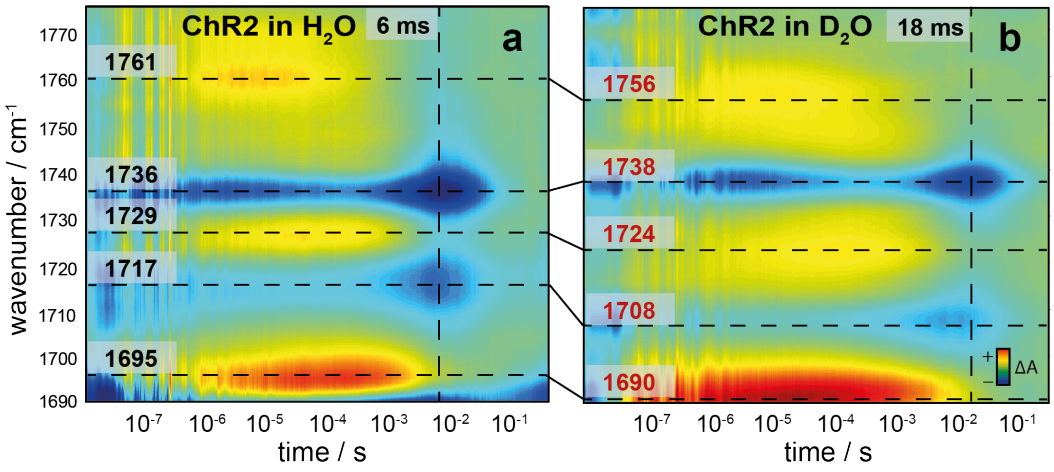

Fig. 3.9: Contour plot of the IR absorption differences of ChR2 in H_2O (left, A) and D_2O (right, B) in the carboxylic region from 1690 cm^{-1} to 1775 cm^{-1}. Positive and negative absorbance changes are colored in red and blue, respectively. Dashed horizontal lines indicate the maxima and minima of difference bands at particular wavenumbers as discussed in the text. The vertical line indicates the time for maximal accumulation of the P_3^{520} state [34].

The intense positive band (red contour in Fig. 3.9a) at 1695 cm^{-1}, to which the $C = O$ vibration of the primary acceptor of the Schiff base proton, D253, contributes (7), is downshifted in frequency by 4 cm^{-1} upon H/D exchange. As this vibrational band contains spectral contributions from overlapping vibrations other then the $C = O$ stretch of D253, the determination of the KIE of its rise and decay kinetics is pointless. The negative and positive vibrational bands at 1717 cm^{-1} and 1729 cm^{-1} (Fig. 3.9a) are shifted by 9 cm^{-1} and 5 cm^{-1} wavenumbers in D_2O (Fig. 3.9b), respectively. These two bands have been assigned to changes in hydrogen bonding of the $C = O$ group of protonated E90 [5, 7, 45]. The negative band at 1736 cm^{-1} was assigned to the $C = O$ vibration of the primary proton donor to the Schiff base D156 [5]. This band is slightly up shifted by 2 cm^{-1} in D_2O (Fig. 3.9b), which is an unusual response of the carboxylic $C = O$ stretching vibration due to deuteration. The positive band at 1761 cm^{-1}, assigned to the $C = O$ stretch of D156 in the P_1^{500} intermediate [5] and more specifically to a late P_1^{500} state, is downshifted by 4 cm^{-1}. Although the frequency of the $C = O$ stretch of D156 in the dark state is hardly affected in D_2O (*vide infra*), it shows a normal frequency downshift during the lifetime of the P_1^{500} intermediate, indicative of deuteration of the $O - H$ group of the carboxylic group of D156. The assignment of the difference bands [5, 7] and their vibrational isotope effects are compiled in Table 3.1.

Tab. 3.2: Deuterium vibrational isotope effects (VIE) in the carboxylic region of the IR difference spectra of ChR2 [34].

ν in H_2O	ν in D_2O	VIE (Δν)	assignment
1717 cm^{-1}	1708 cm^{-1}	-9 cm^{-1}	(-) E90
1729 cm^{-1}	1724 cm^{-1}	-5 cm^{-1}	(+) E90
1736 cm^{-1}	1738 cm^{-1}	+2 cm^{-1}	(-) D156
1761 cm^{-1}	1756 cm^{-1}	-4 cm^{-1}	(+) D156

The transient absorbance changes at 1736 cm^{-1} and 1738 cm^{-1}, corresponding to the $C = O$ stretch of D156 in ground state ChR2, are plotted in Fig. 3.10 (black trace for experiments in H_2O and red trace in D_2O). The decay and the subsequent recovery in the millisecond time range, which were assigned to deprotonation and reprotonation of D156 [5], exhibit a KIE of 2.7 and 2.4, respectively. These KIEs agree well with those determined for the rise and decay of the P_3^{520} state as derived from time-resolved UV/Vis spectroscopy (see Table 3.2), within the standard deviation of approximately 10-15% of the resulting time constants. This finding is in coherence with our previous assignment of D156 to act as the proton donor to the retinal Schiff base [5]. Furthermore, the fact that a substantial KIE is observed

after H/D exchange strongly suggests that the side chain of D156 is accessible to H/D exchange.

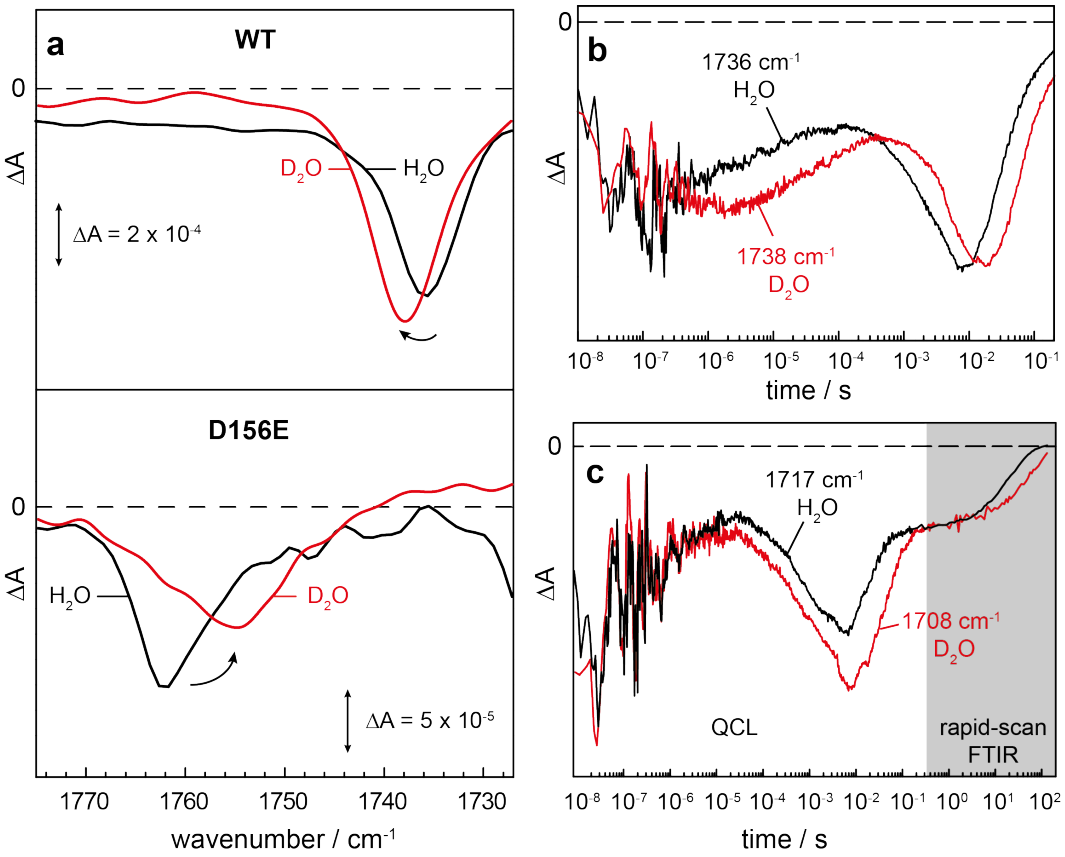

Fig. 3.10: (a) IR difference spectra in the carboxylic region of wild-type ChR2 (top panel) and the D156E variant (bottom panel). For the wild type, spectra at 6 ms in H_2O and at 18 ms in D_2O after the exciting laser pulse were extracted from the QCL data. The spectrum for the D156E variant was recorded under continuous illumination at 450 nm, representing mostly the P_3^{520} state. The negative band was assigned to the $C = O$ stretching vibration of protonated D156 (top panel) and E156 (bottom panel), respectively. Vibrational isotope effect leads to a spectral upshift of 2 cm^{-1} in wild-type ChR2 (top panel). The D156E variant exhibits a vibrational down shift of 8 cm^{-1} in D_2O, typical for H/D exchange (bottom panel). (c) Transient absorption changes of the $C = O$ stretching vibrational band of D156 (proton donor to the retinal Schiff base) probed at 1736 cm^{-1} in H_2O (black) and 1738 cm^{-1} in D_2O (red, dotted). (d) Transient absorption changes of wild-type ChR2 at 1717 cm^{-1} in H_2O (black) and at 1708 cm^{-1} in D_2O (red). These frequencies correspond to the $C = O$ stretching vibration of E90 in water and in deuterium oxide, respectively. Absorbance changes from 300 ms to 90 s were recorded by time-resolved rapid-scan FTIR spectroscopy and merged to the time-resolved QCL data [34].

3.2.4 VIE in the D156E mutant

To further corroborate the exchangeability of the proton of the carboxylic group of D156, the aspartic acid at position 156 was replaced by glutamic acid. This conservative replacement does not impair functionality [5]. Because of the delayed decay of P_3^{520} (reprotonation of E156), it is possible to observe the $C=O$ stretch frequency of E156 by FTIR difference spectroscopy under continuous illumination (Fig. 3.10a, lower). As previously reported [5, 100, 101], the replacement leads to an upshift of the $C=O$ vibration in the dark state from 1736 cm^{-1} (D156) to 1763 cm^{-1} (E156) in H_2O (black traces in Fig. 3.10a). The longer glutamate side chain likely locates the carboxylic group in a conformation less favorable for H-bonding with C128 and, thus, the frequency of the $C=O$ stretch is upshifted. In D_2O, the $C=O$ stretch of E156 exhibits a spectral downshift by 8 cm^{-1}, from 1763 cm^{-1} to 1755 cm^{-1} (bottom panel of Fig. 3.10a) which provides evidence that the carboxylic group at position 156 undergoes H/D exchange. Thus, it is accessible to the externally added D_2O during some steps of the photocycle.

3.2.5 KIE of proton transfer reactions involving E90

E90 is the other carboxylic residue that is protonated in dark-state ChR2 and transiently deprotonated during the ChR2 photocyle. The frequency of the $C=O$ stretch of the carboxylic of E90 is at 1717 cm^{-1} in H_2O which is shifted to 1708 cm^{-1} in D_2O [32, 45, 51]. Despite this significant vibrational isotope effect, the transients at these frequencies (Fig. 3.10c) are very similar from 15 ns to 5 ms (KIE = 1). This experimental observation agrees well with our previous conclusion that the absorption changes at 1717 cm^{-1} in the sub-ms range arise from changes in hydrogen-bonding rather than from deprotonation changes of E90 [5]. This conclusion is also coherent with the wild-type like photocycle kinetics [102] and channel activity of the E90A mutant [31, 102].

At times later than 10 ms, the kinetic of E90 at 1717 cm^{-1} is clearly delayed in D_2O. This time range corresponds to the decay of the P_3^{520} state which is bifurcated to repopulate the initial ground state (75% of the molecules) and to pass the P_4^{480} state (25% of the molecules). Only during the lifetime of the latter, E90 is deprotonated [5], a process that exhibits a KIE of 2.2 (Fig. 3.10c). Reprotonation of E90 takes place in the transition from P_4^{480} to the initial ground state, which occurs in around 10-20 s [5, 51] and shows a KIE of 2.1. Both results indicate a late de- and reprotonation of E90 in the ChR2 photocycle.

3.3 pH indicator experiments

Fig. 3.11 shows the time-dependent absorption changes of the pH indicator bromoxylenol blue (BXB) after blue light excitation of ChR2-wt and the variants E90A (a) and R120H (b). The data for ChR2-wt was taken from Nack et al., 2012 [30]. In comparison to ChR2-wt the E90A shows during the P_3^{520} rise and decay faster proton release and uptake kinetics (factor ≈ 2), fitting with the photocycle kinetics of E90A. The quantification of 0.3 ± 0.1 protons release per activated ChR2 molecule was also identical to ChR2-wt. However, the observed negative plateau region from 100 ms to 10 s in ChR2-wt vanished. This indicates that this proton release and uptake event is caused by E90, which is supported by time-resolved FTIR measurements (see section 3.1.2 and 3.2). The amplitude of this the proton release and uptake during the rise and decay of the P_4^{480} intermediate is around 75% smaller and indicates a lower occupancy of this intermediate state. This was supported by time-resolved FTIR measurements which also show a biphasic recovery kinetic of the initial ground state. Thus, E90 shows a de- and reprotonation event during the P_4^{480} state after channel closure.

The R120H variant was found to be non-conductive. Surprisingly, the UV/Vis kinetics of the intermediate states and the proton release and uptake event is almost identical to ChR2-wt. The stoichiometry is also identical with 0.3 ± 0.1 protons per activated ChR2 molecule. Therefore the mechanistic link between proton transport and channel function may include R120. See section 3.5 for the absorption changes in the IR.

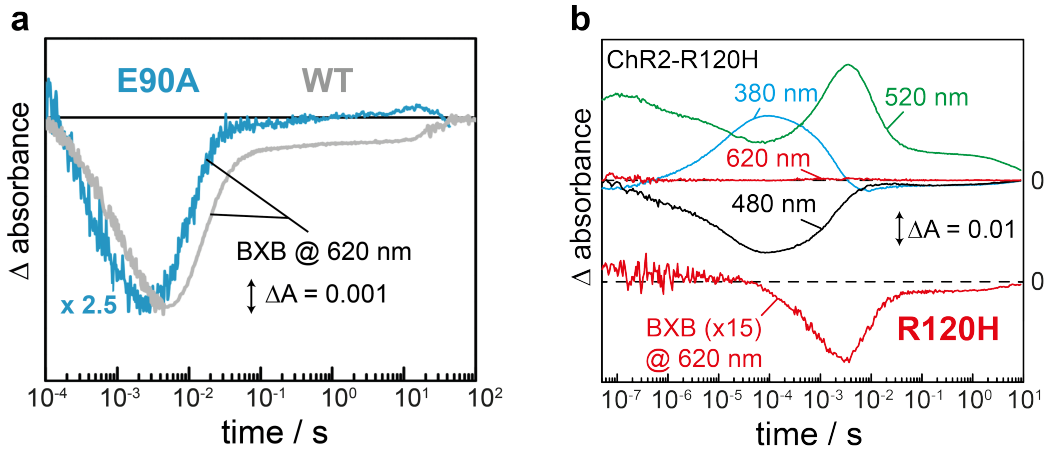

Fig. 3.11: Overview of the time-resolved absorbance changes of bromoxylenol blue (BXB) after photoexcitation of ChR2. (a) Proton release and uptake for ChR2-wt and E90A. (b) Characteristic wavelengths of the ChR2-R120H variant (top) and the proton release and uptake kinetics observed by BXB (bottom). Data for ChR2-wt are taken from [30].

3.4 Pre-gating conformational changes in the E123T variant of ChR2 (ChETA)

I performed time-resolved UV/Vis spectroscopy on the ChR2 variant E123T. The time-resolved absorption changes are presented in Fig. 3.12. The contour plot allows an overall comparison of the absorption changes over time; initiated by a 10 ns laser pulse. Despite shifts in the maximum absorption changes in ChETA, I keep the nomenclature of the intermediate states like in ChR2-wt. The overall comparison shows similarities, but notable differences. Both have an early red-shifted intermediate state (P_1^{500}, $t_{max} < 100$ ns), a blue-shifted intermediate state (P_2^{390}, $t_{max} = 150$ μs in ChR2-wt and $t_{max} = 300$ μs for ChETA), a late red-shifted intermediate state (P_3^{520}, $t_{max} = 3$ ms in ChR2-wt and $t_{max} = 4$ ms for ChETA) followed by slowly ground state-like intermediate (P_4^{480}, $t_{max} \approx 200$ ms). The absorption maxima of the intermediate states shifted in respect to ChR2-wt. As shown in Fig. 3.12 c, the the P_1^{500} state is shifted by 45 nm (510 nm in ChR2-wt and 555 nm in ChETA), the P_2^{390} state is hardly shifted and the P_3^{520} state is shifted by 15 nm (520 nm in ChR2-wt and 535 nm in ChETA). The ground state absorption is also red shifted by 25 nm (450 nm in ChR2-wt and 475 nm in ChETA), (Fig. 3.12 c). Although the time point of maximal accumulation of the intermediate states are similar in ChR2-wt and ChETA, the rise and decay time-constants differ. Fig. 3.12 d-e, represents the rise and decay of the P_2^{390} intermediate state and the decay of the P_1^{500} and the rise and decay of the P_3^{520} intermediate states, respectively. The decay kinetic of the P_1^{500} state is delayed, which leads to a delayed rise kinetic of the P_2^{390} state (Fig. 3.12 d. The decay of the P_2^{390} and the rise and decay of the P_3^{520} state is very similar to ChR2-wt. But in ChR2-wt the decay of the P_3^{520} state shows a pronounced P_4^{480} state with a slow decay component. The observed time constant of the ground state recovery (P_4^{500} decay) is: $\tau = 2$ s in ChETA and $\tau = 12$ s in ChR2-wt.

In addition to the UV/Vis experiments Víctor Lórenz-Fonfría performed the time-resolved ns-step-scan FTIR measurements and performed maximum entropy method (MEM) and Fourier self deconvolution (FSD). In Fig. 3.13a the ethylenic bands from the photoproducts of the all-*trans* and 13-*cis* photocycles are presented. The negative band at ≈1554 cm^{-1} was assigned to the ethylenic vibration of the dark-state retinal and shows an expected ultrafast rise ((Fig. 3.13c). This band also shifts during the photocycle from 1555.5 to 1552 cm^{-1} (Fig. 3.13d), infer a spectral overlap of at least two bands. By MEM, a maximum at ≈1552 cm^{-1} is accompanied by a minor band at ≈1558 cm^{-1}, assigned as ethylenic vibration of all-*trans* and 13-*cis* retinal in the dark state, respectively.

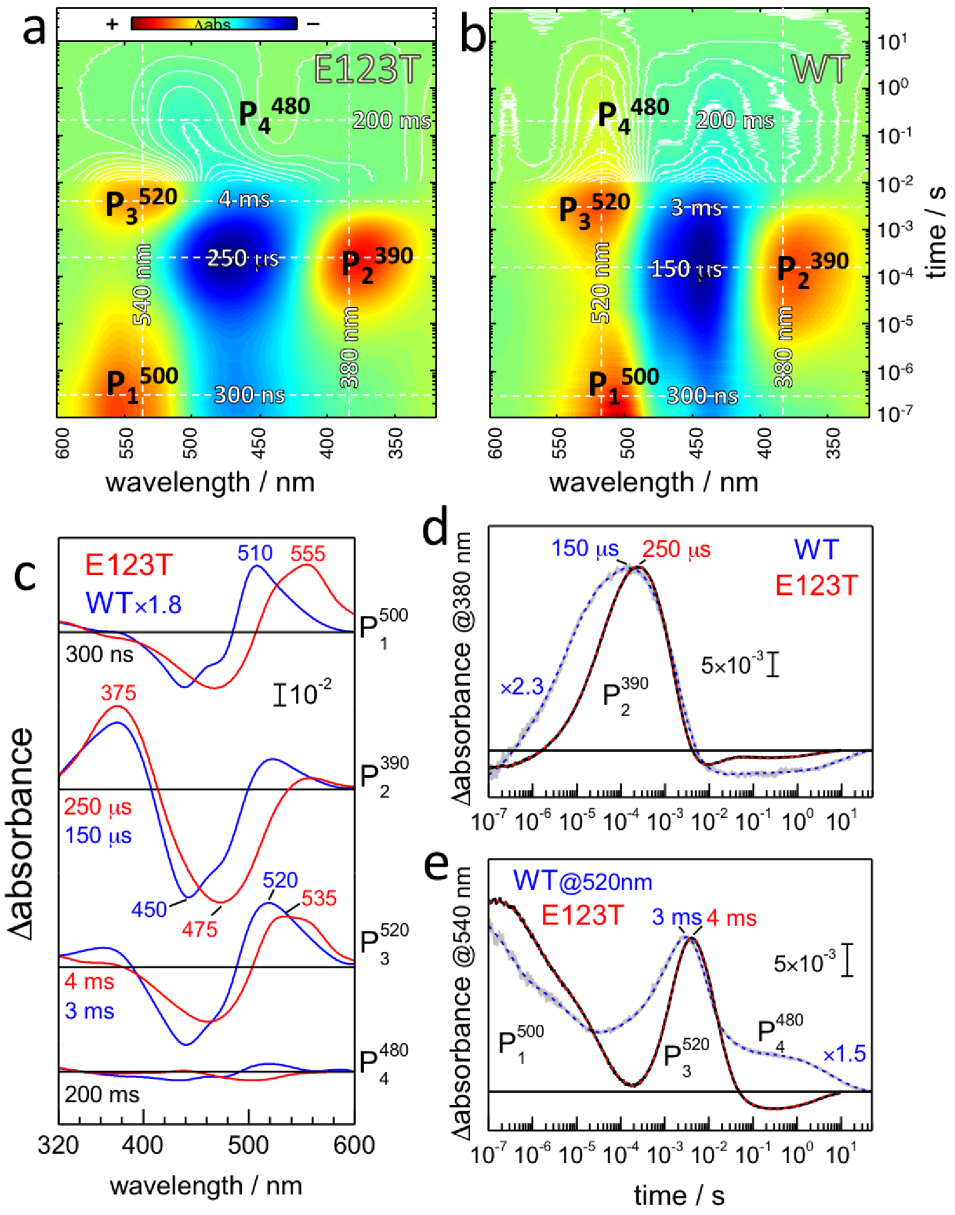

Fig. 3.12: Light-induced absorption changes of ChR2-E123T and ChR2-wt in the UV/Vis range. (a-b) Contour plots of the absorption changes between 320 nm and 600 nm. Positive and negative absorption changes are colored in red and blue, respectively. Intermediate states are highlighted in respect to their maximum absorption wavelength and the corresponding time points. The horizontal and vertical dashed lines indicates spectral slices or kinetics, presented in c and d-e, respectively. (c) Absorption difference spectra of ChR2-wt (blue) and E123T (red), representing the P_1^{500}, P_2^{390}, P_3^{520} and P_4^{480} state. (d-e) Transient absorption changes of ChR2-wt (blue) and and E123T (red) at 380 nm and 520 or 540 nm as indicated. The fit is indicated by dashed lines [52].

Only the component at 1552 cm^{-1} was resolved above 1 ms (Fig. 3.13a). Therfore, the photocycle from the 13-*cis* photocycle exhibits a dark-state recovery with a half-life below 1 ms. The early broad positive band at ≈1529 cm^{-1} shows three components at ≈1540, 1528, and 1514 cm^{-1}, resolved after band narrowing by both FSD and MEM (Fig. 3.13a). From these three putative ethylenic bands, the maximum value for retinal absorption in the visible is concluded at ≈520, ≈560, and ≈620 nm [84], which is in coherence with the broad positive band centered at 555 nm in the UV/Vis difference spectra in the nanosecond range (Fig. 3.13b). The absorption changes at 1541 and 1514 cm^{-1} rises before 60 ns, but the kinetic at 1528 cm^{-1} rises slightly later (Fig. 3.13e). For further information see Lórenz-Fonfría et al. 2015 [52].

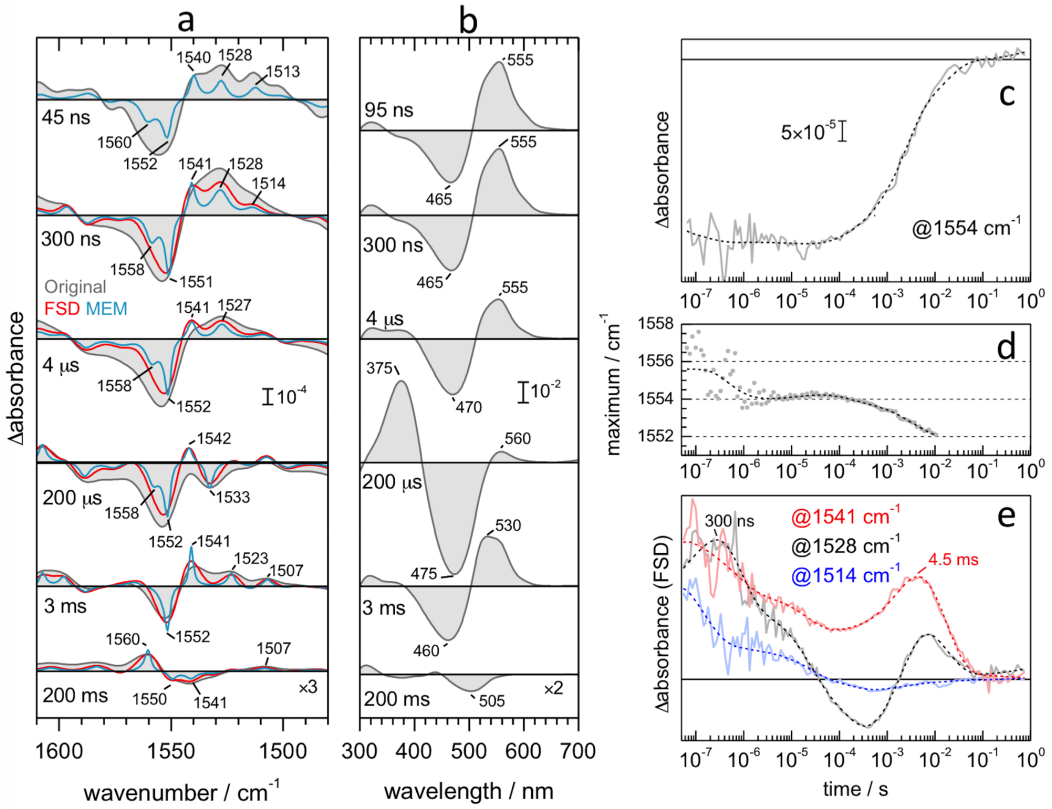

Fig. 3.13: Analysis of the retinal ethylenic region of ChR2-E123T by Víctor Lórenz-Fonfría. (a) FTIR difference spectra of ChR2-E123T at selected times (gray) and processed by two band-narrowing methods: FSD (red) and MEM (light blue). (b) UV/Vis difference spectra at equivalent times. (c) Transient absorption changes of the retinal ethylenic vibration of the dark state at 1554 cm^{-1}. (d) Maximum of the retinal ethylenic band of the dark state as a function of time (gray dots). Values above 10 ms are omitted due to the low intensity of the band. (e) Transient absorption changes at 1541 cm^{-1} (red trace), 1528 cm^{-1} (black trace), and 1514 cm^{-1} (blue trace), monitored by the FSD spectra. In parts c-e, the dashed traces correspond to a global exponential fitting [52].

3.5 Loss-of-function variants of ChR2

Time-resolved QCL spectroscopy on ChR2-wt and the non-channeling variant ChR2-R120H was performed. Although, we found that the D253N variant exhibits also strongly reduced photocurrents and only small differences in the absorption kinetics in the visible [5], but the expression and effects on the proton transfer reaction might be more challenging to interpret, and therefore we focus on the R120H mutant. The time-resolved vis-pump IR-probe spectroscopy was performed for ChR2-wt and R120H in collaboration with AG Wachtveitl (MPI, Frankfurt). Electrophysiology measurements were performed by Christian Bamann (AG Bamberg, Frankfurt). I fused the data sets together and analyzed them. All measurements were done in D_2O since high absorption of water bands overlap with the amide I bands. Therefore, it is challenging to obtain time traces with a sufficient signal-to-noise ratio in H_2O by vis-pump IR-probe spectroscopy.

3.5.1 Time-resolved IR spectroscopy on ChR2-wt

Previous results on time-resolved IR spectroscopy gave an insight into protonation dynamics [5], structural changes [58] and represent the first events after photoexcitation [32, 59]. Time dependent absorption changes were recorded from 0.4 ps to 1 s in the spectral range from 1566 cm^{-1} to 1684 cm^{-1}, see Fig. 3.14a. Individual kinetics (dotted lines) are extracted and presented in Fig. 3.14b. This is, to our knowledge, the first time that a combined IR data set of a protein sample covers 12 magnitudes in time. The calculated decay associated difference spectra are shown in Fig. 3.14C. For a detailed discussion of the vis-pump and IR-probe data from fs to ns see Neumann-Verhoefen et al., 2013 [32]. IR data in the time range between 6 μs and 1 s of ChR2-wt were discussed in section 3.1.

3.5.2 The loss-of-function variant: R120H

The variant R120H of ChR2 is characterized by electrophysiology (Fig. 3.15) and time-resolved UV/Vis spectroscopy (Fig. 3.16). The time-resolved photocurrents are measured by Christian Bamann (AG Bamberg, MPI Frankfurt). Based on the non-functional variant R159A of the C1C2 chimera (described by Kato et al. [31]) a non-channeling variant R120H in ChR2 was synthesized. As shown in Fig. 3.15, the electrophysiology measurements in HEK cells under continuous blue light excitation show strongly reduced photocurrents (0.01 nA) in comparison to ChR2-wt (300-500 nA).

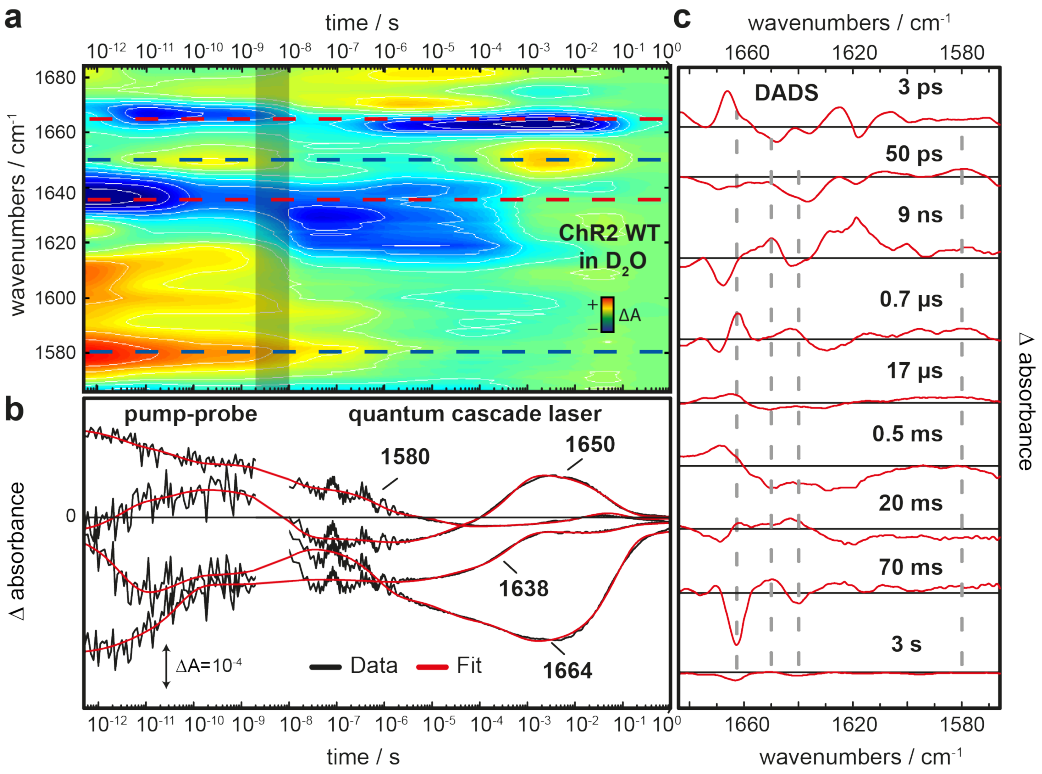

Fig. 3.14: Channelrhodopsin-2 in D_2O measured by Vis-pump-IR-probe spectroscopy and tunable QCL. (a) Contour plot of the combined and fitted data set of ChR2-wt in D_2O. Positive and negative absorption changes are colored in red and blue, respectively. Characteristic wavenumbers are marked by dashed lines. The grey area indicates interpolated data. (b) Transient absorption changes ranging from 0.5 ps to 1 s at specific wavenumbers: 1580 cm^{-1}, 1630 cm^{-1}, 1650 cm^{-1} and 1664 cm^{-1}. Raw data and multiexponential fits are shown in black and red, respectively. (c) Decay associated difference spectra (DADS) at the 9 time constants after global fit analysis. The fs pump-probe data set was taken from [32].

We further investigated the ChR2-R120H mutant with time-resolved spectroscopy. Although the photocurrents are strongly reduced, the transient visible absorption changes in H_2O are hardly effected (see Fig. 3.16). The kinetics at 520 nm, 380 nm and 440 nm are colored in red, blue and black, respectively for the variant and in grey for ChR2-wt. The transient absorption changes at these wavelengths represent the intermediate states P_1^{500}, P_2^{390}, P_3^{520}, P_4^{480} and the ground state depletion. Intermediate states of the ChR2 photocycle are characterized by the absorption maxima in the visible, caused by the retinal absorption. These shifts in the absorption maxima are related to structural changes as well as proton transfer reaction of the retinal Schiff base. The kinetics of ChR2-wt and variant are almost identical although the P_2^{390} decay and the P_3^{520} rise are slightly accelerated. The contour plots of ChR2-wt (Fig. 3.16c) and ChR2-R120H (Fig. 3.16d) show that the red shifted intermediate

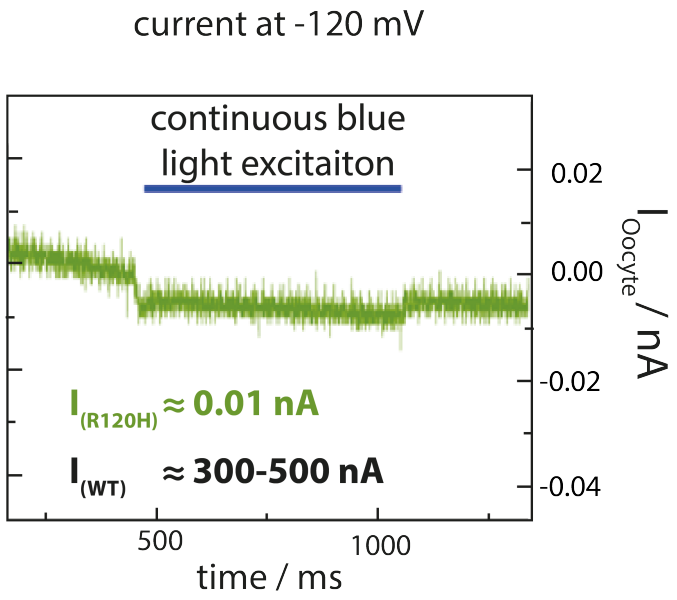

Fig. 3.15: Electrophysiological measurements of ChR2-R120H and compared to ChR2-wt. Electrophysiology measurements were performed by Christian Bamann (AG Bamberg, Frankfurt).

states P_1^{500} and P_3^{520} are spectrally upshifted by 10 nm. The decay associated difference spectra (DADS) are presented in Fig. 3.16b. The time constants of the global exponential fit are similar to the previously published data for ChR2-wt [5, 34]. This means, that the protonation reactions at the SB are hardly affected, although the channel is non-functional. A link between proton transfer reactions and pore formation is still missing.

3.5.3 Time-resolved IR spectroscopy on ChR2-R120H

Time-resolved absorption measurements in the visible are well established to identify the intermediate states of ChR2 related to the electronic state of the retinal cofactor, but structural changes of the protein are spectrally silent. Vibrational spectroscopy in the IR range detects structural changes as well as protonation dynamics. Here, we analyze the described non-functional variant R120H in the IR range by vis-pump and IR-probe as well as time-resolved tunable QCL spectroscopy. An overview of the time-resolved difference spectra is shown in Fig. 3.17. The contour plot of the global fit covers the spectral range from 1568 cm^{-1} to 1684 cm^{-1} and the time range from 0.4 ps to 1 s. Positive and negative absorption changes are colored in red and blue, respectively. The grey bar between 1.8 ns and 10 ns indicates the interpolated data points. Dashed lines indicate the most important marker band; Their kinetics are extracted and shown in Fig. 3.17b as for ChR2-wt (Fig. 3.14b). The raw data and the global fit are shown in black and red, respectively.

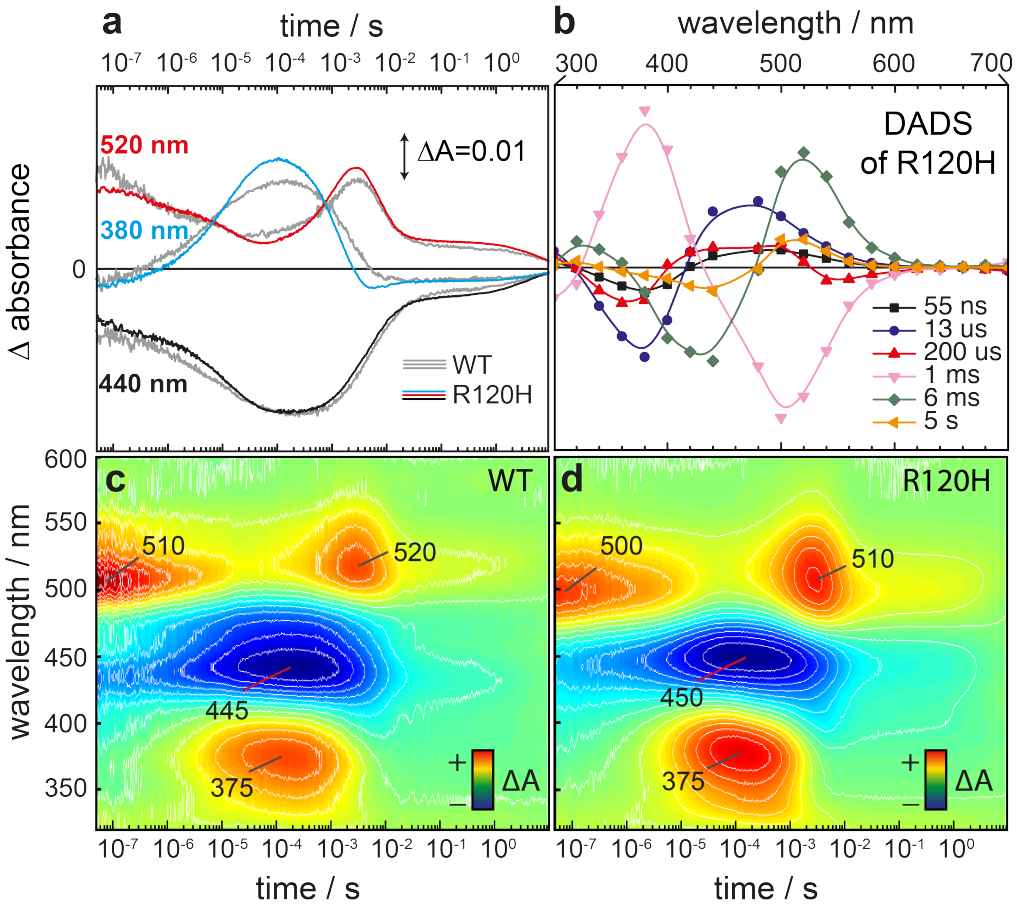

Fig. 3.16: Characterization of the R120H mutant by UV/Vis spectroscopy and electrophysiology measurements. (a) Kinetics at 380 nm, 440 nm and 520 nm are colored for R120H in red, black and blue, respectively and in grey for ChR2-wt. The time range from 50 ns to 9 s in covered. (b) Decay associated difference spectra (DADS) of R120H at time constants obtained by global fitting analysis. (c-d) Contour plots of the transient absorption changes of ChR2-wt (c) and R120H (d). Positive and negative absorption changes are colored in red and blue, respectively. Absorption peaks are marked by their wavelength.

The kinetics are similar to the WT sample, but the positive contribution at 1580 cm^{-1} is missing in the period up to 1 ns. Therefore, this band in the WT data (Fig. 3.14) is either caused directly by the replaced arginine, or it is indirectly affected by the variant R120H. Global exponential fit and SVD analysis were performed. The DADS and their specific time constants are shown in Fig. 3.17c in red for R120H and in grey for WT. The time constants are very similar, but there are some differences in the DADS. The positive band at 1580 cm^{-1} is missing in the pico second time range. In addition the broad negative band at 1625 cm^{-1} vanishes at 0.7 ms in comparison to the WT. In section 3.5.4 we analyzed further the vibrational mode of R120.

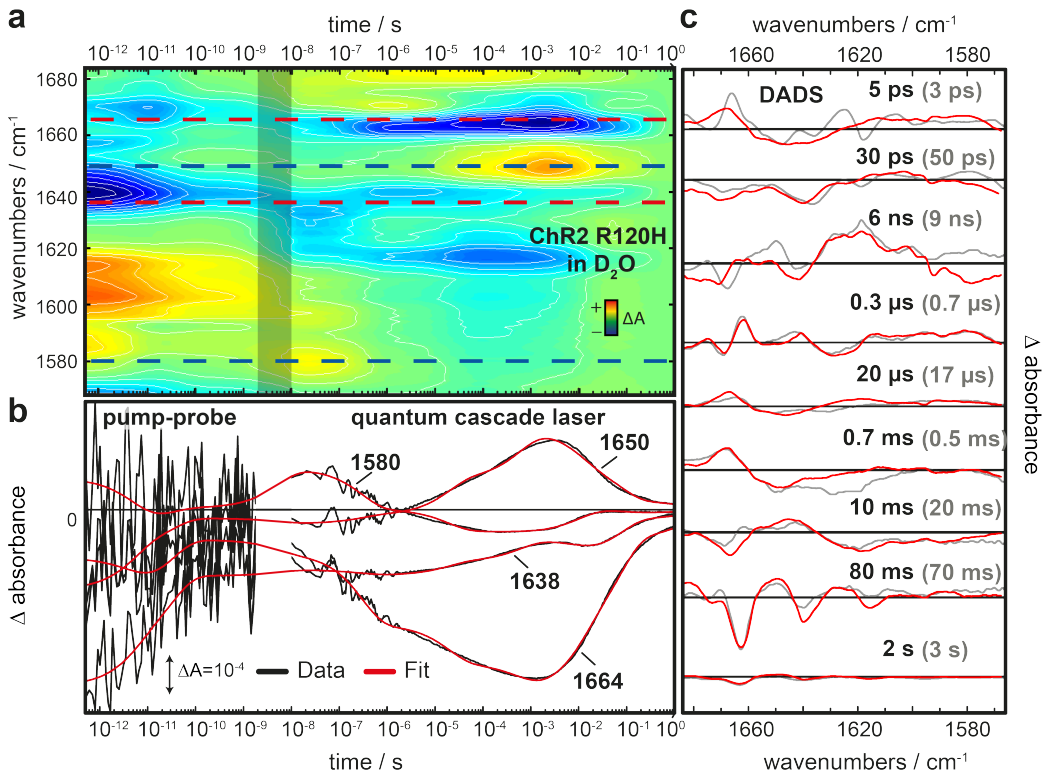

Fig. 3.17: ChR2-R120H in D_2O measured by Vis-pump-IR-probe spectroscopy and tunable QCL. (a) Contour plot of the combined and fitted data set of ChR2-R120H in D_2O. Positive and negative absorption changes are colored in red and blue, respectively. Characteristic wavenumbers are marked by dashed lines. The grey area indicates interpolated data. (b) Transient absorption changes ranging from 0.5 ps to 1 s at specific wavenumbers: 1580 cm^{-1}, 1630 cm^{-1}, 1650 cm^{-1} and 1664 cm^{-1}. Raw data and multiexponential fits are shown in black and red, respectively. (c) Decay associated difference spectra (DADS) at the 9 time constants after global fit analysis. ChR2-R120H and WT data are colored in red and grey, respectively.

3.5.4 Arginine vibrations

The identification of arginine modes in a protein environment is difficult, because they have a low extinction coefficient and strongly overlap with vibrations from the backbone and retinal. IR spectra of model compounds like guanidine hydrochloride (GdmCl) can address vibrational modes of arginine side chains. GdmCl was solved in D_2O and H_2O and measured with an ATR setup. A pure solvent spectrum of D_2O and H_2O with the appropriate salt concentration was subtracted. As presented in Fig. 3.18 (black), the protonated guanidine group at pD 8 is showing a maximum vibrational band at a frequency of 1603/1593 cm^{-1} (second derivative analysis revealed two maxima) representing the nearly degenerate asymmetric stretching mode of the CN_3 group coupled to the ND_2 scissor mode [103]. Two smaller peaks

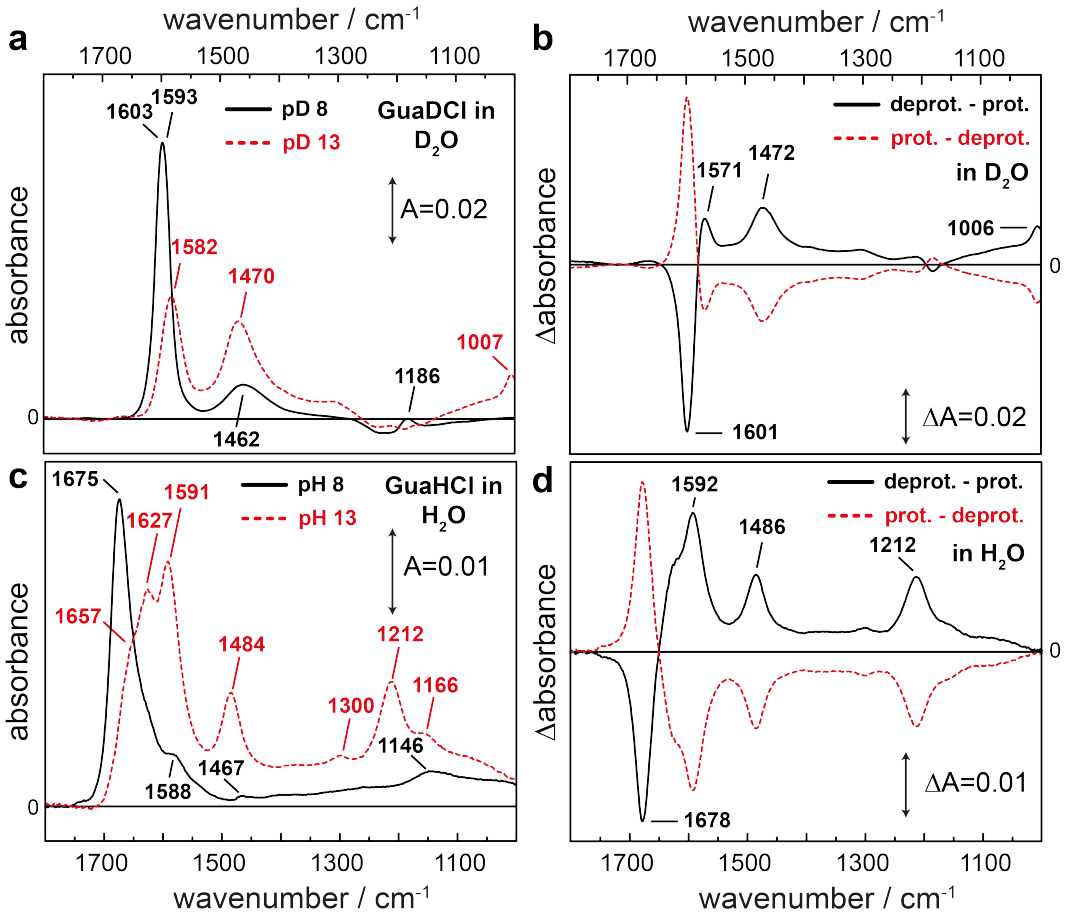

Fig. 3.18: Spectroscopic analysis of a guanidine group in the IR range. IR spectra (a) and IR difference spectra (b) of guanidine hydrochloride in D_2O at pD 8 and pD 13 colored in black and red, respectively. (c-d) shows the same, except that the guanidine hydrochloride was solved in H_2O instead of D_2O.

are observed at 1462 cm^{-1} and 1186 cm^{-1}, the later is caused by the symmetric stretching vibration of the CN_3 group [103]. Upon deprotonation (pD 13) theses peaks shifts to 1582 cm^{-1}, 1470 cm^{-1} and 1007 cm^{-1} (Fig. 3.18, red dotted line). The intensity of the band at 1582 cm^{-1} is reduced, though the intensity of the peaks at 1470 cm^{-1} and 1007 cm^{-1} are increased. The vibrational modes between 1460 cm^{-1} and 1490 cm^{-1} are observed in D_2O (Fig. 3.18a-b) as well as in H_2O (Fig. 3.18c-d), but with higher intensity upon deprotonation of the guanidine group. Therefore this band can be assigned as the asymmetric stretching vibration of the guanidine group that is decoupled from the $N-H$ or $N-D$ scissor modes, as suggested by Braiman et al. [104].

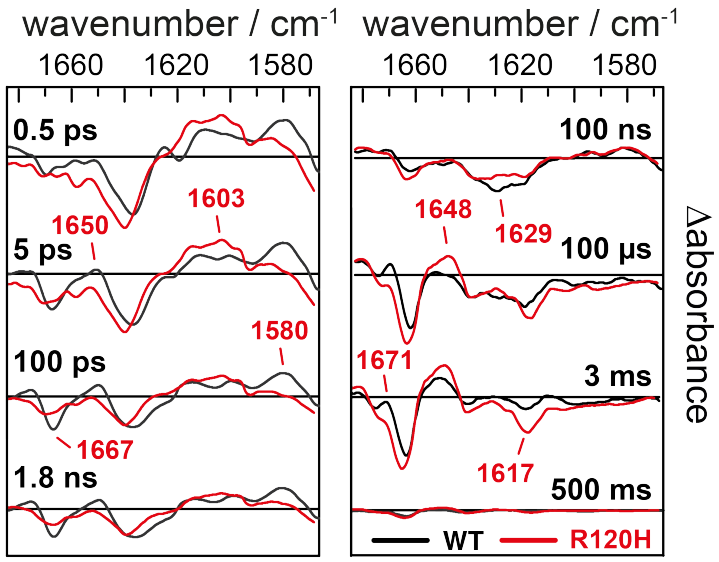

Fig. 3.19: IR difference spectra of ChR2-wt (black) and ChR2-R120H (red) at specific time points. The differences between wild type and mutant are highlighted by red colored wavenumbers. The time points of these spectra are shown in black.

The difference absorption spectrum between protonated and deprotonated state for GdmCl is shown in Fig. 3.18B. The largest peak can be observed at 1601 cm^{-1} and two smaller peaks at 1571 cm^{-1} and 1472 cm^{-1}. These reference spectra are compared with our results from ChR2-wt and the R120H variant (Fig. 3.19). But one has to keep in mind, that vibrational modes of GdmCl and bound Arg may show differences caused by the environment and the 3-carbon aliphatic chain. The difference spectra at eight different time points are presented in Fig. 3.19. In the left column, the spectra at 0.5 ps, 5 ps, 100 ps and 1.8 ns are shown, representing the early photoproducts. The right column represents the maximum accumulation of the intermediate states named P_1^{500}, P_2^{390}, P_3^{520} and P_4^{480} at 100 ns, 100 μs, 3 ms and 500 ms, respectively. The differences between ChR2-wt (black) and ChR2-R120H variant (red) are marked by their particular wavenumber (colored in red). Here, the band at around 1580 cm^{-1} is missing in the R120H variant from 10 ps till 1 ns. A small negative peak appears in the spectra at 0.5 ps and 5 ps at 1658 cm^{-1}. The amide I band formation is reduced in the variant during P_1^{500} formation although the amplitude during the pore formation (P_2^{390} and P_3^{520} state) is not affected. During pore formation only a small band at 1630 cm^{-1} is missing.

3.6 Temporal evolution of helix hydration

3.6.1 Correlation between photocurrents and absorption changes in ChR2

In a time-resolved patch-clamp electrophysiology experiment light-induced currents (photocurrents) of ChR2 expressed in human embryonic kidney (HEK) cells are recorded. The time-resolved photocurrents were measured by Christian Bamann (AG Bamberg, MPI Frankfurt). The photocurrents are proportional to the ion conductance of the ion channel and the amplitude of the photocurrent is voltage dependent, see Fig. 3.20 a. The rise and decay of the photocurrent reflects the on-gating and off-gating, respectively. The time point of maximum ion conductance (Fig. 3.20 a, green open circles) is voltage insensitive; $t_{max} = 1.2 \pm 0.1\ ms$ from -100 mV to +80 mV. This paramter is compared with our spectroscopic results from time-resolved UV/Vis and IR spectroscopy (Fig. 3.20 b-e). The absobance changes are shown as contour plots within the time range of 6 μs to 1 s.

In the UV/Vis range (Fig. 3.20b) ChR2 shows two intermediate states (P_2^{390} and P_3^{520}), which reach a maximum accumulation at 150 μs and 3 ms, respectively. Therefore, the ion conducting state is not associated with a specific protonation state of the retinal Schiff base. This is further supported by analysis of the ethylenic stretching vibration ($C = C$), see Fig. 3.20 e. In other ion channels, it was found that protonation of internal amino acid side changes are involved in the gating mechanism [105]. We already identified several protonation events in ChR2, involving E90, D156, and D253, as described in section 3.1. But the photocurrents and the absorption changes of protonated carboxylic acids do not correlate (Fig. 3.20 c).

To illustrate the correlation of all vibrational modes, the correlation coefficient was determined for each frequency to match with the photocurrent (Fig. 3.20 f). High and low correlation is colored in red and blue respectively. Interestingly, only two vibrational modes in the amide I region between 1600 cm^{-1} and 1700 cm^{-1} correlate with the observed photocurrents. The bands at (-) 1664 cm^{-1} and (+) 1648 cm^{-1} are mostly related to the $C = O$ stretching vibration of the protein backbone amide carbonyl vibration. The frequency depends on the interhelical and external hydrogend bonds. The transients show a maximum accumulation at 0.8 ms and 1.0 ms for 1664 cm^{-1} and 1648 cm^{-1}, respectively. This is in agreement with the observed maximum accumulation of the photocurrents. We conclude that changes in α-helices tallies with ion conductance. The comparison of $H_2\ ^{16}O$ and $H_2\ ^{18}O$

measurements reveal that the observed frequency shift origins from helix hydration, see Lórenz-Fonfría et al. 2015 [52]. A detailed analysis by lifetime distribution was performed to identify the on- and off gating events by helix hydration. The photocurrents rises in two steps: $\tau = 225\ \mu s$ (ON1) and $\tau = 2.2\ ms$ (ON2). The photocurrents also decay with two steps: $\tau = 9.3\ ms$ (OFF1) and $\tau = 44\ ms$ (OFF2). lifetime distribution of the amide I bands mostly agrees with the time constants observed for the photocurrents. For further information see Lórenz-Fonfría et al. 2015 [52].

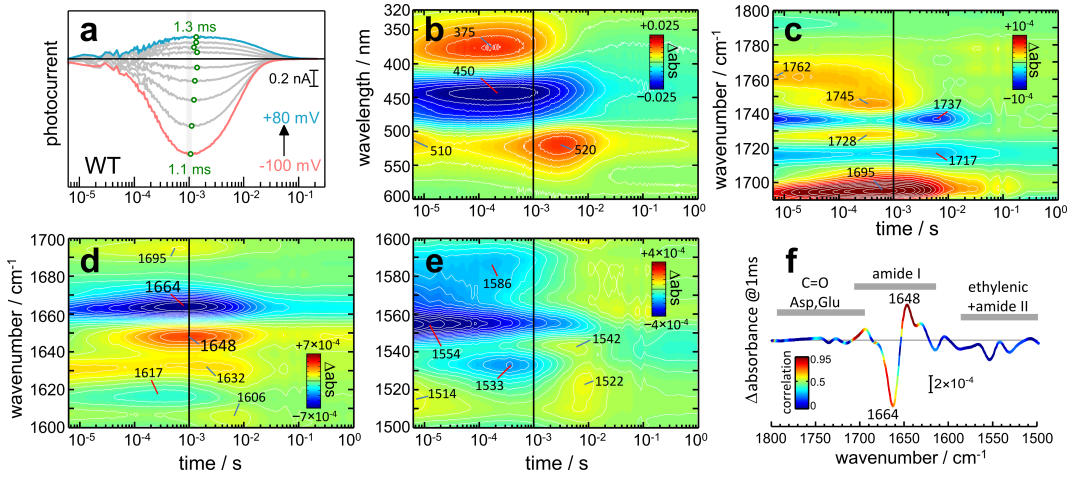

Fig. 3.20: Comparison of time-resolved absorption changes and currents of ChR2. (a) Time-resolved photocurrents at different voltages from -100 mV to +80 mV. The maximum ion flow is indicated by green open circles. ChR2 was expressed in HEK cells and measured by whole cell electrophysiology. (b-e) Contour plot of transient absorption changes in the UV/Vis and IR range. Positive and negative absorption changes are colored in red and blue, respectively. Characteristic wavelength and wavenumbers highlighted. The solid black line indicates $t_{max} = 1\ ms$ of the photocurrents. (f) Infrared difference spectrum at $1ms$. The color represents the correlation coefficient between photocurrents at -40 mV and the transient absorption changes in the IR region. High and low correlation is colored red and blue. Lifetime distribution was performed by V. Lórenz-Fonfría and electrophysiology measurements were performed by C. Bamann [58].

3.6.2 Slow (D156E) and fast (E123T) functional variants of ChR2

The observed correlation between helix hydration and photocurrents must be verified by slow and fast channeling variants of ChR2 because the electrophysiology measurements were performed in HEK cells (lipid environment) and the time-resolved IR data was obtained for ChR2 solubilized in detergent. It was found that D156E show delayed photocurrents [5] and E123T shows accelerated photocurrents [10].

In Fig. 3.21 we present the measured photocurrents and the amide I absorption changes of the ChR2 variant E123T (a-b) and D156 (c-d). E123T shows a maximum accumulation of ion conductance at around 550 μs (450 μs at 25 řC). The amide bands reach a maximum at 350 μs (1665 cm^{-1}) and 500 μs (1648 cm^{-1}) and agree with the two times faster photocurrents. D156E shows a maximum accumulation of ion conductance between 5 ms to 12 ms, depending on the applied patch clamp voltage. The amide bands reach a maximum at 5 ms (1663 cm^{-1}) and 12 ms (1650 cm^{-1}), which is still in agreement with the 5-12 times faster photocurrents.

The lifetime distribution of E123T shows an on- and off-gating time constant: $\tau =$ 180 μs (ON1) and $\tau = 5.0$ ms (OFF1), which is suitable to the time constants for the amide I vibrations: $\tau \approx 170$ μs and $\tau \approx 3.4$ ms (Fig. 3.21e, upper panel). The lifetime distribution of D156E shows an on- and off-gating time constant: $\tau = 1.5$ μs (ON1) and $\tau = 75$ ms (OFF1), which is consistent to the time constants for the amide I vibrations: $\tau \approx 1.9$ ms and $\tau \approx 55$ ms (Fig. 3.21 e, lower panel). Overall, the fast and slower variants show accelerated and delayed helix hydration steps, correlating with the observed photocurrents.

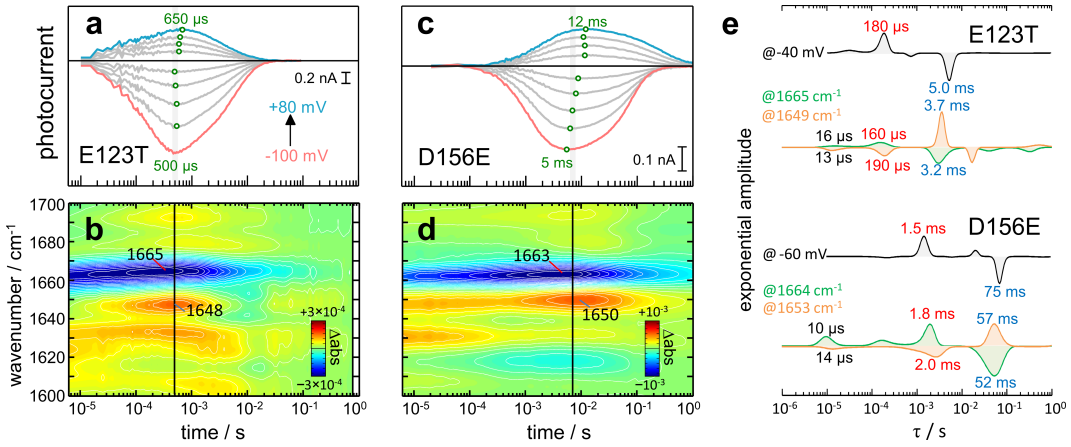

Fig. 3.21: Comparison of time-resolved absorption changes in the amide I region of the fast channeling variant ChR2-E123T and the slow channeling variant ChR2-D156E. Time-resolved photocurrents of (a) E123T and (c) D156E. Transient absorption changes in the IR region (1600-1700 cm^{-1}) of (b) E123T and (d) D156E. The black line indicates t_{max} of the photocurrents. (e) Comparison of the lifetime distribution of the amide I changes and the photocurrents. Lifetime distribution was performed by V. Lórenz-Fonfría and electrophysiology measurements were performed by C. Bamann [58].

3.7 ChR2 at various pressures

3.7.1 ChR2 in detergent

After blue light excitation ChR2 undergoes a photocycle with different intermediate states resulting in different absorption maxima. Transient absorbance changes of ChR2 solubilized in detergent were measured at five different pressures and at three different wavelengths (Fig. 3.23). The data at 380 nm reflect rise and decay of the P_2^{390} intermediate (a-b), while the data at 520 nm corresponds mostly to the rise and decay of the P_1^{500} and P_3^{520} intermediate states (c-d). To the data at 480 nm, not shown, contribute basically all the intermediates, being of more complex interpretation. It is evident, that the amplitude of the P_2^{390} state exhibits a non-linear pressure dependency. The highest amplitude is observed at 1 bar, which is reduced by a factor of 1.5 to 1.9 at 100 to 400 bar, respectively. Upon applying a pressure of 800 bar, the intensity is reduced by a factor of 7.5. The traces were normalized to yield the same maximum transient absorption difference (Fig. 3.23b) to facilitate the comparison of the kinetics. This reduction in amplitude was fully reversible while decreasing the pressure back to 1 bar, discarding protein denaturation as its source. The absorption spectrum was also unaffected by pressure (Fig. 3.22), discarding that the reduced amplitudes could be caused by pressure-induced a spectral shift of the chromophore absorption maximum.

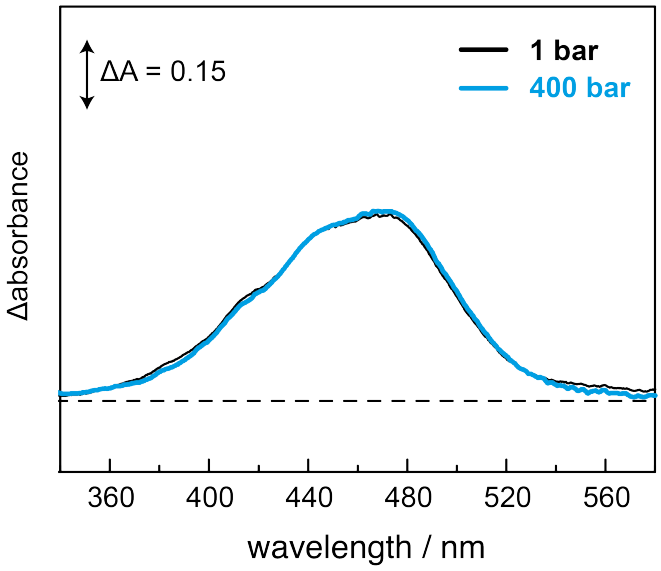

Fig. 3.22: UV/Vis absorption spectrum of detergent-solubilized ChR2 ground state at 1 bar (black) and 400 bar (blue). This spectrum was measured with a portable UV/Vis spectrometer.

The decay of the P_2^{390} state is accelerated under pressure, an observation that fits with other indications [5, 58], that support the occurrence of important conformational changes between an early and a late P_2^{390} intermediates (referred as P_{2a}^{390} and P_{2b}^{390}, respectively). The decay of the P_{2b}^{390}state is accelerated under pressure and an early P_{2a}^{390} intermediate is observed. These kinetic effects are analyzed by global fitting (table 3.3) and lifetime distribution analysis (not shown). The P_1^{500} and P_3^{520} states show also a reduced accumulation under high pressure but with slightly different factors (Fig. 3.23c-d). It seems, that pressure reduces the quantum yield of photoisomerization, but kinetic factors on the photocycle contribute to a lower extend to modulate the final accumulation of each intermediate. By scaling to the maximum amplitude of the P_3^{520} state it becomes evident that the rise of this intermediate is accelerated (in coherence with the faster decay of the P_{2b}^{390}state) while its decay is decelerated. Interestingly, the decay of the P_3^{520} state has been shown to correlate with the cessation of the photocurrents [5], but also with the dewetting of transmembrane regions as the conductive transmembrane pore collapses [58]. The delayed decay of P_3^{520} indicates, that this process involves an activation state of increased volume. Although the lifetime distribution analysis shows hardly any acceleration of the rise of the P_3^{520} state, the time constants provided by global exponential fitting do show a linear acceleration under pressure (Fig. 3.23). This small discrepancy can be explained by the fact that the lifetime distribution analysis uses information of a single time trace, while global exponential fitting uses data from multiple time traces.

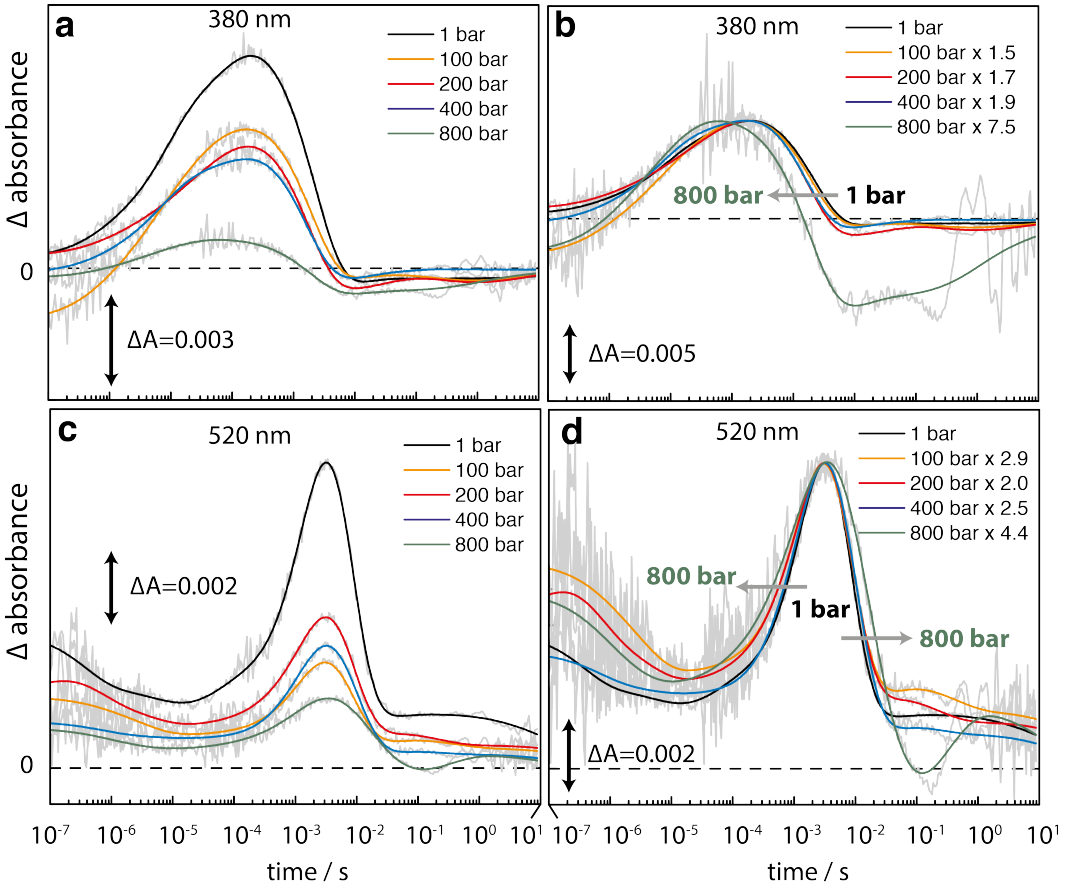

Fig. 3.23: Transient absorbance changes and lifetime distributions of ChR2 solubilized in detergent at various pressure values. The raw data is shown in grey and the fits are colored according to the applied pressure as indicated from 1 bar (black) to 800 bar (green). The raw and scaled absorption changes at 380 nm are shown in (a) and (b), respectively. The raw and scaled absorption changes at 520 nm are shown in (c) and (d), respectively.

3.7.2 ChR2 reconstituted in phospholipids

ChR2 was reconstituted into small unilamellar liposomes made of the lipid POPC. The resulting proteoliposomes scatter visible light, in particular at lower wavelengths. Therefore, for determination of the time-constants and their pressure sensitivity by exponential fitting, time traces of sufficient signal-to-noise ratio were only achieved at 480 nm and 520 nm. As found for the detergent solubilized sample, the decay of the P_3^{520} state is decelerated by increasing the pressure (Fig. 3.24).

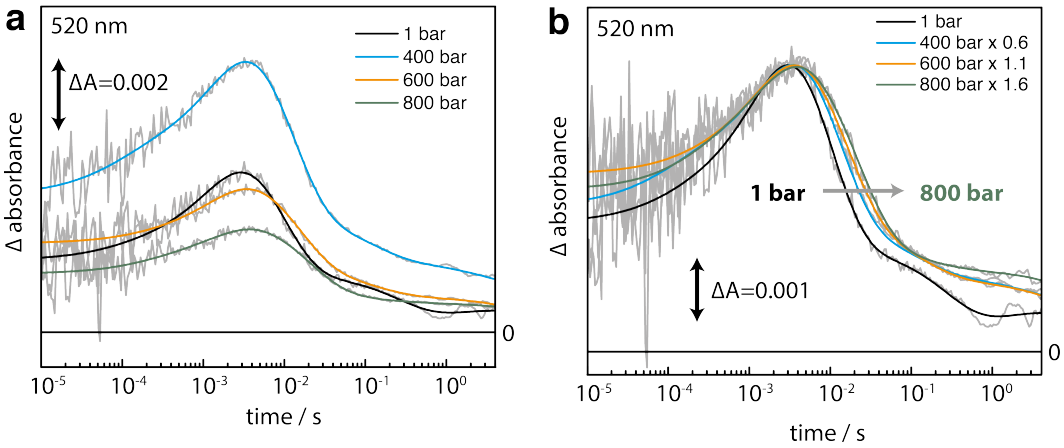

Fig. 3.24: Transient absorbance changes and lifetime distributions of ChR2 reconstituted into liposomes at various pressure values. The raw data is shown in grey and the fits are colored according to the applied pressure as indicated from 1 bar (black) to 800 bar (green). The raw and scaled absorption changes at 520 nm are shown in (a) and (b), respectively. Absorption changes at 380 nm are not measured due to light scattering.

3.7.3 ChR2 embedded in lipidic nanodiscs

In contrast to the lipid reconstitution, a new reconstitution technique named nanodiscs can be used to prevent large aggregation and therefore reduce scattering, providing time-traces of higher quality. Nanodiscs exploits phospholipid bilayers, of DMPC in our case, encircled by a stabilizing amphipathic helical membrane scaffold protein [106]. The nanodiscs were sufficiently large in diameter to encompass a dimer of ChR2. As compared to lipid vesicles, nanodiscs represent a well-controlled membrane system of a size that does not scatter visible light. Moreover, protein aggregation is prevented.

The kinetics and their pressure dependency are very similar (Fig. 3.25) to those observed for detergent solubilized ChR2 (Fig. 3.23), while differing substantially stronger for those obtained with proteoliposomes (Fig. 3.24). The kinetics observed during the transition from the P_1^{500} to the P_2^{390} state are delayed by higher pressure (see table 3.3). The decay of the P_2^{390} state is accelerated and amplitudes of the $P_{2a}^{390}$and P_{2b}^{390}state are affected. At 1 bar the P_{2a}^{390}state only appears as a small shoulder during the P_{2b}^{390}state formation. In contrast, at 800 bar all amplitudes are decreased, but the ratio of these two states is almost inverted, indicating an influence of the concentration of these states by pressure and therefore activation volume changes. Under high pressure the P_3^{520} state decay is decelerated as if in detergent. The accumulation of all intermediates, and in particular of P_2^{390} and P_3^{520}, is also decreased upon pressure.

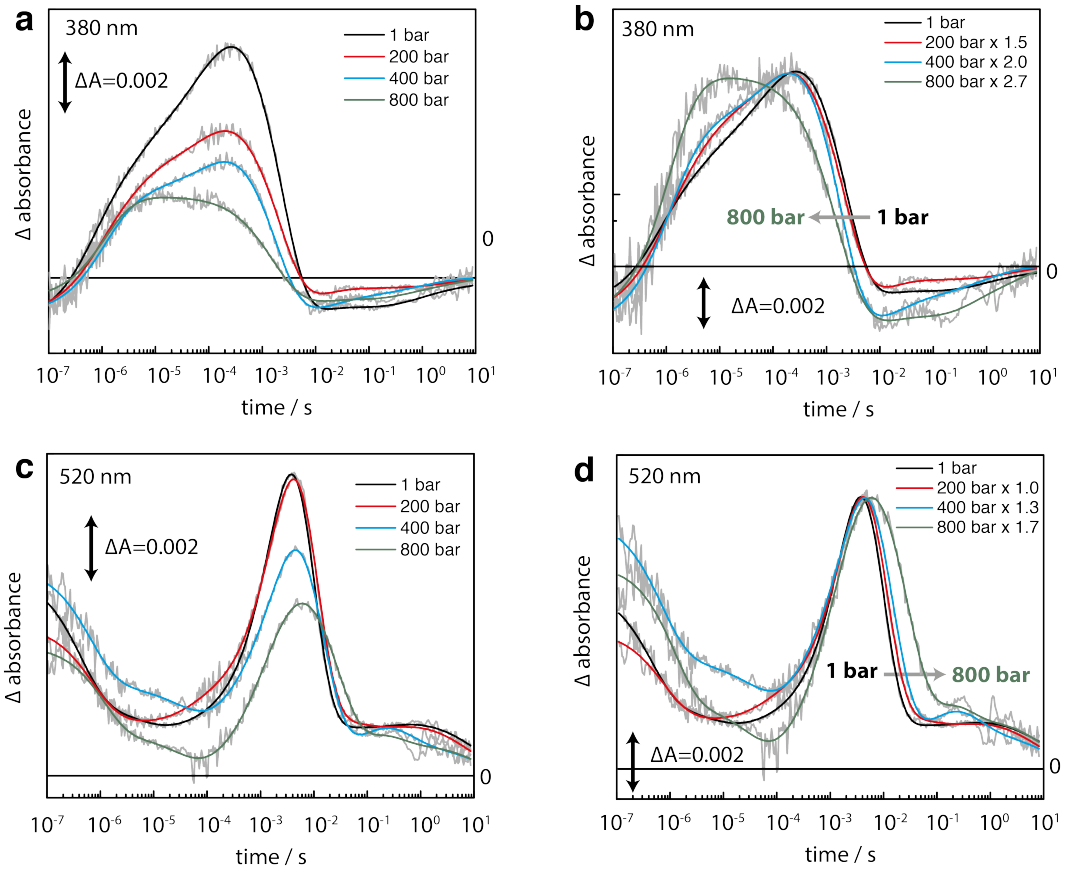

Fig. 3.25: Transient absorbance changes and lifetime distributions of ChR2 reconstituted into nanodiscs at various pressure values. The raw data is shown in grey and the fits are colored according to the applied pressure as indicated from 1 bar (black) to 800 bar (green). The raw and scaled absorption changes at 380 nm are shown in (a) and (b), respectively. The raw and scaled absorption changes at 520 nm are shown in (c) and (d), respectively.

3.7.4 Calculation of activation volumes

The activation volumes are calculated by the logarithm of the rate constant against the pressure as described in equation 1.1 and shown in Fig. 3.26. The graph show the results from ChR2 in detergent, nanodiscs and lipids. The symbols at different colors represent the rate constants or rather the time constants and the solid lines are the corresponding linear fits. The slope of the fits for the rate constants k_1, k_2, k_3 and k_5 is negative; resulting in a positive activation volume ($\Delta V^{\neq}$). In detergent and in nanodiscs, only the decay of the $P_{2b}^{390}$and rise of the P_3^{520} intermediate (k_4) and decay of P_4^{480} (k_6) intermediate show a positive slope and therefore a negative activation volume (see table 3.3). In lipids only the later shows negative change in the activation volume.

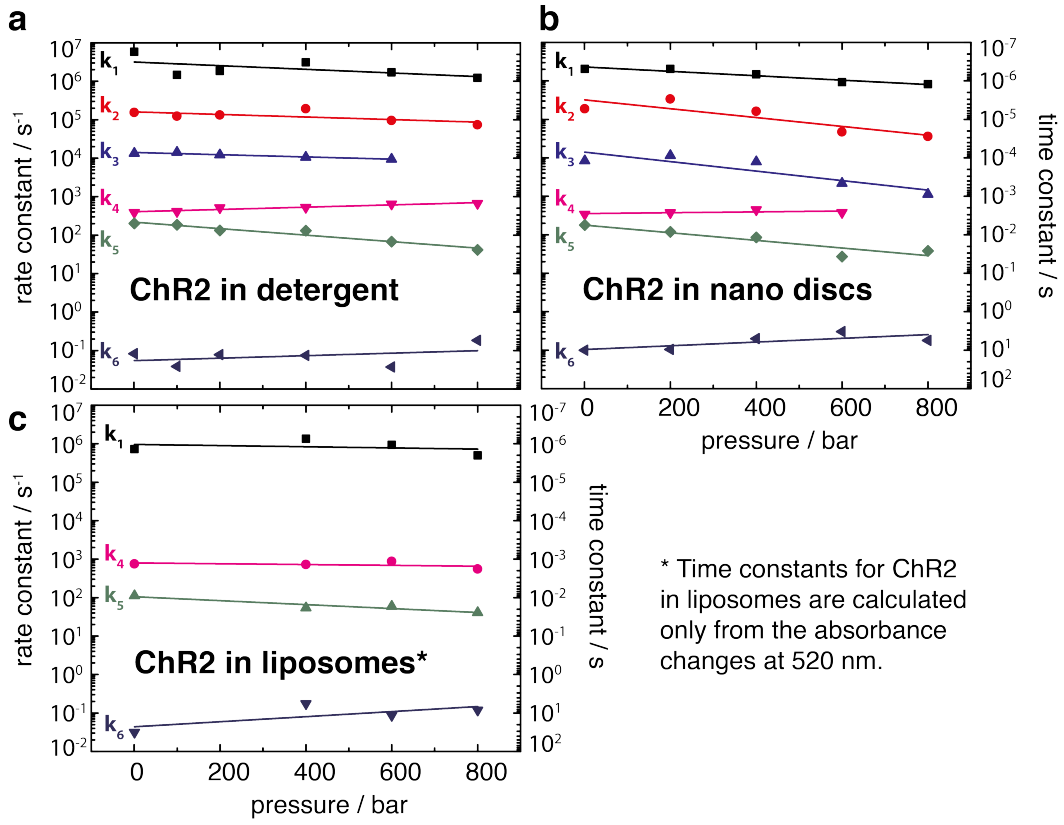

Fig. 3.26: Pressure dependence of the rate constants determined by global fitting analysis at 25°C (symbols) and their linear fits (solid lines). The results are shown for ChR2 solubilized in detergent (a), reconstituted in nanodiscs (b) and lipids (c).

Tab. 3.3: Activation volumes $\Delta V^{\neq}$ of ChR2 solubilized in detergent, or if reconstituted into nanodiscs or in lipid vesicles. (See Figs. 3.23, 3.24, and 3.25 for the kinetic data recorded under various pressures; n.d. = not determined due to low signal-to-noise ratio of the data).

Time constants	ΔV‡ / ml/mol		
	detergent	nanodiscs	lipids
1 (P_{1a}^{500} -> P_{1b}^{500})	+27	+33	+9
2 (P_{1b}^{500} -> P_{2a}^{390})	+19	+66	n.d.
3 (P_{2a}^{390} -> P_{2b}^{390})	+17	+70	n.d.
4 (P_{2b}^{390} -> P_{3}^{520})	-17	-6	+6
5 (P_{3}^{520} -> P_{4}^{480})	+48	+57	+29
6 (P_{4}^{480} -> GS)	-19	-28	-37

Tab. 3.4: Calculated time constants from global exponential fit analysis at different pressures for ChR2 dissolved in detergent or reconstituted in lipidic nanodiscs or in liposomes.

	Pressure	τ_1	τ_2	τ_3	τ_4	τ_5	τ_6
Detergent	1	0.2 µs	6.5 µs	75 µs	2.6 ms	5.0 ms	12 s
	100	0.7 µs	8.1 µs	70 µs	2.4 ms	5.4 ms	26 s
	200	0.5 µs	7.5 µs	82 µs	1.9 ms	7.6 ms	13 s
	400	0.3 µs	5.2 µs	94 µs	1.9 ms	7.7 ms	13 s
	600	0.6 µs	10.5 µs	106 µs	1.6 ms	14.7 ms	27 s
	800	0.8 µs	13.7 µs	---	1.5 ms	24.3 ms	5 s
Nano discs	1	0.5 µs	5.3 µs	120 µs	2.9 ms	5.6 ms	10 s
	200	0.5 µs	3.0 µs	86 µs	2.7 ms	8.4 ms	10 s
	400	0.7 µs	6.2 µs	126 µs	2.2 ms	11.7 ms	5 s
	600	1.1 µs	2.1 µs	458 µs	2.6 ms	37.0 ms	3 s
	800	1.2 µs	2.8 µs	887 µs	---	26.2 ms	6 s
Lipids *	1	1.4 µs	---	---	1.3 ms	8.9 ms	32 s
	400	0.7 µs	---	---	1.4 ms	18.5 ms	6 s
	600	1.1 µs	---	---	1.1 ms	16.8 ms	12 s
	800	2.0 µs	---	---	1.8 ms	24.5 ms	8 s

* only 520 nm and 480 nm fitted

4 Discussion and Conclusion

4.1 Protonation dynamics of ChR2

4.1.1 Transient protonation changes in ChR2

We performed time-resolved step-scan FTIR difference spectroscopy and UV/Vis flash photolysis measurements of photoactivated ChR2. The correlation of photocycle kinetics and changes in vibrational modes reveal three crucial carboxylic amino acids. First, the carboxylate D253 gets protonated during the rise of the P_2^{390} state and thus identified as the primary proton acceptor of the retinal Schiff base proton (Fig. 3.5). Second, the carboxylic acid D156 gets de- and reprotonated during the formation and decay of the P_3^{520} state, which mark D156 as the primary proton donor of the Schiff base (Fig. 3.3b). Third, the de- and reprotonation of E90 takes place during the desensitized P_4^{480} state (Fig. 3.3c, green). The residues are assigned with the help of point mutations: E90A, E123T, D156A, D156E, D253E, and D253N.

The acidic residue at position 253 is conserved in all ChRs so far, but not at position 123 [107]. Furthermore, the replacement of D253 by non-protonatable groups leads to loss of function, i.e. D253A in C1C2 [31] and D253N in ChR2. In contrast, the replacement at position 123 shows a preserved function of the protein [10]. The role of D253 is further supported by the 50-fold accelerated deprotonation event of the retinal Schiff base in the D253E variant (Fig. 3.4). The longer side chain of the glutamic acid places the proton accepting group closer to the protonated Schiff base, resulting in a faster proton transfer reaction, which is reminiscent to the D85E variant in bR [108].
The unusual low frequency of the $C = O$ stretching frequency of D253 at 1695 cm^{-1} needs further explanation. It was found that such low frequencies origin from two effects. First, the $C = O$ group is hydrogen bonded to another amino acid that acts as a hydrogen-bonding donor (e.g. lysine) [90]. Second, the coupling with the $O - H$ bending is hindered by interaction with an hydrogen-bonding acceptor (e.g. carboxylic acid) [109]. We conclude that E123 acts as the hydrogen-bonding acceptor to D253 in ChR2. This is supported by the frequency shift of D253 from 1695 to 1712 cm^{-1} in the E123T mutant (Fig. 3.5). A similar upshift is observed in the D253E mutant where the hydrogen-bonding interaction to E123 is less favorable due to the longer side chain (Fig. 3.5).

D156 is identified as the primary proton donor to the Schiff base by kinetic analysis and point mutation at position 156. This assignment is strongly supported by the extreme prolonged P_2^{390} state in the D156A variant [92]; hindering the reprotonation of the Schiff base. Further, the assignment also explains the kinetic alteration of C128 variants [92]. C128 is hydrogen-bonded to D156 and form a so called "DC-gate" [101]. The DC gate may be necessary to raise the pK_a of D156. If the deprotonated form of D156 is favored, like in the C128T and C128A variants [92], the P_3^{520} state is prolonged. Similar pK_a shifts are observed in the T90A variant in bR [110]. In addition, the KIE supports our interpretation strongly, see section 4.1.2.

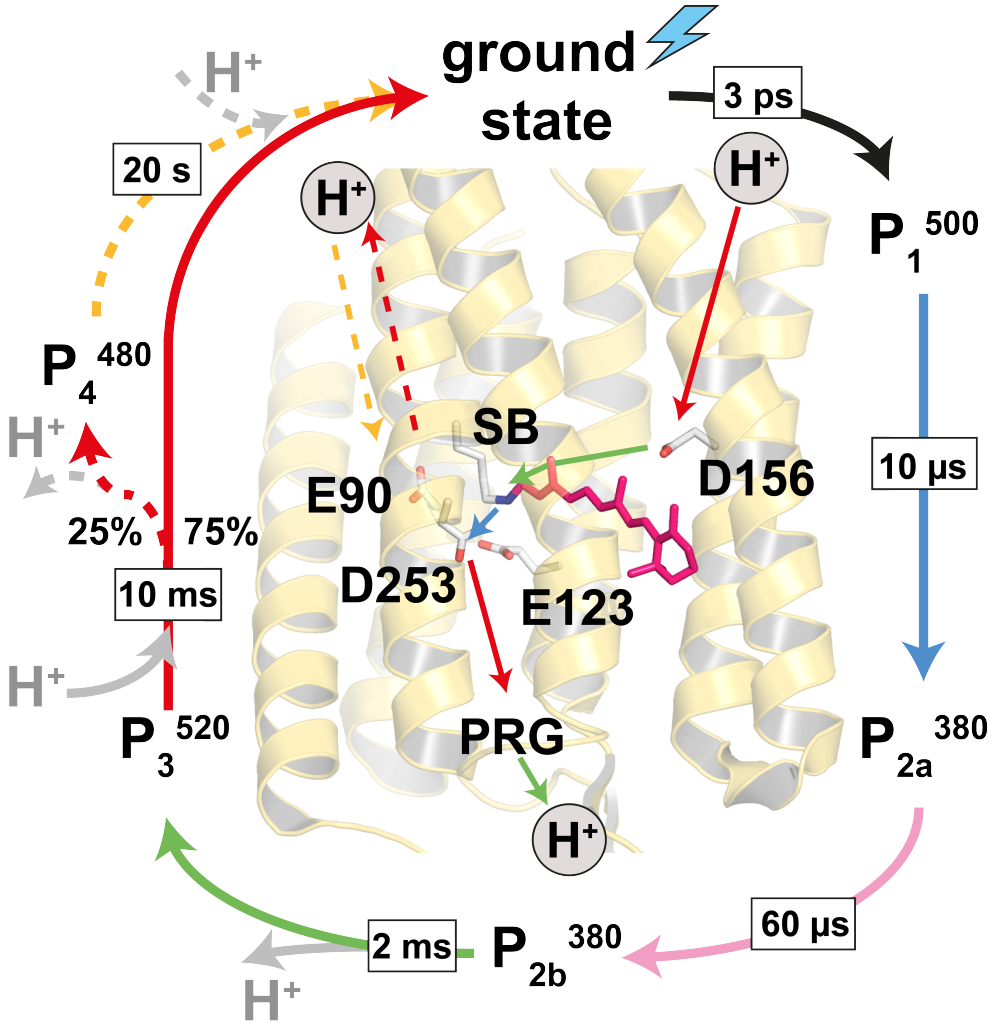

Fig. 4.1: Structure of ChR2 (based on the C1C2 structure [31]) including the proton transfer steps during the photocycle with their $t_{1/2}$ times. The primary proton transfer is directional from the intracellular to the extracellular side. The proton release and uptake from E90 is arbitrarily set to the intracellular side. The proton release group (PRG) and its location is still unknown but preliminarynary fixed towards the extracellular side. The outer arrows indicate the ChR2 photocycle with a branch during the P_3^{520} decay.

The proton transport pathways are summarized in Fig. 4.1 and combined with the structural model based on the C1C2 crystal structure [31]. After light excitation, the retinal isomerizes from the all-*trans* to the 13-*cis* configuration and the P_1^{500} is formed within $t_{1/2}$ = 3 ps [111] (black). The next step leads to a proton transfer from the retinal Schiff to the primary proton acceptor D253 within $t_{1/2}$ = 10 μs (blue). This changes the electrostatic properties of the bound retinal, which leads to a red shift in absorption; the P_{2a}^{390} state is formed. The ion channel is still closed (see section 4.3.1). After 60 μs the P_{2b}^{390} state is formed and the ion flow starts (pink). This is in coherence with the ion conducting prolonged P_2^{390} state in the D156A variant. Therefore, we identified two different P_2^{390} states, although they have identical properties in the UV/Vis. Within $t_{1/2}$ = 2 ms the blue shifted P_3^{520} intermediate is formed related to the reprotonation of the Schiff base via D156 and at the same time a proton is released to the bulk by the proton release group (PRG) [30] (green). The ground state recovery is divided in two separate steps, observed by the integrated area between 1249 and 1227 cm^{-1} [5]. About 75 $\%$ relaxes directly from the P_3^{520} state to the ground state within $t_{1/2}$ = 10 ms (red). At the same time a proton is taken up from the bulk and D156 gets reprotonated. The remaining 25 $\%$ show another proton release event by E90 and the formation of the desensitized P_4^{480} state (red, dashed). This intermediate decays slowly within $t_{1/2}$ = 20 s (orange, dashed) and another proton uptake from the bulk and the reprotonation E90 is observed. The pH indicator experiments this late proton release and uptake event by E90 exhibits a relative amplitude of 20 $\%$, which is closed to the observed 25 $\%$ obtained by the retinal fingerprint region. The retinal fingerprint region is discussed in detail elsewhere [4, 5].

The role of E90 is more difficult to explain. E90 deprotonates during the rise of the P_4^{480} state, which occurs with channel closure. We infer that the deprotonation of E90 leads to the formation of a hydrogen bond with N258 that hinders the dynamic of the adjacent helices. This constriction may reduce the ion conductance. Although not a microbial rhodopsin, this ionic lock system is observed in bovine visual rhodopsin [112]. Analogue, E90 may inhibit the ion conductance under continuous illumination (desensitization). Supportively, E90 variants show a reduced [113] or an abolished [45] desensitization. The protonation events of E90 and D156 are further supported by H/D exchange, as discussed next.

4.1.2 Isotope effects on the proton transfer reactions in ChR2

This chapter is based on Resler et al., 2015, *Biophysical Journal* [34]. The first indications of proton transfer reactions in channelrhodopsin have been derived from time-resolved UV/Vis spectroscopic experiments. In analogy to other microbial rhodopsins, a blue-shifted photocycle intermediate was observed in the photocycle of ChR2 whose rise is associated with the deprotonation of the Schiffbase linkage of the retinal to K257 [6, 114]. This interpretation has been corroborated for ChR1 from *Chlamydomonas augustae* by resonance Raman spectroscopy [47]. Transient proton release and uptake by ChR2 to and from the bulk aqueous medium were detected by pH-sensitive dyes [30]. As discussed in section 4.1, D253 and D156 are identified as acceptor and donor to the retinal Schiff base, respectively [5].

These proton transfer reactions do not only account for the residual proton-pumping activity of ChR2 [29] but it appears that the channel function of ChR2 is also highly dependent on these [4]. As a prominent example for the latter, the reprotonation of D156 is a rate-limiting channel closure, as its replacement by a non-protonatable amino acid delayed the lifetime of the open state from 10 ms to > 150 s [92]. The exchange of D253 to non-protonatable amino acids abolished ion conductance [5, 31, 60]. E90 was shown to decrease its initial high pKa during the photocycle [45], but deprotonation takes place upon formation of the desensitized (nonconductive) P_4^{480} state [5]. This observation explains why the replacement of E90 to non-protonatable amino acids retains ion conductivity with barely affected kinetics [45, 102]. In contrast, recently published molecular dynamics simulations and time-resolved step-scan FTIR results suggested a downward movement of E90, coupled to the deprotonation of E90 in the submicrosecond time range, which opens the pore [35]. This causes an influx of water through the opened pore and a tilt of helix B that fully opens the channel [35]. We showed here that the $C = O$ stretching vibration of E90 (at 1717 cm^{-1} in H_2O and at 1708 cm^{-1} in D_2O) exhibited a significant KIE only after P_3^{520} formation. This result supports our earlier conclusion that the deprotonation of E90 occurs within the lifetime of the P_4^{480}. It is evident, however, that E90 plays a central role in ion selectivity of the channel because replacements lead to drastic alterations in cation selectivity [45]. As a matter of fact, the replacement of the uncharged E90 to the positively charged lysine or arginine residues converts the cation channel into an anion channel [57].

The $C = O$ stretching vibration of carboxylate side chains of aspartic and glutamic acids is diagnostic for proton transfer reactions involving these residues. We developed and applied here, to our knowledge, a novel, time-resolved setup for IR

absorption spectroscopy on the basis of tunable QCLs, which provides a time resolution of 15 ns and exquisite sensitivity. This setup is considered very versatile, and we expect its application to mechanistic studies of proteins of larger size and higher complexity.

D156 of ChR2 was shown to be the internal proton donor to the retinal Schiff base (SB) [5, 35]. Thus, it is interesting to compare the kinetics of the de- and reprotonation of D156 in ChR2 with D96, the proton donor to the retinal SB in bR (Fig. 4.2A). The pKa of the latter residue is > 12 [115] and drops during the photocycle down to 7.1 [89]. The frequencies of the $C = O$ stretches of D156 and D96 appear with 1736 and 1741 cm^{-1}, respectively, in a range that is typical for the carbonyl oxygen accepting a single hydrogen bond. Thus, the $C = O$ probe a local vicinity similar in electrostatics for both residues. Despite the fact that the two residues localize at very different spatial positions within the respective proteins, the distances to the SB are with 10 Å (Fig. 4.2B) and 11 Å (Fig. 4.2C) also similar. Although proton transfer take place during intermediate state transitions that involve structural rearrangements, it is not surprising that the proton transfer from the respective donors to the retinal SB take place in the same time range of 1–100 ms (Fig. 4.2A).

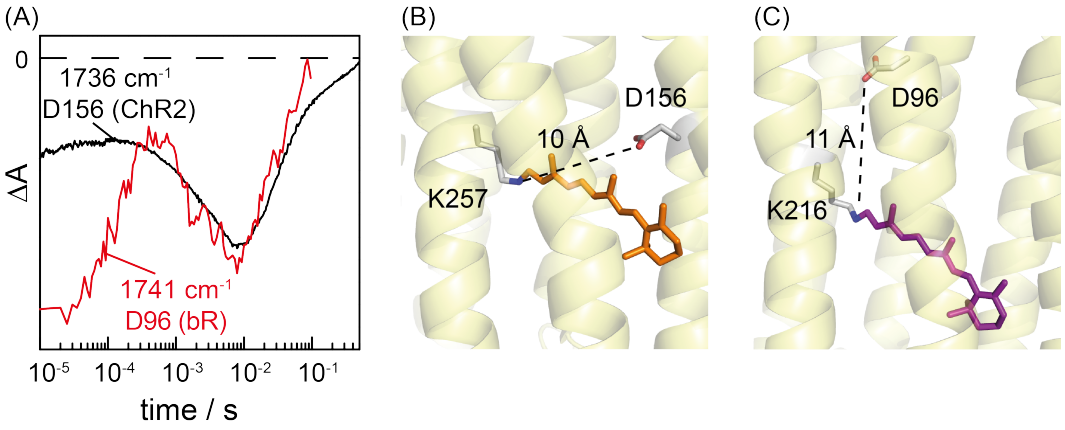

Fig. 4.2: (A) Transient absorption changes of the $C = O$ stretching vibrations of the primary proton donors of D156 of ChR2 and D96 of bR. The kinetics recorded at 1736 cm^{-1} correspond to D156 of ChR2 (black trace) and is redrawn from Fig. 3.10. For comparison, the kinetics at 1741 cm^{-1} of D96 of bR (red) is replotted from Zscherp et al. [89]. (B) Structure of channelrhodopsin (PDB:3UG9) including the distance of the internal proton donor D156 to the retinal Schiff base. (C) Structure of bacteriorhodopsin (PDB:1C3W) including the distance of the internal proton donor D96 to the retinal Schiff base. The distances given are from the N of the retinal Schiff base to the carboxylic OD2 of D96 in bR and to the carboxylic OD1 of D195 in the C1C2 chimera (corresponding to D156) of ChR2, respectively [34].

Despite the coincidence in kinetics, and additional experimental evidence as reviewed recently in Lorenz-Fonfria and Heberle [26], the role of D156 as the SB proton donor has been challenged [33, 35], as well as the timing of E90 deprotonation [35]. Therefore, additional experiments were demanded and the determination of deuterium isotope effects represents a means to gain insight into the role and timing of the proton transfers in the photocycle of ChR2.

Using time-resolved UV/Vis spectroscopy, we determined only a small KIE (< 2) for the rise of the P_2^{390} state, the photocycle intermediate with deprotonated SB. This result is in strong contrast to bR where the rise of the M state exhibits a much larger KIE of ≈ 5 (Table 3.1). It is concluded from this result that deprotonation of the Schiff base is not rate limiting in ChR2, but it is in bR. Furthermore, the P_2^{390}-to-P_3^{520} as well as the P_3^{520}-to-P_4^{480} transitions show a stronger KIE in ChR2 (3.3 and 3.2, respectively) than corresponding transitions in bR (KIE < 2). This indicates that proton transfer is rate-limiting during the lifetime of the late intermediates of the ChR2 photocycle. Although proton-pumping bR and ion-conducting ChR2 share structural and mechanistic similarities, the different KIEs indicate distinct differences in their proton transfer pathways. This is in agreement with different residues playing the role of the SB proton acceptor/donor: D253/D156 in ChR2 (equivalent to residues D212/D115 of bR), while the SB proton acceptor/donor pair in bR is D85/D96 (equivalent to residues E123/H134 of ChR2).

The comparison of the time-resolved absorption changes bands in the carboxylic region show that all observed $C = O$ vibrations are sensitive toward H/D exchange (Fig. 3.9) but to variable degrees. The KIE for the deprotonation/protonation of D156 (Fig. 3.10) is very similar to the KIEs of formation and decay of the P_3^{520} state as detected in the visible (Table 3.1). This result further supports our previous identification of D156 as the primary proton donor [7]. This assignment has recently been challenged by Ito et al. [33] and by Kuhne et al. [35]. These authors argued from the H/D insensitivity of the $C = O$ stretching vibrational band of D156 [7, 32, 33, 35] that the O-H group of the carboxylic group of D156 is not exchangeable, refuting the role of D156 as proton donor to the retinal Schiff base [33, 35].

In fact, we observed here that the $C = O$ stretch of D156 is sensitive to H/D exchange, albeit with an unusual frequency upshift by 2 cm^{-1} (Fig. 3.10a), instead of the typically observed downshift by 5–10 cm^{-1} of this vibration. It is pointed out that the $C = O$ stretch of D156 exhibited a more typical downshift by 5 cm^{-1} (from 1761 to 1756 cm^{-1}) during the lifetime of the P_1^{500} intermediate (Fig. 3.9). The typical H/D-induced downshift by 8 cm^{-1} (from 1763 to 1755 cm^{-1}) is apparent in the D156E variant, demonstrating that the carboxylic group at position 156 is

indeed accessible to H/D exchange. Thus, our results resolve the major argument against the assignment of D156 as the proton donor to the Schiff base.

What is left to be discussed is the scenario of the hydrogen-bonded network surrounding the carboxylic group of D156 that accounts for the observed 2 cm^{-1} frequency upshift of the $C = O$ stretching vibration after H/D exchange, as well as the 27 cm^{-1} (in H_2O) upshift upon exchange from Asp to Glu. It is well known that the frequency of the $C = O$ stretch of a carboxylic group is modulated by H-bonding [90, 91, 116, 117], not only due to direct H-bonding to the $C = O$ group, but also to the O-H of the carboxylic group.

The frequency of the $C = O$ stretching vibration can upshift by >12 cm^{-1} and downshift by >70 cm^{-1}, depending on the H-bonding configuration according to quantum-mechanical calculations [90, 91]. Differences between the strength of H-bonds and D-bonds [118] to the $C = O$ group might induce different shifts in the $C = O$ vibration. An H-bond between the S-H group of cysteine and the $C = O$ of a carboxylic group, as was proposed for the DC gate [26, 101], is expected to downshift the $C = O$ frequency by 17 cm^{-1} according to calculations performed on protonated carboxylic acids in vacuo [90]. In E156, this H-bond is possibly disrupted due to the longer side chain of Glu with respect to Asp, accounting for the 27 cm^{-1} higher $C = O$ frequency in the D156E variant (Fig. 4.3).

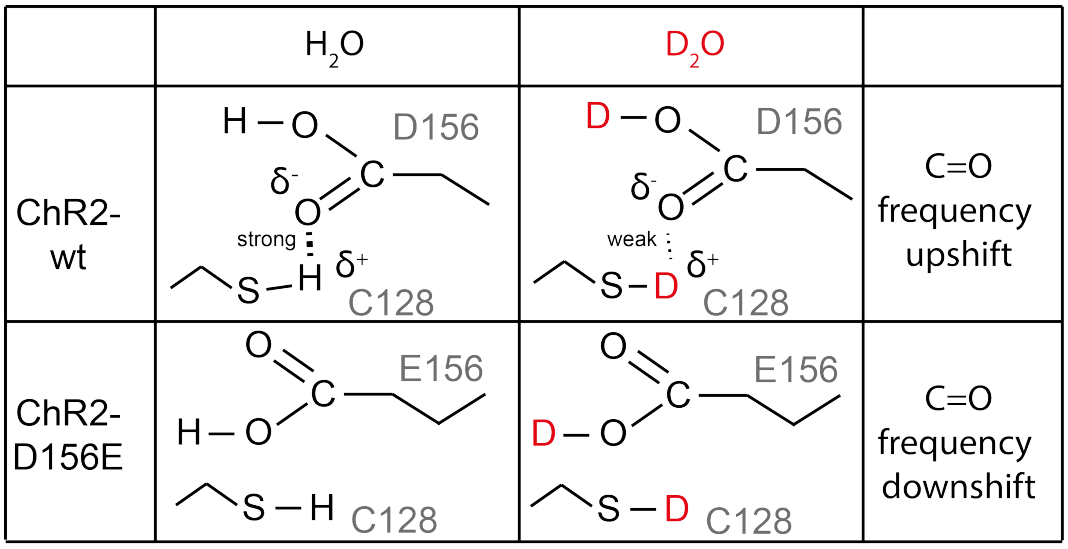

Fig. 4.3: Illustration of the hydrogen-bonding interaction of C128 and D156 (DC gate) in H_2O and D_2O. This model explains the different VIEs of D156 and E156 upon H/D exchange [34].

It should be noted that S-D groups are expected to be less polarized than S-H groups, as deduced by the 2.5 lower extinction coefficient of S-D stretches with respect S-H stretches [119, 120]. Under this reasonable assumption, deuteration of

C128 will reduce the strength of its H-bond with D156, presumably upshifting the $C = O$ vibration and compensating the down- shift caused by the deuteration at the hydroxyl group of D156 (Fig. 4.3).

Recent FTIR spectroscopic experiments recorded on the C1C2 chimera and its variants, in which the corresponding residues of D156 and C128 have been replaced [121], agree very well with these data on ChR2. Thus, we consider the correlation of FTIR experiments that resolve structural changes of ChR2 with the dark-state structure of C1C2, as determined by x-ray crystallography [31], to be valid and meaningful. Deviations in the photocycle kinetics of the two variants of channelrhodopsin, ChR2 and C1C2, have been noted [121], but are irrelevant as long as time-resolved approaches succeed in being used for separate photocycle states, as was shown here.

Atypical shifts in the carboxylic region, as shown here for the $C = O$ stretching vibration of D156 in dark-state ChR2, have also been reported for the $C = O$ stretching vibration of D96 in the L intermediate of bR [99]. In this latter case, the $C = O$ frequency of D96 in the ground state showed a normal 9 cm^{-1} downshift in D_2O (from 1741 to 1732 cm^{-1}), but in the L intermediate the frequency exhibited a mere 1 cm^{-1} downshift (from 1748 to 1747 cm^{-1}) [99]. Maeda et al. [99] suggested a putative H-bond of the hydroxyl group of D96 in the L intermediate as the cause for the anomalous shift upon deuteration; a suggestion that, to our knowledge, still lacks confirmation. In any case, anomalous shifts in the frequency of the $C = O$ stretch of carboxylic groups of proteins upon deuteration might indicate an unusual arrangement of H-bonds, whose characterization are best addressed by applying sophisticated quantum-mechanics/molecular-mechanics calculations [107, 117, 122].

4.2 Photoreactions of ChR2 under conditions with negligible channel activity

4.2.1 13-*cis* photocycle of ChR2-E123T (ChETA)

Gating of ChR2 is initialized by photoisomerization of the retinal chromophore. In the light-adapted ground state it contains a mixture of the 70% all-*trans* retinal and 30% 13-*cis* retinal [46, 47]. For investigation of the 13-*cis* photocycle we analyzed the kinetics of the fast-cycling functional ChR2-E123T variant of channelrhodopsin-2, also known as ChETA. It was shown by electrophysiology that under continuous

illumination two different photocycles are necessary to explain the results [21, 48, 49]. Both open states decay with a time constant of 10 and 40 ms. We performed time-resolved IR and UV/Vis spectroscopy with ns time-resolution. The analysis of the $C-C$ and $C=C$ stretching vibration of the retinal allows the distinction between the 13-*cis* and all-*trans* photocycle at 1552 and 1558 cm^{-1}, respectively (see Fig. 3.13). The overlap was reduced by band narrowing methods. We observed, that the recovery of the proton transfer reactions are linked exclusively to the all-*trans* photocycle. The analysis of time-resolved UV/Vis and IR data provides evidence that the 13-*cis* photocycle recovers within 1 ms, which is faster than channel closure and reprotonation of the Schiff base. Thus, we conclude that the 13-*cis* photocycle is of minor functional relevance in ChR2 (see Fig. 4.4). It was recently suggested that the open state of the second photocycle could originate from the photocycle of 13-*cis* retinal [51]. This suggestion directly conflicts with our current findings, described in detailed elsewhere [4].

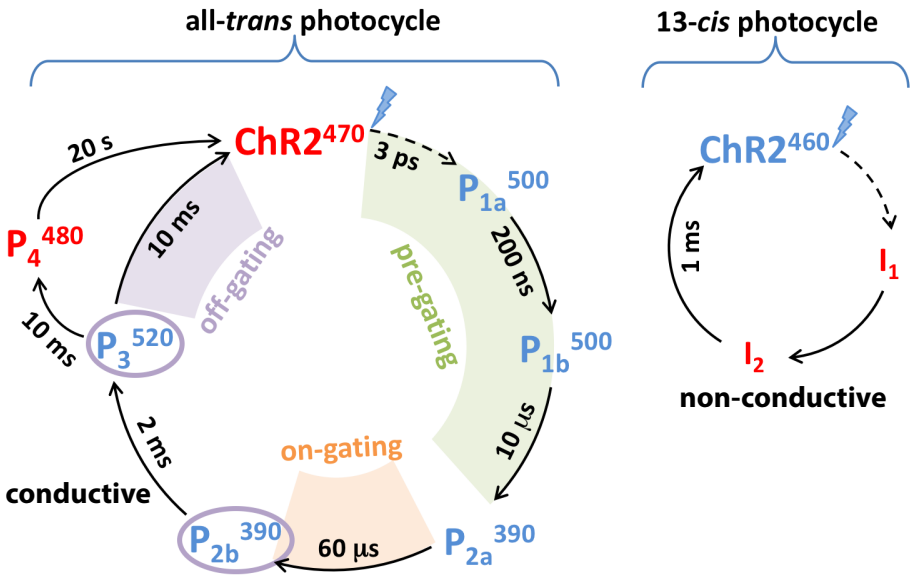

Fig. 4.4: Comparison of the all-*trans* and 13-*cis* photocycle of ChR2 [52].

Further, we observed early structural changes in ChR2-E123T. They are assigned as "pre-gating" and discussed in more detail in our publication [52] and resolved in section 4.3.1. To our knowledge, it was the first time that these early structural changes of the apoprotein are presented for any ChR.

The UV/Vis data of ChR2-E123T was compared with ChR2-wt. It shows a native-like photocycle with some minor spectral and kinetic differences with respect to the WT. The ground state recovery from the P_4^{480} intermediate is 5-times faster and the absorption of the bound retinal is red shifted in the E123T variant in respect to WT. Therefore we conclude E123 in ChR2-wt remain ionic across the entire

photocycle. This interpretation fits with our proton transfer model of ChR2 and recent interpretation that E123 act as a primary proton acceptor [35] are ruled out.

4.2.2 Loss-of-function variant R120H

I presented joined time-resolved IR spectroscopic data and the analysis of ChR2-wt and the non-functional ChR2 variant: R120H. Surprisingly, the ion flow vanishes while the proton transfer reaction of the retinal are preserved as shown by voltage-clamp recordings (Fig. 3.15) and flash photolysis (Fig. 3.16). The observed time-constants and DADS fit well with those obtained for ChR2-wt [34]. Thus, R120 is not part of the proton transfer pathway. By time-resolved IR difference spectroscopy I investigated the kinetics of vibrational modes. Furthermore, I demonstrated that time-resolved IR difference spectroscopy by vis-pump and IR-probe ranging from 0.4 ps to 1.8 ns and by tunable QCL ranging from 10 ns to 1 s can be combined in one set of data covering almost 13 decades in time. Although the excitation wavelength and pulse length are not identical in both experiment, the spectral kinetics are compatible. These joined IR spectroscopic methods are applied on ChR2-wt and the R120H variant. With this approach, we identified that small spectral features are different but the overall spectroscopic result is similar to wild type, except for the band at 1580 cm^{-1}. It decays within 10 ps in the R120H variant and is not present till 2 ns, where the band rises and decays within 5 ns. This band could be spectrally assigned to the asymmetric stretching mode that couples to the $N - D$ scissor vibration, as shown by the model compound analysis of guanidine hydrochloride during deprotonation. However, this interpretation is unlikely, according to the time-scale of several picoseconds. It is more conclusive that this vibrational mode is caused indirectly when the arginine is present, forming the extracellular vestibule (see explanation below).

In addition, we used PROPKA 3.1 (Version 3.1, 07/01/2011, Copenhagen) for pKa calculation of the C1C2 chimera (Table 4.1). For further information see Li et al. [123] and Søndergaard et al. [124]. H173 (H134) and H288 (H249) show an unusual low pKa value of 1.33 and 1.14 and attractive coulomb interactions with the positively charged arginines R307 (R268) and R159 (R120), respectively. (The number of the residues in parenthesis is according to ChR2). From this calculation I conclude that both histidines are likely to be deprotonated and both arginines are likely to be protonated in the ground state at pH 7.4. As indicated in Fig. 4.5 the corresponding amino acids are in planar orientation to each other within a distance of 3.5 Å. Although hardly discussed, weak attractive aginine-histidine interactions are observed by molecular dynamic simulations [125–127]. At least

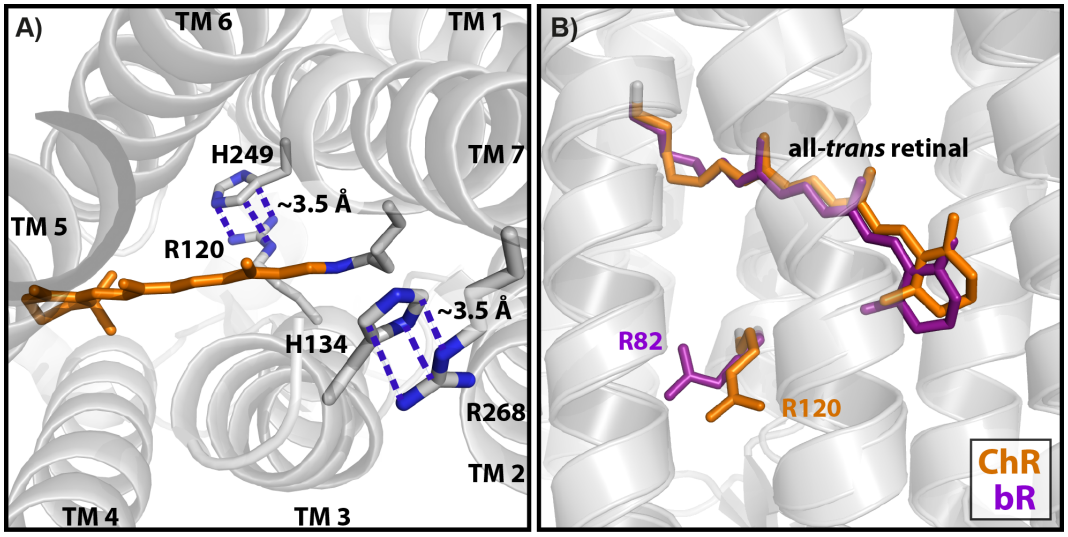

Fig. 4.5: (A) Structure of channelrhodopsin (C1C2, PDB ID: 3UG9) including the average distance of two Histidine-Arginine pairs, both located on transmembrane (TM) 3 and 7. Numbering according to the ChR2 sequence. (B) Comparison of ChR (orange) and bR (purple) by structure alignment. The Schiff base bound retinal and the conserved arginine (R120 in ChR2; R82 in bR) are highlighted.

in water attractive interactions between arginines [125] and histidines [127] are caused by an interplay of quadropole-quadrupole, dispersion and cavitation forces. Thus, despite coulomb repulsion, a contact pair is formed to stabilize the protein structure [127].

Interestingly, it was shown that the variants H134S/Y/R (in ChR1 and ChR2) only influences the photocurrents slightly [128, 129], but the replacement of the neutral histidine to an aspartic acid blocks the photocurrent [8], maybe caused by strong interaction with the positively charged arginine (R268). On the other side, removal of the positive charge at residue 268 leads to mutants with no observable light-induced currents (*not shown, work in progress*). The same is true for the mutant of E82 [113], which forms an coulombic interaction with R268. Hence, it is getting clear from the different phenotypes of the mutant that the interaction network of R268 plays an important role for the channel functionality: The linkage to transmembrane (TM) helix B (E82) might be important for structural reasons, the defect from the single point mutants can not be rescued by the double mutant E82R/R269E. This view is in line with the reported decreased surface expression E82 [113]. On the other side, the interaction between TMH G (R268) and TMH C (H134) could tune the lifetime of the open state. Decreasing the interaction (H134R) would lead to a longer lifetime [129] as observed, while a stronger interaction than the His-Arg type would strongly decrease the lifetime leading to smaller current amplitudes like in

Tab. 4.1: Calculated pKa values of specific histidine and arginine based on the C1C2 chimera (PDB: 3UG9). Numbering according to C1C2, numbering in parentheses corresponds to ChR2. PROPKA (version 3.1, 07/01/2011, Copenhagen) was used for calculation at pH 7.4 and with PARSE force field.

Amino acid side chain	pKa value	Buried	Columbic interactions
H173 (H134)	1.33	100%	**-1.68 R307 (R268)** -0.09 H304 (H265)
H288 (H249)	1.14	100%	**-2.03 R159 (R120)** -0.37 L132 (L93) -0.13 L296 (L257)
R159 (R120)	12.80	100%	1.43 Y160 (Y121) 1.25 E274 (E235) 0.33 D292 (D253) 0.16 E136 (E97) 0.12 E162 (E123)
R307 (R268)	12.04	78%	0.85 E121 (E82) 0.35 E122 (E83) 0.24 Y184 (Y145)

the Asp-Arg type. Similar tuning mechanisms have been suggested for voltage-gated channels [130].

The structural similarities to the well studied bacteriorhodopsin, suggest a detailed comparison with ChR2. As shown in Fig 4.5B both crystal structures (bR and C1C2) are compared. R120 in ChR2 (orange) is conserved in the C1C2 chimera (R159) and in bR (R82, purple). The arginine of bR is rotated towards the Schiff base in contrast to ChR, where it is rotated to the extracellular side. This structural rearrangement may also contribute to a different functional role. R82 was found to be part directly [131] or indirectly [132, 133] involved in the proton release. The reorientation, i.e. rotation towards the extracellular site was supported by time-resolved electrical measurements [134]. The pH indicator experiments that detect the proton uptake and release were measured for the variants: S245E [30] and R120H. Both variants show neither an alternation of the photocycle kinetics nor an influence on the proton release and uptake. Thus, S245 and R120H cannot be part of the proton release group like E204 and R82 in bR, which forms a proton release cluster with E194 [131].

We demonstreted by time-resolved spectroscopy that the proton transport pathway is not affected but, however, the ion conductance is prevented. Our observation supports the conclusion by Kato et al. that R120 plays an important role in formation

of the extracellular vestibule instead of proton transfer [31]. Thus, other mutations, which lead to a collapse of the vestibule, which seems to be a requirement for gating, may prevent the ion flow as well. This is also in coherence with the recently published gating mechanisms [35, 58] and would explain that this arginine is highly conserved in different channelrhodopsins [27].

In summary, this technical advancement of joined IR difference spectroscopy will discover detailed information of light triggered protein, by following the time traces of vibrational modes directly after photo excitation until there physiological function takes place, i.e. tracking of structural changes, protonation dynamics and other events with an unprecedented spatial and temporal resolution.

4.3 Structural changes during the ChR2 photocycle

4.3.1 Temporal evolution of helix hydration

In the past two decades, the overall understanding of ion channels has improved thanks to static atomic structural information on trapped inactive and conducting states. Dynamic information were complemented by MD trajectories often in the nanosecond time scale and focusing on the role of water molecules [135]. Recently, using all-atom molecular dynamics simulations, the switches between activated and deactivated states of a voltage-gated potassium channel was simulated. Hundreds of microseconds were covered, water dynamics and structural changes in the protein were sampled across the relevant time scale for channel gating, providing mechanistic insights [136].

Experimentally, time-resolved IR spectroscopy is a label-free technique combining structural sensitivity with high temporal resolution. So far, technical challenges have limited the application to study ion channels [137]. As shown in this thesis, ChR2 is triggered by light and may act as a model system for other ion channels. Therefore, time-resolved electrophysiology and optical spectroscopy with a temporal resolution in the μs range can be applied and compared. We observe that the conductive state is not associated with an intermediate state in the visible, i.e. specific protonation or conformational state of the retinal. But ion conductance tallies with vibrational modes of the protein backbone that shift from 1665 to 1648 cm^{-1}. This correlation holds true for the fast (E123T) and slow (D156E) channeling variants (Fig.3.21). These bands report the hydration of transmembrane α-helices: 1665 cm^{-1} for dry

and 1648 cm^{-1} for hydrated helices. As shown by electrophysiology measurements, ion conductance starts with $\tau \approx 200\ \mu s$ and ends with $\tau \approx 10\ ms$. Interestingly, partial helix hydration takes place within $\tau \approx 10\ \mu s$, i.e. before cation permeation starts, thus water influx occurs in two steps. In the first step, one-third of the helix hydration takes place within $\tau \approx 10\ \mu s$; insufficient for ion conductance. In the second step, the remaining two-third of the helix hydration occurs within $\approx 200\ \mu s$, which leads to ion conductance by forming a continuous water-filled channel. The minor pre-gating step occurs at 10-15 μs in both variants (E123T and D156E) independently of differences in the start of ion permeation. But the major hydration step correlates well with the altered on-gating kinetics of the variants: E123T ($\tau \approx 180\ \mu s$) and D156E ($\tau \approx 1.5\ ms$). The dewetting of alpha helices tallies with channel closure, which follows ground state recovery: $\tau \approx 10\ ms$ in WT, $\tau \approx 4\ ms$ in E123T, and $\tau \approx 60\ ms$ in D156E. In combination with our observed protonation dynamics (sections 4.1 and 4.1.2).

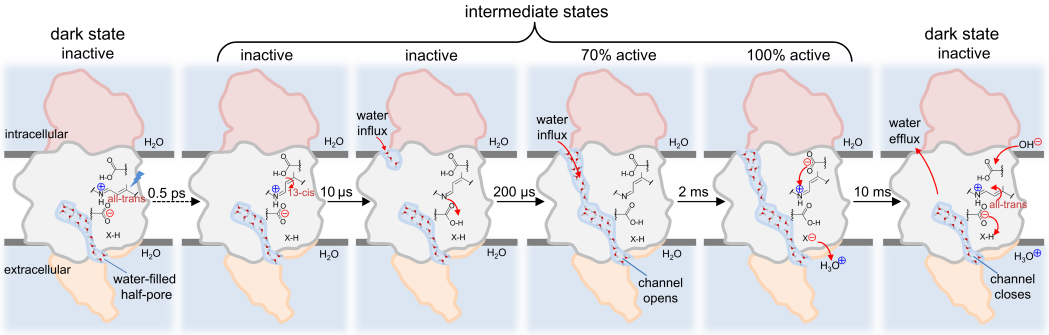

Fig. 4.6: Schematic representation of the gating steps in ChR2 after light excitation. Water filled pore, water influx and efflux steps, protonation dynamics, retinal isomerization, and proton pumping steps are highlighted. The water influx (helix hydration) are divided in two different but cooperative steps ($\tau_1 = 10\ \mu s$ and $\tau_2 = 200\ \mu s$); during the latter step cation permeation starts. It ends within $\tau = 10\ ms$ by dewetting of the helices and the related collapse of the ion conducting pore. The proton release group (PRG) is still unknown and represented by X-H [58].

The location of the hydrated α helical segments are still elusive, but the surrounding close to the putative ion channel (i.e. between helices A, B, C and G) seems likely. The quantity of water molecules involved in helix hydration is around 20, which is sufficent to hydrate the helices and forming a pore. The number is roughly estimated from the area of the amide I band at 1648 cm^{-1}. Similarly, in the voltage-gated potassium channels an influx of 40-50 water molecules, in the transition between inactivated and activated state, are observed [136, 138].

The pre-gating step with partial water influx $\tau \approx 10\ \mu s$ correlates with the deprotonation event of the retinal Schaff base in ChR2 [5]. Similar to bacteriorhodopsin (bR) this water influx is maybe due to a small outward movement of helix B [139].

Consequently, the formation of the conducting pore at $\tau \approx 200\ \mu s$ may origin from a larger outward movement of helix B, as observed by EPR studies [56, 62]. From our data two sequence in events are possible: Structural changes lead to water influx or water penetration allows for structural changes.

As schematically shown in Fig. 4.6, the ion conductance within $\tau \approx 200\ \mu s$ exhibits only 70 $\%$ conductance in comparison to the fully active state with $\tau \approx 2$ ms. Surprisingly, this increase in conductance is not correlated with water influx. With the same time constant, the transition between the P_2^{390} and P_3^{520} state are observed, as described in section 4.1 [5]. Hydrogen-bonding rearrangements and protonation changes, i.e. the reprotonation of D156, might affect the polarity of the ion-conducting pore, or electrostatic changes might locally increase the voltage, accounting for the increase in ion conductance. In summary, we found by cross-correlated of time-resolved electrophysiology and step-scan FTIR measurement, that ion conductance tallies with hydration of α-helices in ChR2.

4.3.2 Photocycle kinetics of ChR2 at various pressures

I have determined the effect of hydrostatic pressures on the photocycle kinetics of channelrhodopsins (ChRs) to determine the activation volumes of the photocycle intermediates starting from 10 ns. Specifically, I wanted to investigate the role of pressure and how this influences volume changes that origin from de- and reprotonation events of the retinal Schiff base, i.e. the photocycle kinetics. All samples were measured under different pressures, raising from 1 bar to 800 bar and their time constants are obtained by global exponential fitting and lifetime distribution. The activation volumes are determined and a strong (but reversible) effect on the amplitudes for all kinetics is observed already at 200 bar. These results are summarized in Fig. 4.7 and will be discussed in the following in the framework of known molecular reactions of ChR2. For ChR2 solubilized in detergent we found that the early transitions show only positive activation volumes (Fig. 4.7, green background). These transitions reflect pre-gating of the ion channel [52] as was inferred from time-resolved FTIR difference spectra. The rise of the P_2^{390} state indicates deprotonation of the retinal Schiff base. The proton is transferred to D253 (primary proton acceptor). We note, that the water influx associated with pregating of the ion channel is not correlating with the intermediate states in the visible. Thus, these activation volumes reflect only the charge neutralization and some conformational changes.

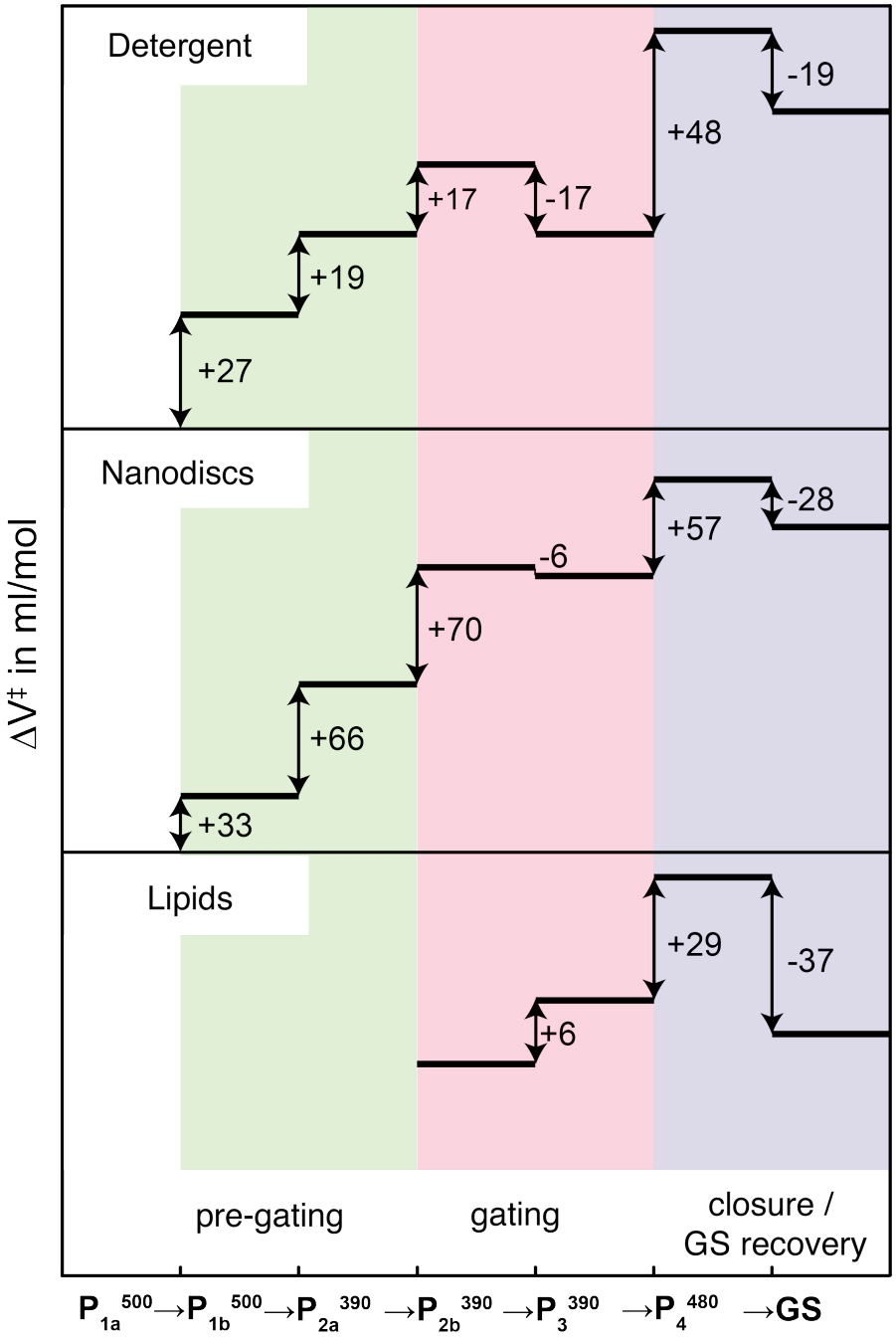

Fig. 4.7: Determined activation volumes of the kinetic processes during pore formation. The results are shown for ChR2 solubilized in detergent (top), reconstituted in nano discs (middle) and lipids (bottom). The pre-gating, gating and closure (ground state recovery) are highlighted in green, red and blue, respectively.

The rise of the P_3^{520} state reflects the reprotonation of the retinal Schiff base from the primary proton donor D156 (as described above) [5, 34] and the simultaneous proton release as detected by a pH indicating dye [30]. This reaction is accompanied by a negative activation volume (Fig. 4.7, red background). Generally, ion pairs are destabilized under hydrostatic pressure caused by the electrostrictive effects of separate charges: water molecules that arrange for charge compensation are more densely packed than in bulk water [66]. This explains the negative activation volumes during the P_3^{520} formation (-17 ml/mol). During the decay of the P_3^{520} intermediate, D156 gets reprotonated from the bulk [5, 34] and the ion channel closes by dewetting of the helices [58]. Resulting in a positive activation volume of +48 ml/mol for ChR2 in detergent. This result is in agreement with the idea that the exposure of hydrophobic residues is favored under high pressure [66]. During this decay, 75% of the activated proteins relax back to the initial ground state and 25% form the desensitized P_4^{480} state, which is characterized by E90 de- and reprotonation. The decay of the P_4^{480} state is associated with negative activation volumes (-19 ml/mol), see Fig. 4.7, blue background. This is in contrast to the expected positive volume changes for charge neutralization of a carboxylic acid, see Gross et al. [66], but the back reaction from P_4^{480} to the ground state involves also structural changes which may compensate these effects.

To account for different protein environments, (which may affect the volume changes), we have measured and analyzed the photocycle kinetics of ChR2 solubilized in detergent and reconstituted into the lipidic environment as provided by nanodiscs or by liposomes. The visible absorption changes of ChR2 reconstituted in nanodiscs show the expansion and compression at the same transition states, like ChR2 dissolved in detergent. But the expansions on the early transitions (pre-gating and the first gating step) are larger (+33 , +66, +70 ml/mol), see Fig. 4.7. The negative activation volume of -6 ml/mol during the gating step is slightly smaller than in detergent. The closure of the channel shows positive (+57 ml/mol) and the ground state relaxation negative changes (-28 ml/mol) of the activation volume. The small differences between ChR2 solubilized in detergent and the reconstituted into nanodiscs might refer to the more rigid structure of the nanodics.

ChR2 reconstituted into liposomes made of POPC lipids show a smaller positive activation volume change during the P_{1a}^{500} to P_{1b}^{500} transition. The P_2^{390} transition cannot be monitored due to scattering. The result for the liposomes during the rise of the P_3^{520} state (+6 ml/mol) might origin from surface bound protons. For ChR2 in detergent we could neglect surface-bound protons during the proton release and uptake event [30]. The lipid vesicles or batches are larger than the nano discs,

which is observed by a strong scattering. This results in a higher probability for a surface-bound proton.

Pressure dependent measurements were performed for other microbial rhodopsins, which show structural similarities but different functions; like the proton pump: bacteriorhodopsin. Klink et al. investigated the pressure dependency of the bR photocycle kinetics [73]. The time constants of the M state formation was found to be pressure insensitive, in contrast to the work of Marque and Eisenstein, where larger pressure effects were observed [65]. In addition, Varo et al. observed large activation volumes during the M decay [72]. Interestingly, for wild-type bR only positive activation volumes were reported in all three publications. Marque and Eisenstein explain this effect by a modulation of the intrinsic membrane viscosity under high-pressure [65], as reported by viscosity measurements on bR [140]. It was shown for bacteriorhodopsin that the isomeric composition of the retinal in the ground state is shifted from the all-*trans* to the 13-*cis* configuration [141, 142]. Although the ground state absorption spectra of ChR2 is hardly shifted (see Fig. 3.22), the isomeric composition might be shifted towards the 13-*cis* configuration of the retinal in the ground state. This may explain the reduced amplitude of the intermediate states, because the 13-*cis* photocycle exhibits different intermediate states and a faster photocycle [52]. Although we cannot rule out that the quantum yield of the initial reaction is reduced by increased pressure. Further investigation of the volume changes by photoacoustic measurements or pressure dependent time-resolved measurements in the infrared might help to further analyze the volume changes of ion channels like ChRs.

5 Summary and Outlook

The discovery of light-gated ion channels set the stage for the new and vibrant field of optogenetics, where action potentials in neuronal cells are triggered by light. Channelrhodopsin-2 (ChR2) from the green algae *Chlamydomonas reinhardtii* is the most widely used optogenetic tool in neuroscience, but the underlying molecular mechanism remain elusive. In this work, I scrutinized the fundamental molecular processes of protonation dynamics and structural changes that lead to ion permeation in ChR2.

Transient absorbance changes in the UV/Vis and IR region are recorded by time-resolved spectroscopy. Three-dimensional data sets simultaneously showing frequency and amplitude over time were analyzed to resolve transient vibrational changes that represent the gating as well as proton transfer events. In ChR2, the visible light is absorbed by a retinal chromophore bound to a protonated Schiff base. Aspartate 253 (D253) is identified as primary proton acceptor and aspartate 156 (D156) as primary proton donor of the Schiff base. Because proton transfer reactions play a key role in channel gating, the vibrational and kinetic isotope effects (VIE/KIE) are determined of various aspartic and glutamic acid residues by monitoring their $C=O$ stretching vibrations in H_2O and in D_2O. D156 exhibits a KIE >2 in deprotonation and reprotonation, which substantiates its role as internal proton donor to the retinal Schiff base. The unusual VIE of D156, upshifted from 1736 cm^{-1} to 1738 cm^{-1} in D_2O, was scrutinized by studying the variant D156E. The $C=O$ stretch of E156 is down shifted by 8 cm^{-1} in D_2O, providing evidence for the accessibility of the carboxylic group. The $C=O$ stretching band of E90 exhibits a VIE of 9 cm^{-1} and a KIE of ≈2 for the de- and the reprotonation reactions during the lifetime of the late desensitized, non-conductive P_4^{480} state. The observed KIE of 1 in the time range from 20 ns to 5 ms is incompatible with an early deprotonation of E90. These conclusions are further supported by a pH indicator experiment of the variant E90A and thus, other conclusions that E90 plays a key role in channel opening are ruled out.

Further, the connection between the gating mechanism and the role of water molecules is investigated. The time-resolved step-scan FTIR measurements are complemented by time-resolved electrophysiology measurements and cross-correlation analysis. Ion conductance tallies with vibrational changes of the amide I backbone at 1665(-) and 1648(+) cm^{-1}. Isotope labeled water ($H_2^{18}O$) was used as a solvent to identify these vibrational changes as hydration of transmembrane α-helices. Water

influx proceeds two different steps with time constants of 10 μs and 200 μs. The first step is assigned to pre-gating in ChR2, but only the second leads to ion conductance. A time constant of 10 ms is determined for water efflux, which tallies with channel closure. These correlations hold true for fast (E123T) and slow (D156E) channeling variants of ChR2.
In addition, the overall expansion and compression of transition states in ChR2 are measured by hydrostatic pressure spectroscopy. The pressure dependent photocycle kinetics are recorded at different pressures from 1 to 800 bar and the activation volumes are determined. Early intermediates show decelerated kinetics at higher pressures (positive activation volume), but the later reprotonation of the Schiff base exhibits an accelerated kinetic (negative activation volume). The decay of the conductive P_3^{520} state is also decelerated, which is correlated to water efflux and dehydration of helices. Real volume changes can be calculated from these data, if the extinction coefficient of the intermediate states are known. Influences of the protein environment are explored by experiments of ChR2 solubilized in detergent, reconstituted into lipidic nanodiscs, and unilamellar liposomes.

The gating of ChR2 is initialized by photoisomerization of the retinal chromophore. In the light-adapted ground state it contains a mixture of the 70% all-*trans* retinal and 30% 13-*cis* retinal. The analysis of time-resolved UV/Vis and IR data provides evidence that the 13-*cis* photocycle recovers within 1 ms, which is faster than channel closure and reprotonation of the Schiff base. Thus, the 13-*cis* photocycle is of minor functional relevance in ChR2.
Finally, the link between protonation dynamics and ion gating was investigated by analysis of a non-functional variant: R120H. Although ion conductance is prevented, the photocycle kinetics are very similar to wild-type ChR2. For a detailed analysis pump-probe and QCL spectroscopy are combined in a time-resolved IR data set covering 12 decades from late fs to s. Although an assignment of the arginine band was not feasible, the possible role His-Arg interactions are discussed. Further, I demonstrated that R120 is not part of the proton release complex, which is in contrast to bacteriorhodopsin (bR). In bR, the arginine is part of the proton release complex and has a different orientation, pointing towards the Schiff base, but in ChR2 it is twisted away from the Schiff base and the proton uptake and release kinetics are not effected in R120H.

Although the mechanistic link between proton transfer reaction and channel function remain is not completely identified, we achieved an enormous progress in resolving the molecular details of the photoreaction of ChR2, by applying time-resolved molecular spectroscopy.

Acknowledgement

Although this thesis has been written in English, thanking people in German feels more personally to me.

Zuallererst möchte ich mich bei Prof. Joachim Heberle bedanken, der es mir erst ermöglichte überhaupt diese Dissertation zu beginnen und mir mit Rat und Tat zur Seite stand. Er hat mich gefordert und gefördert, mich kritisiert und gelobt, mit mir gescherzt und ernsthaft diskutiert. Bereits zu Beginn meiner Forschungen durfte ich an internationalen Konferenzen teilzunehmen um meine Ergebnisse zu präsentieren. Ich danke ihm für all dies, da es mich nachhaltig geprägt hat.
Dr. Víctor Lórenz-Fonfría gebührt ein riesiges Dankeschön! Nicht nur für seine Unterstützung bei den Experimenten und bei der Auswertung der Messergebnisse, sondern auch für seine stets freundliche und immer hilfsbereite Art.
Ich danke Bernd Schultz, der nicht nur das QCL spectrometer entwickelt hat, sondern mir auch in allen technischen Fragen beistand und sich ausdauernd um unsere fehleranfälligen Lasersysteme gekümmert hat.
Die aufwendigsten Messungen und Apparaturen nützen nichts ohne eine hervorragende Proteinprobe. Liebe AG Schlesinger, ohne euch würden wir nur Luft und Wasser messen. Vielen Dank für eure Arbeit, insbesondere Dr. Ramona Schlesinger, Dr. Vera Muders, Dr. Nils Krause, Maria Walter, Dorothea Heinrich und Kirsten Hoffmann.

In der Grundlagenforschung arbeitet man nicht alleine, darum danke ich meinen Kollaborationspartnern: Dr. Christian Bamann und Prof. Ernst Bamberg (MPI Frankfurt), Prof. Josef Wachtveitl und Elena Bühl (Universität Frankfurt), Prof. Roland Winter (TU Dortmund) und Prof. Ana-Nicoleta Bondar (FU Berlin). Bei Prof. Ulrike Alexiev möchte ich mich bedanken für die Koordination der Graduiertenschule und für ihre Bereitschaft sich als Zweitgutachterin meiner Dissertation zur Verfügung zu stellen. Außerdem danke ich dem Sonderforschungsbereich 1078 für meine Finanzierung und den universitätsübergreifenden Wissensaustausch zwischen den einzelnen Arbeitsgruppen. Die jährlich stattfinden "Retreats" wurden von Dr. Kerstin Wagner hervorragend organisiert und bei allen Verwaltungsfragen konnte ich mich immer an Silvia Luther wenden.

Ich bedanke mich außerdem bei all meinen Kollegen. Die Atmosphäre in unserer Arbeitsgruppe ist hervorragend und der Zusammenhalt einfach wunderbar. Hervorheben möchte ich Dr. Silke Kerruth und Emanuel Pfitzner, die sich nicht nur mit mir das Büro geteilt haben, sondern auch meine engen Freunde geworden sind. Was mich zu den lieben Menschen außerhalb der Universität bringt.

Meine besten Freunde Xenia Knigge, Jens Möckel, Christopher Mielack und Marc Hofmann haben mich immer dann aufgebaut, wenn es mal nicht so gut lief und sich mit mir gefreut, wenn ich Erfolg hatte. Vielen lieben Dank!

Das wichtigste kommt zum Schluss. Meinen Großeltern, Irene und Georg Sych sowie Erika und Bernhard Resler möchte ich für ihre Unterstützung danken. Meinen Eltern, Petra und Jörg Resler, meinem Bruder Arno Resler und meinem Lebensgefährten Florian Kössl gebührt ein besonderer Dank. Eure Unterstützung und Liebe sind grenzenlos.

Bibliography

[1] V. Schuenemann. “Biophysik - Eine Einführung”. In: *Springer Verlag* (2005).

[2] E. Gouaux and R. Mackinnon. “Principles of selective ion transport in channels and pumps”. In: *Science* 310.5753 (2005), pp. 1461–5.

[3] B. Corry and S. H. Chung. “Mechanisms of valence selectivity in biological ion channels”. In: *Cell Mol Life Sci* 63.3 (2006), pp. 301–15.

[4] V. A. Lórenz-Fonfría and J. Heberle. “Channelrhodopsin unchained: structure and mechanism of a light-gated cation channel”. In: *Biochim Biophys Acta* 1837.5 (2014), pp. 626–42.

[5] V. A. Lórenz-Fonfría, T. Resler, et al. “Transient protonation changes in channel- rhodopsin-2 and their relevance to channel gating”. In: *Proc Natl Acad Sci U S A* 110.14 (2013), E1273–81.

[6] C. Bamann, T. Kirsch, et al. “Spectral characteristics of the photocycle of channelrhodopsin-2 and its implication for channel function”. In: *J Mol Biol* 375.3 (2008), pp. 686–94.

[7] E. Ritter, K. Stehfest, et al. “Monitoring light-induced structural changes of channelrhodopsin-2 by UV-visible and Fourier transform infrared spectroscopy”. In: *J Biol Chem* 283.50 (2008), pp. 35033–41.

[8] G. Nagel, D. Ollig, et al. “Channelrhodopsin-1: a light-gated proton channel in green algae”. In: *Science* 296.5577 (2002), pp. 2395–8.

[9] P. Hegemann. “Algal sensory photoreceptors”. In: *Annu Rev Plant Biol* 59 (2008), pp. 167–89.

[10] L. A. Gunaydin, O. Yizhar, et al. “Ultrafast optogenetic control”. In: *Nat Neurosci* 13.3 (2010), pp. 387–92.

[11] P. Hegemann and G. Nagel. “From channelrhodopsins to optogenetics”. In: *EMBO Mol Med* 5.2 (2013), pp. 173–6.

[12] M. M. Doroudchi, K. P. Greenberg, et al. “Virally delivered channelrhodopsin-2 safely and effectively restores visual function in multiple mouse models of blindness”. In: *Mol Ther* 19.7 (2011), pp. 1220–9.

[13] L. Fenno, O. Yizhar, and K. Deisseroth. “The Development and Application of Optogenetics”. In: *Annual Review of Neuroscience, Vol 34* 34 (2011), pp. 389–412.

[14] K. Deisseroth. “Optogenetics”. In: *Nat Methods* 8.1 (2011), pp. 26–9.

[15] F. Zhang, J. Vierock, et al. “The microbial opsin family of optogenetic tools”. In: *Cell* 147.7 (2011), pp. 1446–57.

[16] X. Han. “In vivo application of optogenetics for neural circuit analysis”. In: *ACS Chem Neurosci* 3.8 (2012), pp. 577–84.

[17] A. Kalmbach, T. Hedrick, and J. Waters. “Selective optogenetic stimulation of cholinergic axons in neocortex”. In: *J Neurophysiol* 107.7 (2012), pp. 2008–19.

[18] X. Liu, S. Ramirez, et al. “Optogenetic stimulation of a hippocampal engram activates fear memory recall”. In: *Nature* 484.7394 (2012), pp. 381–5.

[19] M. Prigge, F. Schneider, et al. “Color-tuned channelrhodopsins for multiwavelength optogenetics”. In: *J Biol Chem* 287.38 (2012), pp. 31804–12.

[20] K. Berglund, E. Birkner, et al. “Light-emitting channelrhodopsins for combined optogenetic and chemical-genetic control of neurons”. In: *PLoS One* 8.3 (2013), e59759.

[21] J. C. Williams, J. Xu, et al. “Computational optogenetics: empirically-derived voltage- and light-sensitive channelrhodopsin-2 model”. In: *PLoS Comput Biol* 9.9 (2013), e1003220.

[22] N. AzimiHashemi, K. Erbguth, et al. “Synthetic retinal analogues modify the spectral and kinetic characteristics of microbial rhodopsin optogenetic tools”. In: *Nature Communications* 5 (2014).

[23] A. Dawydow, R. Gueta, et al. “Channelrhodopsin-2-XXL, a powerful optogenetic tool for low-light applications”. In: *Proc Natl Acad Sci U S A* 111.38 (2014), pp. 13972–7.

[24] H. E. Kato, M. Kamiya, et al. “Atomistic design of microbial opsin-based blue-shifted optogenetics tools”. In: *Nature Communications* 6 (2015), p. 7177.

[25] A. Berndt, S. Y. Lee, et al. “Structural foundations of optogenetics: Determinants of channelrhodopsin ion selectivity”. In: *Proc Natl Acad Sci U S A* 113.4 (2016), pp. 822–9.

[26] V. A. Lórenz-Fonfría and J. Heberle. “Proton transfer and protein conformation dynamics in photosensitive proteins by time-resolved step-scan Fourier-transform infrared spectroscopy”. In: *J Vis Exp* 88 (2014), e51622.

[27] C. Del Val, J. Royuela-Flor, et al. “Channelrhodopsins: a bioinformatics perspective”. In: *Biochim Biophys Acta* 1837.5 (2014), pp. 643–55.

[28] J. Heberle, J. Fitter, et al. “Bacteriorhodopsin: the functional details of a molecular machine are being resolved”. In: *Biophys Chem* 85.2-3 (2000), pp. 229–48.

[29] K. Feldbauer, D. Zimmermann, et al. “Channelrhodopsin-2 is a leaky proton pump”. In: *Proc Natl Acad Sci U S A* 106.30 (2009), pp. 12317–22.

[30] M. Nack, I. Radu, et al. “Kinetics of proton release and uptake by channelrhodopsin-2”. In: *FEBS Lett* 586.9 (2012), pp. 1344–8.

[31] H. E. Kato, F. Zhang, et al. “Crystal structure of the channelrhodopsin light-gated cation channel”. In: *Nature* 482.7385 (2012), pp. 369–74.

[32] M. K. Neumann-Verhoefen, K. Neumann, et al. “Ultrafast infrared spectroscopy on channelrhodopsin-2 reveals efficient energy transfer from the retinal chromophore to the protein”. In: *J Am Chem Soc* 135.18 (2013), pp. 6968–76.

[33] S. Ito, H. E. Kato, et al. “Water-containing hydrogen-bonding network in the active center of channelrhodopsin”. In: *J Am Chem Soc* 136.9 (2014), pp. 3475–82.

[34] T. Resler, B. J. Schultz, et al. “Kinetic and Vibrational Isotope Effects of Proton Transfer Reactions in Channelrhodopsin-2”. In: *Biophys J* 109.2 (2015), pp. 287–97.

[35] J. Kuhne, K. Eisenhauer, et al. “Early formation of the ion-conducting pore in channelrhodopsin-2”. In: *Angew Chem Int Ed Engl* 54.16 (2014), pp. 4953–7.

[36] R. P. Bell. “Recent advances in study of kinetic hydrogen isotope-effects”. In: *Chem Soc Rev* 3.4 (1974), pp. 513–544.

[37] P. K. Glasoe and F. A. Long. “Use of glass electrodes to measure acidities in deuterium oxide”. In: *Journal of Physical Chemistry* 64.1 (1960), pp. 188–190.

[38] L. I. Krishtalik. “The mechanism of the proton transfer: an outline”. In: *Biochim Biophys Acta* 1458.1 (2000), pp. 6–27.

[39] J. Heberle and N. A. Dencher. “Proton transfer in the light-harvesting protein bacteriorhodopsin: an investigation with optical pH-indicators”. In: *proton transfer in hydrogen-bonded systems*. Ed. by T. Bountis. New York: Plenum Press, 1992, pp. 187–197.

[40] J. Le Coutre and K. Gerwert. “Kinetic isotope effects reveal an ice-like and a liquid-phase-type intramolecular proton transfer in bacteriorhodopsin”. In: *FEBS Lett* 398.2-3 (1996), pp. 333–6.

[41] D. L. Jenson, A. Evans, and B. A. Barry. “Proton-coupled electron transfer and tyrosine D of photosystem II”. In: *J Phys Chem B* 111.43 (2007), pp. 12599–604.

[42] A. Klauss, M. Haumann, and H. Dau. “Alternating electron and proton transfer steps in photosynthetic water oxidation”. In: *Proc Natl Acad Sci U S A* 109.40 (2012), pp. 16035–40.

[43] A. L. Johansson, S. Chakrabarty, et al. “Proton-transport mechanisms in cytochrome c oxidase revealed by studies of kinetic isotope effects”. In: *Biochim Biophys Acta* 1807.9 (2011), pp. 1083–94.

[44] V. A. Lórenz-Fonfría and H. Kandori. “Bayesian maximum entropy (two-dimensional) lifetime distribution reconstruction from time-resolved spectroscopic data”. In: *Appl Spectrosc* 61.4 (2007), pp. 428–43.

[45] K. Eisenhauer, J. Kuhne, et al. “In channelrhodopsin-2 Glu-90 is crucial for ion selectivity and is deprotonated during the photocycle”. In: *J Biol Chem* 287.9 (2012), pp. 6904–11.

[46] M. Nack, I. Radu, et al. “The retinal structure of channelrhodopsin-2 assessed by resonance Raman spectroscopy”. In: *FEBS Lett* 583.22 (2009), pp. 3676–80.

[47] V. Muders, S. Kerruth, et al. “Resonance Raman and FTIR spectroscopic characterization of the closed and open states of channelrhodopsin-1”. In: *FEBS Lett* 588.14 (2014), pp. 2301–6.

[48] P. Hegemann, S. Ehlenbeck, and D. Gradmann. “Multiple photocycles of channelrhodopsin”. In: *Biophys J* 89.6 (2005), pp. 3911–8.

[49] K. Nikolic, N. Grossman, et al. “Photocycles of channelrhodopsin-2”. In: *Photochem Photobiol* 85.1 (2009), pp. 400–11.

[50] F. Schneider, D. Gradmann, and P. Hegemann. “Ion selectivity and competition in channelrhodopsins”. In: *Biophys J* 105.1 (2013), pp. 91–100.

[51] E. Ritter, P. Piwowarski, et al. “Light-dark adaptation of channelrhodopsin C128T mutant”. In: *J Biol Chem* 288.15 (2013), pp. 10451–8.

[52] V. A. Lórenz-Fonfría, B. J. Schultz, et al. “Pre-gating conformational changes in the ChETA variant of channelrhodopsin-2 monitored by nanosecond IR spectroscopy”. In: *J Am Chem Soc* 137.5 (2015), pp. 1850–61.

[53] M. Müller, C. Bamann, et al. “Projection structure of channelrhodopsin-2 at 6 Å resolution by electron crystallography”. In: *J Mol Biol* 414.1 (2011), pp. 86–95.

[54] F. Garczarek, L. S. Brown, et al. “Proton binding within a membrane protein by a protonated water cluster”. In: *Proc Natl Acad Sci U S A* 102.10 (2005), pp. 3633–8.

[55] A. P. Plazzo, N. De Franceschi, et al. “Bioinformatic and mutational analysis of channelrhodopsin-2 protein cation-conducting pathway”. In: *J Biol Chem* 287.7 (2012), pp. 4818–25.

[56] N. Krause, C. Engelhard, et al. “Structural differences between the closed and open states of channelrhodopsin-2 as observed by EPR spectroscopy”. In: *FEBS Lett* 587.20 (2013), pp. 3309–13.

[57] J. Wietek, J. S. Wiegert, et al. “Conversion of channelrhodopsin into a light-gated chloride channel”. In: *Science* 344.6182 (2014), pp. 409–12.

[58] V. A. Lórenz-Fonfría, C. Bamann, et al. “Temporal evolution of helix hydration in a light-gated ion channel correlates with ion conductance”. In: *Proc Natl Acad Sci U S A* 112.43 (2015), E5796–804.

[59] F. Scholz, E. Bamberg, et al. “Tuning the primary reaction of channelrhodopsin-2 by imidazole, pH, and site-specific mutations”. In: *Biophys J* 102.11 (2012), pp. 2649–57.

[60] O. A. Sineshchekov, E. G. Govorunova, et al. “Intramolecular proton transfer in channelrhodopsins”. In: *Biophys J* 104.4 (2013), pp. 807–17.

[61] V. A. Lórenz-Fonfría, V. Muders, et al. “Changes in the hydrogen-bonding strength of internal water molecules and cysteine residues in the conductive state of channelrhodopsin-1”. In: *J Chem Phys* 141.22 (2014), p. 22D507.

[62] T. Sattig, C. Rickert, et al. “Light-induced movement of the transmembrane helix B in channelrhodopsin-2”. In: *Angew Chem Int Ed Engl* 52.37 (2013), pp. 9705–8.

[63] H. Mohrmann, I. Kube, et al. “Transient Conformational Changes of Sensory Rhodopsin II Investigated by Vibrational Stark Effect Probes”. In: *J Phys Chem B* 120.19 (2016), pp. 4383–7.

[64] M. Reppert and A. Tokmakoff. “Computational Amide I 2D IR Spectroscopy as a Probe of Protein Structure and Dynamics”. In: *Annu Rev Phys Chem* 67 (2016), pp. 359–86.

[65] J. Marque and L. Eisenstein. “Pressure Effects on the Photocycle of Purple Membrane”. In: *Biochemistry* 23.23 (1984), pp. 5556–5563.

[66] M. Gross and R. Jaenicke. “Proteins under pressure. The influence of high hydrostatic pressure on structure, function and assembly of proteins and protein complexes”. In: *Eur J Biochem* 221.2 (1994), pp. 617–30.

[67] S. E. Braslavsky and G. E. Heibel. “Time-Resolved Photothermal and Photoacoustic Methods Applied to Photoinduced Processes in Solution”. In: *Chemical Reviews* 92.6 (1992), pp. 1381–1410.

[68] P. J. Schulenberg, M. Rohr, et al. “Photoinduced Volume Changes Associated with the Early Transformations of Bacteriorhodopsin - a Laser-Induced Optoacoustic Spectroscopy Study”. In: *Biophys J* 66.3 (1994), pp. 838–843.

[69] W. B. Jackson, N. M. Amer, et al. “Photothermal Deflection Spectroscopy and Detection”. In: *Applied Optics* 20.8 (1981), pp. 1333–1344.

[70] P. J. Schulenberg, W. Gartner, and S. E. Braslavsky. “Time-Resolved Volume Changes during the Bacteriorhodopsin Photocycle - a Photothermal Beam Deflection Study”. In: *Journal of Physical Chemistry* 99.23 (1995), pp. 9617–9624.

[71] V. V. Mozhaev, K. Heremans, et al. “High pressure effects on protein structure and function”. In: *Proteins* 24.1 (1996), pp. 81–91.

[72] G. Varo and J. K. Lanyi. “Effects of Hydrostatic-Pressure on the Kinetics Reveal a Volume Increase during the Bacteriorhodopsin Photocycle”. In: *Biochemistry* 34.38 (1995), pp. 12161–12169.

[73] B. U. Klink, R. Winter, et al. “Pressure dependence of the photocycle kinetics of bacteriorhodopsin”. In: *Biophys J* 83.6 (2002), pp. 3490–8.

[74] W. Parson. “Modern Optical Spectroscopy”. In: *Springer* (2009).

[75] R. W. Hendler and R. I. Shrager. “Deconvolutions based on singular value decomposition and the pseudoinverse: a guide for beginners”. In: *J Biochem Biophys Methods* 28.1 (1994), pp. 1–33.

[76] J. Woenckhaus, R. Kohling, et al. “High pressure-jump apparatus for kinetic studies of protein folding reactions using the small-angle synchrotron x-ray scattering technique”. In: *Review of Scientific Instruments* 71.10 (2000), pp. 3895–3899.

[77] T. K. Ritchie, Y. V. Grinkova, et al. “Reconstitution of Membrane Proteins in Phospholipid Bilayer Nanodiscs”. In: *Methods in Enzymology; Liposomes, Pt F* 464 (2009), pp. 211–231.

[78] P. R. Griffith and J. A. Haseth. “Fourier Transform Infrared Spectrometry”. In: *WILEY* (2007).

[79] G. C. Ellis-Davies. “Caged compounds: photorelease technology for control of cellular chemistry and physiology”. In: *Nat Methods* 4.8 (2007), pp. 619–28.

[80] W. Herres and J. Gronholz. “Understanding FT-IR Data Processing”. In: *Series* (2009).

[81] D. Baurecht. “Fourier-Transform-Infrared- (FTIR)-Spektroskopie”. In: *Institut für Biophysikalische Chemie Universität Wien* (2008).

[82] A. Pfeifer. “Infrarotspektroskopische Aufklärung lichtinduzierter Strukturänderungen im Blaulichtsensor Phototropin”. In: *Dissertation Universität Bielefeld* (2009).

[83] A. Barth and C. Zscherp. “What vibrations tell us about proteins”. In: *Quarterly Reviews of Biophysics* 35.4 (2002), pp. 369–430.

[84] B. Aton, A. G. Doukas, et al. “Resonance Raman studies of the purple membrane”. In: *Biochemistry* 16.13 (1977), pp. 2995–9.

[85] K. Stehfest, E. Ritter, et al. “The branched photocycle of the slow-cycling channelrhodopsin-2 mutant C128T”. In: *J Mol Biol* 398.5 (2010), pp. 690–702.

[86] A. K. Dioumaev and M. S. Braiman. “Two bathointermediates of the bacteriorhodopsin photocycle, distinguished by nanosecond time-resolved FTIR spectroscopy at room temperature”. In: *Journal of Physical Chemistry B* 101.9 (1997), pp. 1655–1662.

[87] C. Hackmann, J. Guijarro, et al. “Static and time-resolved step-scan Fourier transform infrared investigations of the photoreaction of halorhodopsin from Natronobacterium pharaonis: Consequences for models of the anion translocation mechanism”. In: *Biophys J* 81.1 (2001), pp. 394–406.

[88] M. Hein, A. A. Wegener, et al. “Time-resolved FTIR studies of sensory rhodopsin II (NpSRII) from Natronobacterium pharaonis: Implications for proton transport and receptor activation”. In: *Biophys J* 84.2 (2003), pp. 1208–1217.

[89] C. Zscherp, R. Schlesinger, et al. “In situ determination of transient pKa changes of internal amino acids of bacteriorhodopsin by using time-resolved attenuated total reflection Fourier-transform infrared spectroscopy”. In: *Proc Natl Acad Sci U S A* 96.10 (1999), pp. 5498–503.

[90] B. Nie, J. Stutzman, and A. Xie. “A vibrational spectral maker for probing the hydrogen-bonding status of protonated Asp and Glu residues”. In: *Biophys J* 88.4 (2005), pp. 2833–47.

[91] K. Takei, R. Takahashi, and T. Noguchi. “Correlation between the hydrogen-bond structures and the C=O stretching frequencies of carboxylic acids as studied by density functional theory calculations: theoretical basis for interpretation of infrared bands of carboxylic groups in proteins”. In: *J Phys Chem B* 112.21 (2008), pp. 6725–31.

[92] C. Bamann, R. Gueta, et al. “Structural guidance of the photocycle of channelrhodopsin-2 by an interhelical hydrogen bond”. In: *Biochemistry* 49.2 (2010), pp. 267–78.

[93] J. Sasaki, L. S. Brown, et al. “Conversion of bacteriorhodopsin into a chloride ion pump”. In: *Science* 269.5220 (1995), pp. 73–5.

[94] L. S. Brown, R. Needleman, and J. K. Lanyi. “Origins of deuterium kinetic isotope effects on the proton transfers of the bacteriorhodopsin photocycle”. In: *Biochemistry* 39.5 (2000), pp. 938–45.

[95] R. Korenstein, W. V. Sherman, and S. R. Caplan. “Kinetic isotope effects in the photochemical cycle of bacteriorhodopsin”. In: *Biophys Struct Mech* 2.3 (1976), pp. 267–76.

[96] Y. Cao, L. S. Brown, et al. “Relationship of proton release at the extracellular surface to deprotonation of the schiff base in the bacteriorhodopsin photocycle”. In: *Biophys J* 68.4 (1995), pp. 1518–30.

[97] S. Y. Liu. “Light-induced currents from oriented purple membrane: I. Correlation of the microsecond component (B2) with the L-M photocycle transition”. In: *Biophys J* 57.5 (1990), pp. 943–50.

[98] I. Radu, M. Schleeger, et al. “Time-resolved methods in biophysics. 10. Time-resolved FT-IR difference spectroscopy and the application to membrane proteins”. In: *Photochem Photobiol Sci* 8.11 (2009), pp. 1517–28.

[99] A. Maeda, J. Sasaki, et al. “Structures of aspartic acid-96 in the L and N intermediates of bacteriorhodopsin: analysis by Fourier transform infrared spectroscopy”. In: *Biochemistry* 31.19 (1992), pp. 4684–90.

[100] I. Radu, C. Bamann, et al. “Conformational changes of channelrhodopsin-2”. In: *J Am Chem Soc* 131.21 (2009), pp. 7313–9.

[101] M. Nack, I. Radu, et al. “The DC gate in channelrhodopsin-2: crucial hydrogen bonding interaction between C128 and D156”. In: *Photochem Photobiol Sci* 9.2 (2010), pp. 194–8.

[102] K. Ruffert, B. Himmel, et al. “Glutamate residue 90 in the predicted transmembrane domain 2 is crucial for cation flux through channelrhodopsin 2”. In: *Biochem Biophys Res Commun* 410.4 (2011), pp. 737–43.

[103] D. Y. Vorobyev, C. H. Kuo, et al. “Water-Induced Relaxation of a Degenerate Vibration of Guanidium Using 2D IR Echo Spectroscopy”. In: *Journal of Physical Chemistry B* 114.8 (2010), pp. 2944–2953.

[104] M. S. Braiman, D. M. Briercheck, and K. M. Kriger. “Modeling vibrational spectra of amino acid side chains in proteins: Effects of protonation state, counterion, and solvent on arginine C-N stretch frequencies”. In: *Journal of Physical Chemistry B* 103.22 (1999), pp. 4744–4750.

[105] C. Miller. “ClC chloride channels viewed through a transporter lens”. In: *Nature* 440.7083 (2006), pp. 484–9.

[106] J. Borch and T. Hamann. “The nanodisc: a novel tool for membrane protein studies”. In: *Biol Chem* 390.8 (2009), pp. 805–14.

[107] H. C. Watanabe, K. Welke, et al. “Structural model of channelrhodopsin”. In: *J Biol Chem* 287.10 (2012), pp. 7456–66.

[108] J. Heberle, D. Oesterhelt, and N. A. Dencher. “Decoupling of photo- and proton cycle in the Asp85–>Glu mutant of bacteriorhodopsin”. In: *EMBO J* 12.10 (1993), pp. 3721–7.

[109] G. Iliadis, G. Zundel, and B. Brzezinski. “Aspartic proteinases–Fourier transform IR studies of the aspartic carboxylic groups in the active site of pepsin”. In: *FEBS Lett* 352.3 (1994), pp. 315–7.

[110] A. Peralavarez-Marin, M. Marquez, et al. “Thr-90 plays a vital role in the structure and function of bacteriorhodopsin”. In: *Journal of Biological Chemistry* 279.16 (2004), pp. 16403–16409.

[111] M. K. Verhoefen, C. Bamann, et al. “The photocycle of channelrhodopsin-2: ultrafast reaction dynamics and subsequent reaction steps”. In: *Chemphyschem* 11.14 (2010), pp. 3113–22.

[112] R. Vogel, M. Mahalingam, et al. “Functional role of the "ionic lock"–an interhelical hydrogen-bond network in family A heptahelical receptors”. In: *J Mol Biol* 380.4 (2008), pp. 648–55.

[113] Y. Sugiyama, H. Wang, et al. “Photocurrent attenuation by a single polar-to-nonpolar point mutation of channelrhodopsin-2”. In: *Photochem Photobiol Sci* 8.3 (2009), pp. 328–36.

[114] O. P. Ernst, P. A. Sánchez Murcia, et al. “Photoactivation of channelrhodopsin”. In: *J Biol Chem* 283.3 (2008), pp. 1637–43.

[115] S. Száraz, D. Oesterhelt, and P. Ormos. “pH-induced structural changes in bacteriorhodopsin studied by Fourier transform infrared spectroscopy”. In: *Biophys J* 67.4 (1994), pp. 1706–12.

[116] A. K. Dioumaev. “Infrared methods for monitoring the protonation state of carboxylic amino acids in the photocycle of bacteriorhodopsin”. In: *Biochemistry (Mosc)* 66.11 (2001), pp. 1269–76.

[117] K. Welke, H. C. Watanabe, et al. “QM/MM simulations of vibrational spectra of bacteriorhodopsin and channelrhodopsin-2”. In: *Phys Chem Chem Phys* 15.18 (2013), pp. 6651–9.

[118] S. Scheiner. “Calculation of isotope effects from first principles”. In: *Biochim Biophys Acta* 1458.1 (2000), pp. 28–42.

[119] G. H. Bare, J. O. Alben, and P. A. Bromberg. “Sulfhydryl groups in hemoglobin. A new molecular probe at the alpha1 beta 1 interface studied by Fourier transform infrared spectroscopy”. In: *Biochemistry* 14.8 (1975), pp. 1578–83.

[120] T. Noguchi, Y. Fukami, et al. “Fourier transform infrared study on the primary donor P798 of Heliobacterium modesticaldum: cysteine S-H coupled to P798 and molecular interactions of carbonyl groups”. In: *Biochemistry* 36.40 (1997), pp. 12329–36.

[121] A. Inaguma, H. Tsukamoto, et al. “Chimeras of channelrhodopsin-1 and -2 from chlamydomonas reinhardtii exhibit distinctive light-induced structural changes from channelrhodopsin-2”. In: *J Biol Chem* 290.18 (2015), pp. 11623–34.

[122] H. C. Watanabe, K. Welke, et al. “Towards an understanding of channelrhodopsin function: simulations lead to novel insights of the channel mechanism”. In: *J Mol Biol* 425.10 (2013), pp. 1795–814.

[123] H. Li, A. D. Robertson, and J. H. Jensen. “Very fast empirical prediction and rationalization of protein pK(a) values”. In: *Proteins-Structure Function and Bioinformatics* 61.4 (2005), pp. 704–721.

[124] C. R. Søndergaard, M. H. M. Olsson, et al. “Improved Treatment of Ligands and Coupling Effects in Empirical Calculation and Rationalization of pK(a) Values”. In: *Journal of Chemical Theory and Computation* 7.7 (2011), pp. 2284–2295.

[125] J. Vondrasek, P. E. Mason, et al. “The Molecular Origin of Like-Charge Arginine-Arginine Pairing in Water”. In: *Journal of Physical Chemistry B* 113.27 (2009), pp. 9041–9045.

[126] J. Heyda, R. Vacha, et al. “Ions at aqueous interfaces: From water surface to hydrated proteins”. In: *Abstracts of Papers of the American Chemical Society* 237 (2009).

[127] J. Heyda, P. E. Mason, and P. Jungwirth. “Attractive interactions between side chains of histidine-histidine and histidine-arginine-based cationic dipeptides in water”. In: *J Phys Chem B* 114.26 (2010), pp. 8744–9.

[128] D. Gradmann, A. Berndt, et al. “Rectification of the channelrhodopsin early conductance”. In: *Biophys J* 101.5 (2011), pp. 1057–68.

[129] G. Nagel, M. Brauner, et al. “Light activation of channelrhodopsin-2 in excitable cells of Caenorhabditis elegans triggers rapid behavioral responses”. In: *Curr Biol* 15.24 (2005), pp. 2279–84.

[130] S. A. Pless, A. P. Niciforovic, et al. “A novel mechanism for fine-tuning open-state stability in a voltage-gated potassium channel”. In: *Nature Communications* 4 (2013), p. 1784.

[131] Y. Xiao, M. S. Hutson, et al. “Role of arginine-82 in fast proton release during the bacteriorhodopsin photocycle: a time-resolved FT-IR study of purple membranes containing 15N-labeled arginine”. In: *Biochemistry* 43.40 (2004), pp. 12809–18.

[132] M. S. Hutson, U. Alexiev, et al. “Evidence for a perturbation of arginine-82 in the bacteriorhodopsin photocycle from time-resolved infrared spectra”. In: *Biochemistry* 39.43 (2000), pp. 13189–13200.

[133] R. Rammelsberg, G. Huhn, et al. “Bacteriorhodopsin’s intramolecular proton-release pathway consists of a hydrogen-bonded network”. In: *Biochemistry* 37.14 (1998), pp. 5001–5009.

[134] C. Scharnagl and S. F. Fischer. “Conformational flexibility of arginine-82 as source for the heterogeneous and pH-dependent kinetics of the primary proton transfer step in the bacteriorhodopsin photocycle: An electrostatic model”. In: *Chemical Physics* 212.1 (1996), pp. 231–246.

[135] O. Beckstein, P. C. Biggin, et al. “Ion channel gating: insights via molecular simulations”. In: *FEBS Lett* 555.1 (2003), pp. 85–90.

[136] M. O. Jensen, V. Jogini, et al. “Mechanism of voltage gating in potassium channels”. In: *Science* 336.6078 (2012), pp. 229–33.

[137] Q. Cheng, M. Du, et al. “Evolution of glutamate interactions during binding to a glutamate receptor”. In: *Nat Chem Biol* 1.6 (2005), pp. 329–32.

[138] J. Zimmerberg, F. Bezanilla, and V. A. Parsegian. “Solute inaccessible aqueous volume changes during opening of the potassium channel of the squid giant axon”. In: *Biophys J* 57.5 (1990), pp. 1049–64.

[139] H. Kamikubo and M. Kataoka. “Can the low-resolution structures of photointermediates of bacteriorhodopsin explain their crystal structures?” In: *Biophys J* 88.3 (2005), pp. 1925–31.

[140] L. Eisenstein. “Effect of Viscosity on the Photocycle of Bacteriorhodopsin”. In: *Methods in Enzymology* 88 (1982), pp. 297–305.

[141] M. Tsuda and T. G. Ebrey. “Effect of high pressure on the absorption spectrum and isomeric composition of bacteriorhodopsin”. In: *Biophys J* 30.1 (1980), pp. 149–57.

[142] I. Kovacs, G. U. Nienhaus, et al. “Pressure Effects on the Dark-Adaptation of Bacteriorhodopsin”. In: *Biophys J* 64.4 (1993), pp. 1187–1193.

List of Figures

List of Tables

Selbstständigkeitserklärung

Hiermit bestätige ich, dass die vorliegende Doktorarbeit allein von mir und nur mit Hilfe der angegebenen Hilfsmittel angefertigt wurde. Und ich bestätige hiermit, dass diese Arbeit nicht schon einmal in einem früheren Promotionsverfahren angenommen oder als ungenügend beurteilt wurde.

Berlin, Dezember 21, 2016

Tom Resler